FABRICATION AND CHARACTERIZATION OF QUANTUM DOT SENSITIZED SOLAR CELLS WITH METHYLCELLULOSE–POLYSULPHIDE GEL POLYMER ELECTROLYTE

MUHAMMAD AMMAR BIN MINGSUKANG

FACULTY OF SCIENCE
UNIVERSITY OF MALAYA
KUALA LUMPUR

2019

FABRICATION AND CHARACTERIZATION OF QUANTUM DOT SENSITIZED SOLAR CELLS WITH METHYLCELLULOSE–POLYSULPHIDE GEL POLYMER ELECTROLYTE

MUHAMMAD AMMAR BIN MINGSUKANG

THESIS SUBMITTED IN FULFILMENT OF THE REQUIREMENTS FOR THE DEGREE OF DOCTOR OF PHILOSOPHY

DEPARTMENT OF PHYSICS
FACULTY OF SCIENCE
UNIVERSITY OF MALAYA
KUALA LUMPUR

2019

UNIVERSITY OF MALAYA
ORIGINAL LITERARY WORK DECLARATION

Name of Candidate: **MUHAMMAD AMMAR BIN MINGSUKANG**

Matric No: **SHC160067**

Name of Degree: **DOCTOR OF PHILOSOPHY**

Title of Thesis:

FABRICATION AND CHARACTERIZATION OF QUANTUM DOT SENSITIZED SOLAR CELLS WITH METHYLCELLULOSE–POLYSULPHIDE GEL POLYMER ELECTROLYTE

Field of Study: **EXPERIMENTAL PHYSICS**

I do solemnly and sincerely declare that:

(1) I am the sole author/writer of this Work;
(2) This Work is original;
(3) Any use of any work in which copyright exists was done by way of fair dealing and for permitted purposes and any excerpt or extract from, or reference to or reproduction of any copyright work has been disclosed expressly and sufficiently and the title of the Work and its authorship have been acknowledged in this Work;
(4) I do not have any actual knowledge nor do I ought reasonably to know that the making of this work constitutes an infringement of any copyright work;
(5) I hereby assign all and every rights in the copyright to this Work to the University of Malaya ("UM"), who henceforth shall be owner of the copyright in this Work and that any reproduction or use in any form or by any means whatsoever is prohibited without the written consent of UM having been first had and obtained;
(6) I am fully aware that if in the course of making this Work I have infringed any copyright whether intentionally or otherwise, I may be subject to legal action or any other action as may be determined by UM.

Candidate's Signature Date:

Subscribed and solemnly declared before,

Witness's Signature Date:

Name:

Designation:

FABRICATION AND CHARACTERIZATION OF QUANTUM DOT SENSITIZED SOLAR CELLS WITH METHYLCELLULOSE–POLYSULPHIDE GEL POLYMER ELECTROLYTE

ABSTRACT

Polysulphide liquid electrolyte (PLE) is used as a medium to transport charge from counter electrode (CE) to the photoanode in a quantum dot sensitized solar cell (QDSSC). In this work, novel polysulphide gel polymer electrolyte (PGPE) has been used to replace PLE in order to overcome the problems that result from the use of liquid electrolytes. Methylcellulose (MC) has been chosen as the host polymer since it is biocompatible, cheap, and easily dissolves in water. MC–PGPE with composition of 3.54 *wt.%* MC, 88.46 *wt.%* distilled water, 7.78 *wt.%* Na_2S and 0.22 *wt.%* S shows the highest room temperature (RT) ionic conductivity of (0.191 ± 0.001) S cm^{-1} and lowest activation energy of (55.25 ± 1.15) meV. CdS quantum dot (QD) has been used as sensitizer and is deposited on TiO_2 semiconducting film using successive ionic layer absorption and reaction (SILAR) method. The [FTO / TiO_2 blocking layer / TiO_2 mesoporous layer / CdS] assembly is called the photoanode. QDSSC fabricated with the optimized MC–PGPE, optimized photoanode with 5 SILAR cycles for CdS deposition and platinum (Pt) CE i.e. [FTO / TiO_2 / CdS(5) / electrolyte / Pt(CE) / FTO] QDSSC assembly shows the best performance with power conversion efficiency (*PCE*) of (0.77 ± 0.01)%, short circuit current density (J_{sc}) of (4.54 ± 0.10) mA cm^{-2}, open circuit voltage (V_{oc}) of (0.51 ± 0.01) V and fill factor (*FF*) of (0.34 ± 0.03). The QDSSC photoanode is then deposited with ZnS and SiO_2 passivation layers and to form the QDSSC with configuration: [FTO / TiO_2 / CdS(5) / ZnS / SiO_2 / electrolyte / Pt(CE) / FTO]. A *PCE* of (1.34 ± 0.13)%, J_{sc} of (7.09 ± 0.27) mA cm^{-2}, V_{oc} of (0.56 ± 0.04) V and *FF* of (0.34 ± 0.01) have been obtained. Finally, the work investigates the better material for use as CE. Two materials other than Pt have been used as CE i.e. gold (Au) and lead sulphide (PbS). QDSSC fabricated with PbS CE [FTO / TiO_2 / CdS(5) / ZnS / SiO_2 / electrolyte / PbS(CE) /FTO] shows the best performance with *PCE* of (2.83 ± 0.07)%, J_{sc} of (9.54 ± 0.16) mA cm^{-2}, V_{oc} of (0.60 ± 0.02) V and *FF* of (0.49 ± 0.03).

Keywords: Polysulphide gel polymer electrolyte, methylcellulose, quantum dot sensitized solar cells

FABRIKASI DAN PENCIRIAN SEL SURIA DIPEKAKAN TITIK KUANTUM MENGUNAKAN METILSELULOSA–POLISULFIDA ELEKTROLIT POLIMER GEL

ABSTRAK

Elektrolit cecair polisulfida (ECP) di gunakan sebagai medium untuk pengangkutan cas dari katod (K) ke anod di dalam sel suria dipekakan titik kuantum (SSDTK). Dalam kerja ini, polisulfida elektrolit polimer gel (PEPG) telah digunakan untuk menggantikan ECP untuk mengatasi masalah yang timbul akibat penggunaan elektrolit cecair. Metilselulosa (MS) telah dipilih sebagai polimer perumah kerana ia biokompatibel, murah, dan mudah larut dalam air. MS–PEPG dengan komposisi 3.54 *wt.%* MS, 88.46 *wt.%* air suling, 7.78 *wt.%* Na_2S dan 0.22 *wt.%* S menunjukkan kekonduksian ionik suhu bilik (SB) tertinggi pada (0.191 ± 0.001) S cm^{-1} dengan tenaga pengaktifan terendah sebanyak (55.25 ± 1.15) meV. Titik kuantum (TK) CdS telah digunakan sebagai pemeka dan dimendapkan pada filem TiO_2 (anod) menggunakan kaedah penyerapan dan tindak balas lapisan ionik berturut-turut (PTBLIB). SSDTK yang direka dengan MS–PEPG yang dioptimumkan, anod yang dioptimumkan dengan 5 kitar PTBLIB dan platinum (K) [FTO / TiO_2 / CdS(5) /elektrolit / Platinum(K) / FTO] menunjukkan prestasi terbaik dengan kecekapan penukaran kuasa (*PCE*) (0.77 ± 0.01)%, ketumpatan arus litar pintas (J_{sc}) (4.54 ± 0.10) mA cm^{-2}, voltan litar terbuka (V_{oc}) (0.51 ± 0.01) V dan faktor pengisi (*FF*) (0.34 ± 0.03). Anod QDSSC kemudian dimendapkan dengan lapisan passivasi ZnS dan SIO_2 dan membentuk sel dengan tatarajah: [FTO / TiO_2 / CdS(5) / ZnS /SiO_2 / elektrolit / Platinum(K)] memperlihatkan peningkatan prestasi dengan *PCE* (1.34 ± 0.13)%, J_{sc} (7.09 ± 0.27) mA cm^{-2}, V_{oc} (0.56 ± 0.04) V dan *FF* (0.34 ± 0.01) telah diperolehi. Akhirnya, kerja diteruskan dengan menyiasat bahan yang lebih baik untuk digunakan sebagai K. Dua bahan telah digunakan sebagai CE iaitu emas (Au) dan plumbum sulfida (PbS). SSDTK yang dibuat dengan PbS K [FTO / TiO_2 / CdS(5) / ZnS / SiO_2 / elektrolit / PbS(K)] menunjukkan prestasi terbaik dengan *PCE* (2.83 ± 0.07)%, J_{sc} (9.54 ± 0.16) mA cm^{-2}, V_{oc} (0.60 ± 0.02) V dan FF (0.49 ± 0.03).

Kata kunci: polisulfida elektrolit polimer gel, metilselulosa, sel suria titik kuantum tersensitasi

ACKNOWLEDGEMENTS

In the name of Allah Most Gracious and Merciful. Salawat and salam to the beloved Prophet Muhammad SAW. Alhamdulillah, all admirations go to Allah for giving me strength, patience and courage in completing PhD. I would like to express my gratitude to my supervisors, Prof. Dr. Abdul Kariem bin haji Arof and Dr. Hamdi bin Ali@Buraidah who gave me guidance, advice, support, and inspiration in completing this research journey. They were my mentors who is loaded with knowledge, always stimulate me to discover the knowledge and never stingy in sharing knowledge.

I would like to thank all to the members and officers in Centre for Ionics University of Malaya (C.I.U.M) for their help, kindness and guidance through this research journey. Further, a big appreciation also dedicates to all my friends who are always gave me moral support to complete this journey. And also, I want to thanks all the technical and administrative staff in the Department of Physic, Faculty of Science, IPS and University of Malaya as a whole who are involved directly or indirectly in this research journey.

I would like to acknowledge the financial support from the Ministry of Higher Education (Fundamental Research Grant Scheme FGRS 054–2014A and FP053–2016), the University of Malaya (Program grant RP003D-13AFR) and the Swedish Research Council (Swedish Research Links Grant: 2014-4284).

Last but not least, I would like to express an appreciation to my beloved parents (Mingsukang bin Paraman and Aminah binti Shahid) for their support, unceasing prayers and encouragement in this journey from my very first day in this world until now. Also not forgotten to all my sibling (Mawati, Hazlin, Hafiz, Fauziah, Fakhri and Zulhilmi).

LIST OF CONTENTS

CHAPTER 1: INTRODUCTION

CHAPTER 2: LITERATURE REVIEW

CHAPTER 3: EXPERIMENTAL METHODS

CHAPTER 4: RESULTS FOR CHARACTERIZATION AND OPTIMIZATION OF MC–PGPEs

CHAPTER 5: RESULTS FOR OPTIMIZATION OF PHOTOANODE

CHAPTER 6: RESULTS ON COUNTER ELECTRODE MATERIALS

CHAPTER 7: DISCUSSION

CHAPTER 8: CONCLUSION AND SUGGESTIONS FOR FUTURE WORK

LIST OF FIGURES

LIST OF TABLES

LIST OF SYMBOLS AND ABBREVIATIONS

α : Absorption

E_a : Activation energy

R_b : Bulk resistance

R_{dc} : Charge transfer resistance in symmetrical dummy cell

Q_{CE} : Constant phase element at CE/electrolyte interface

Q_{dc} : Constant phase element in symmetrical dummy cell

Q_{PA} : Constant phase element at photoanode/electrolyte interface

n_{CE} : CPE index at the interfaces of CE/electrolyte

n_{dc} : CPE index for symmetrical dummy cell

n_{PA} CPE index at the interfaces of photoanode/electrolyte

J : Current density

E_g : Energy band gap

FF : Fill factor

v : Frequency

ω : Frequency (angular)

Z : Impedance

R_{CE} : Interfacial resistance at CE/electrolyte interface

R_{PA} : Interfacial resistance at photoanode/electrolyte interface

σ : Ionic conductivity

D : Ionic diffusion

μ : Ionic mobility

n : Ionic number of density

l : Length

V_{oc} : Open circuit voltage

h : Plank's constant

R_s : Series resistance

J_{sc} : Short circuit current density

T : Temperature

V : Voltage

wt.% : Weight percentage

ATR : Attenuated total reflectance

CB : Conduction band

CBD : Chemical bath deposition

CE : Counter electrode

CPE : Constant phase element

DSSC : Dye sensitized solar cell

EDX : Energy dispersive X–ray

EIS : Electrochemical impedance spectroscopy

FESEM : Field effect scanning electron microscopy

FTIR : Fourier transform infrared

FTO : Fluorine tin oxide

GPE : Gel polymer electrolyte

h : Hour

IPCE : Incident current to current efficiency

IPGE : Iodide polysulphide gel polymer electrolyte

ILE : Iodide liquid electrolyte

MC : Methylcellulose

ML : Molecular linker

NIR : Near infrared

PGPE : Polysulphide gel polymer electrolyte

PLE : Polysulphide liquid electrolyte

PCE : Power conversion efficiency

PV : Photovoltaic

QDSSC : Quantum dot sensitized solar cell

QD : Quantum dot

QE : Quantum efficiency

RT : Room temperature

SILAR : Successive ionic layer absorption and reaction

SPE : Solid polymer electrolyte

UV–Vis : Ultraviolet–visible

V : Voltage

VB : Valence band

CHAPTER 1: INTRODUCTION

1.1 Background

Energy is the main issue that has been affecting human lives and environment since the beginning of the Industrial Revolution. Energy is needed in daily living to run existing technologies e.g. gadgets, automobiles, public transports, machines, etc. Energy crisis and global warming are two issues that are intensively discussed (Barreca, 2012; Lamb, 2016; Lewis & Nocera, 2006). The world's population in 2001 is around 6.1 billion and is expected to increase to 9.4 billion by 2050 (Lewis et al., 2006). The continuous increase in human population poses problems with regards to the world energy consumption, which will also increase in a proportionate trend with the increase in human population. Figure 1.1 shows the trends and projections of energy consumption between 1990 and 2050 for several countries and it also shows the estimated energy consumption from 2012 to 2050.

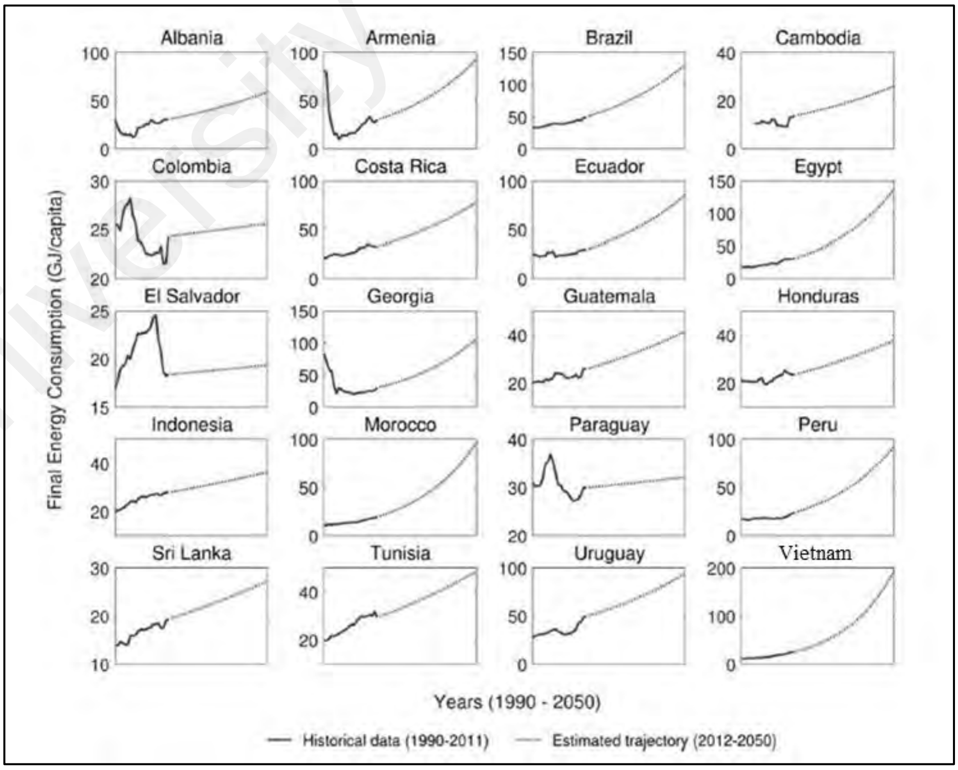

Figure 1.1: Trends and projections of energy consumption from 1990 to 2050 for several countries. It is estimated that energy consumption will increase every year (2012-2050) (Lamb et al., 2016).

The energy crisis is also an economy issue. Some examples of energy crisis are the shortage of energy resources and the increase in energy and fuel cost. The energy crisis can be attributed to population growth, political stress, war and geological factors. This crisis is more adverse in poor countries for example Africa and South Asia where the capita energy consumption for human basic needs is low (Lamb et al., 2015).

Global warming on the other hand is a very severe environmental problem where the earth's temperature increases with time due to the greenhouse effect. Greenhouse effect happens when a lot of the greenhouse gasses [e.g. carbon dioxide (CO_2), methane (CH_4), nitrous oxide (N_2O), etc] are trapped inside the earth's atmosphere. The greenhouse gasses contain the sun's energy and prevent the energy from leaving the earth's atmosphere. Consequently, a lot of heat energy is trapped inside the earth's atmosphere leading to increase in earth temperature. Energy production and consumption process are the main contributors to the greenhouse effect (Xu et al., 2016). The majority of electricity power plants use the combustion process to generate electricity and cars run on combustion engines. Both of these produce greenhouse gasses.

Renewable energy or green energy is believed to be the best solution to overcome the problem caused by the energy crisis and global warming. Renewable energy is energy that comes from sources which can be regenerated or renewed. Examples of renewable energy are solar power, hydro power, wind power and tidal power. The production and consumption of renewable energy will not harm the environment because there is negligible gas emission and waste product. Utilization of renewable energy to generate electricity as an alternative to the conventional electricity power plant could be one of the solutions to global warming. In addition, there is no running cost and maintenance of renewable energy utilization is low.

Among all the renewable energy resources, solar energy is considered as a very promising alternative to the conventional energy resources (i.e. fossil fuel and nuclear energy) (Nashed et al., 2013). This is because solar energy is the most abundant energy compared to other energies existing in this world. The amount of solar energy that reaches the earth for one year is around 3×10^{24} J, while the overall worldwide energy consumption was around 4.25×10^{20} in 2001 (Gratzel, 2005). Hence, the amount of solar energy reaching the earth is more than enough for human consumption. Thus, solar energy is the most promising energy source for the future and the most appropriate energy resource to replace the conventional energy sources that will be exhausted someday. Thomas Edison once said that "I would put my money on the sun and solar energy. What a source of power! I hope we don't have to wait until oil and coal run out before we tackle that".

The most popular way to harvest solar energy is by converting sunlight into electricity using a photovoltaic (PV) device or solar cell. Photovoltaic devices have been invented since the 19th century. Until now, there are a lot of development and research on photovoltaic device technologies to meet human needs. There are three generations of solar cells that has been developed. The first generation are solar cells based on bulk pure crystalline silicon with power conversion efficiency (*PCE*) around 25% (Blakers et.al, 2013). However, the production of the first generation solar cells is extremely costly. The fabrication cost of first generation solar is so expensive and this has led to the development of the second generation solar cells which has lower production cost compared to the first-generation solar cells. The second-generation solar cells are solar cells based on thin film technology. Second generation solar cells utilized a cheaper material compared to bulk pure silicon. These include amorphous silicon, copper indium diselenide and cadmium telluride. To further reduce fabrication cost, but with outstanding performance, third generation solar cells have been introduced. Third generation solar cells are low-cost solar cell with better performance to price ratio and simple preparation procedures (Späth et al., 2003). Examples of third generation solar cells are dye sensitized solar cells (DSSCs), QDSSCs and perovskite solar cells. It is to be noted that the production cost of the first generation solar cells has reduced. However, the third generation cells are still cheaper.

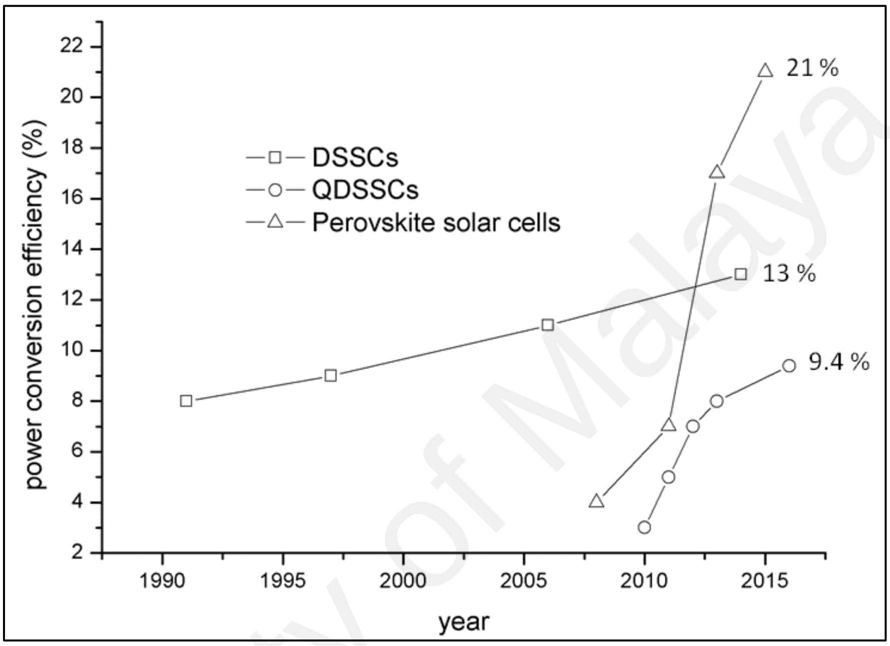

Figure 1.2: The progress of third-generation-sensitized solar cells (Mingsukang at al., 2017)

Among all three generation solar cells, third generation solar cells can be considered as the ultimate solution to the energy crisis and global warming. This is due to its low production cost and better performance to price ratio compared to other types of solar cells. In addition, the performance of third generation solar cells is expected to surpass the other types of solar cells as the development stage for the third-generation solar cells is still young (Charles et al., 2016). In addition, the progress of third-generation solar cells is considered faster compared to the earlier generation solar cells (Green, 2009). This can be seen as the *PCE* of third-generation-sensitized solar cells reached ~21% within 20 years and the performance is expected to increase (Park, 2015). Figure 1.2 shows the progress of third-generation-sensitized solar cells (DSSCs, QDSSCs and perovskite solar cells).

One of the famous third generation solar cells is the mesoporous–TiO_2 based DSSCs that has been introduced by O'Regan & Gratzel, 1991. The development of mesoporous–TiO_2 based DSSC by O'Regan & Gratzel, 1991 has triggered a lot of researchers to develop/study and improve the performance of DSSCs. As the research of DSSCs grows actively, some researchers have come out with the idea of replacing organic dyes with inorganic quantum dots (QDs), hence the name quantum dot sensitized solar cells (QDSSCs) emerged. Since the 90s, there has been a lot of work on replacing organic dyes with QDs in mesoporous–TiO_2 based DSSC that has been architectured by O'Regan & Gratzel, 1991 (Liu et al., 1993; Vogel et al., 1994; Vogel et al., 1990). Until now, Luther's group reported the highest performance of the QDSSC with *PCE* of 13.43% (Sanehira et al., 2017).

Usually polysulphide liquid electrolyte (PLE) is used as a medium for charge transfer in QDSSCs. However, PLE in QDSSCs will pose problems of vaporization, instability in performance and difficulty in handling. Due to the problems stated, researchers have turned to polymer electrolytes. Polymer electrolytes can be divided into two categories which are solid polymer electrolytes (SPEs) and gel polymer electrolytes (GPEs) (Chen et al., 2013; Duan et al., 2015; Duan et al., 2014; Kim et al., 2014). QDSSCs fabricated with SPE show weak performance due to the low ionic conductivity of solid–state electrolytes. However, QDSSCs fabricated with GPE show an outstanding performance comparable to QDSSCs with liquid electrolytes and some of them have reached *PCE* around 8% (Feng et al., 2016; Kim et al., 2014).

In this work, a novel polysulphide GPE (PGPE) has been prepared comprising methylcellulose (MC) as host polymer. MC is the derivative of cellulose and its chemical structure is as shown in Figure 1.3 (Kamitakahara et al., 2008). Due to its excellent properties, MC has been widely used in food, pharmaceutical and tissue engineering industries (Farris et al., 2009; Ozeki et al., 2005; Reverchon et al., 2009). Commercially, MC is prepared by reacting cellulose with aqueous sodium hydroxide (NaOH) and methyl chloride (Kobayashi et al., 1999). The methylation process of cellulose can be controlled by regulating the concentration of NaOH and reaction temperature.

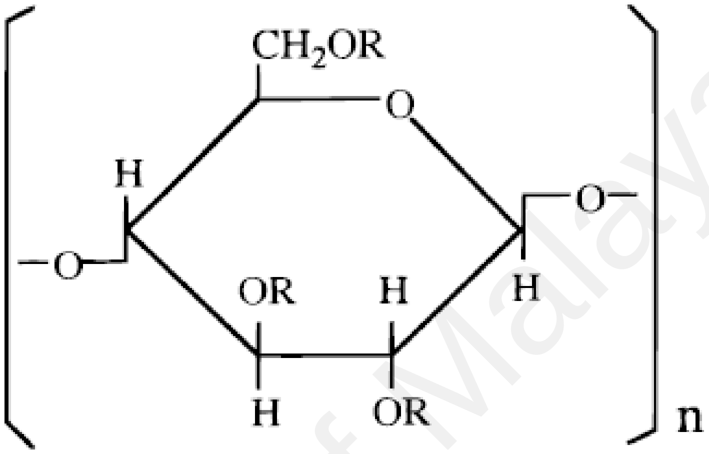

Figure 1.3: MC chemical structure (R = H or CH_3).

MC is abundantly available, cheap, non-toxic and biocompatible. In addition, MC is soluble in water so that sodium sulphide (Na_2S) can be incorporated into it to make it a polysulphide electrolyte. In preparation of the polysulphide electrolyte, it should be noted that there are no other solvents except water to dissolve Na_2S (Kurzin et al., 2010). Therefore, selection of host polymer in PGPE system is restricted to the polymers that have the ability to dissolve in water. So far, no work has been reported on MC–PGPE electrolyte for application in QDSSCs (Mingsukang et al., 2017).

Cadmium chalcogenides (CdS, CdSe and CdTe) is a type of quantum dots that have been frequently used as sensitizers in QDSSCs studies (Jun et al., 2013; Peter, 2011; Rhee et al., 2013). This is because preparation and deposition of cadmium chalcogenides on the surface of TiO_2 is easy. Moreover, the cadmium chalcogenides have conduction bands suitable for electron injection into the TiO_2. It has been proven that utilization of cadmium chalcogenides as sensitizer in QDSSCs will give excellent performance. For example, QDSSCs with *PCE* over 9% have been fabricated by Yang et al. (2015) with alloyed cadmium chalcogenide CdSeTe sensitizer. Another example is the work done by Ren et al. (2015) that achieved *PCE* over 9% which also utilized CdSeTe as sensitizer. Due to the fascinating properties of cadmium chalcogenides as the sensitizer in QDSSCs, CdS has been the choice in this work.

One of the major problems in QDSSCs is electron recombination. Electron recombination happens when electrons produced in the photoanode combined with the S_x^{2-} ions in the electrolyte. S_x^{2-} ions are formed when the sulphide ions (S^{2-}) react with the sulphur (S) contained in the electrolyte (refer QDSSC working mechanism in Chapter 2). In order to avoid the recombination problem in this work, a combination of two types of passivation layer will be deposited on the photoanode with CdS QDs sensitizer. These are zinc sulphide (ZnS) and silicon dioxide (SiO_2) layers. ZnS and SiO_2 are well-known materials used as a passivation layer as they effectively hinder the electron from the photoanode to recombine with the S_x^{2-} ions in the electrolyte (Liu et al., 2010; Tubtimtae et al., 2012).

In sensitized solar cells research, platinum is the commonly used material for counter electrode (CE) due to its superior and stable performance to the sensitized solar cells especially in DSSCs. Hence, platinum has been widely used in many QDSSC studies. However, many reports on QDSSC studies that utilize platinum as CE show poor performance. Utilization of platinum resulted in low fill factor and eventually affected the *PCE* of the device. Therefore, some studies have proposed that platinum is not a suitable material to be utilized as CE in QDSSCs since it can react with the sulphur compound in the electrolyte and inhibits charge transfer from CE to the S_x^{2-} ions in the electrolyte (Radich et al., 2011). To find the alternative to the platinum CE which is compatible with novel MC–PGPEs introduced in this work, gold (Au) and lead sulphide

(PbS) have been chosen as alternative CEs. Au has similar properties with platinum such as stability and catalytic toward reduction of redox mediator in the electrolyte (Seo et al., 2011). Metal chalcogenides is a popular material used as an alternative to the Pt CE in QDSSC and PbS has been chosen in this research due to its ability to form auxiliary tandem effect which will improve the device performance (Lin et al., 2013). Auxiliary tandem effect happens when the CE could act as photocathode that will improve J_{sc} and V_{oc} of the device. Auxiliary tandem effect will be discussed more in Chapter 2 (literature review).

1.2 Problem Statement

Utilization of the polysulphide liquid electrolyte (PLE) in the QDSSCs will cause problems such as vaporization, instability in performance and difficulty in handling. Polymer electrolyte is a suitable option to overcome this problem. However, selection of the polymer for the polysulphide electrolyte system is a great challenge since the salt used is only soluble in water and stability of the polymer is important. Hence, MC has been chosen as it is soluble in water and can be dissolved together with the Na_2S salt.

Another challenge for the QDSSC with the novel MC–based polymer electrolyte is its electrodes i.e. photoanode and CE. Selection and optimization of the electrodes in the QDSSC is important since it is unclear how the MC–based polymer electrolyte would affect the device performance in terms of electrochemical aspects.

1.3 Objectives

The ultimate aim of this research work is to develop and optimize CdS based QDSSCs with a novel methylcellulose–polysulphide gel polymer electrolyte (MC–PGPE) that will be introduced in this dissertation. The research will focus on all three components of QDSSCs which are electrolyte, photoanode and CE. The objectives of this research work are listed bellows:

1. To develop and optimize the conductivity of the PGPE system using methylcellulose as host polymer.

Due to the solubility issue, the host polymer in the PGPE must be soluble in water in order to enable the use of Na_2S salt in the electrolyte. In this work, MC has been chosen as the host polymer. So far, no work has been reported with MC as the host polymer for PGPE.

2. To optimize photoanode sensitized with CdS

The QDSSCs fabricated part will use platinum (Pt) as a CE and optimized MC–PGPE from first objective as the electrolyte. SILAR method will be used to attach the CdS quantum dots on the photoanode. Hence investigation on the optimized number of SILAR cycles will be carried out. To avoid electron recombination problems in QDSSCs at the photoanode/electrolyte interface, passivation layers will be introduced as it could help improve the overall performance of the MC–PGPE based QDSSCs.

3. To investigate the alternative material for counter electrode

In the last part of this work, QDSSCs will be fabricated with optimized MC–PGPE and optimized photoanode while CE used is either Au or PbS. Pt is the best material to be used in application of sensitized solar cells. However, there are many reports on Pt that claimed it is not a suitable material for CE of QDSSCs utilizing polysulphide–based electrolyte. Pt reacts with sulphur compounds and eventually will hinder the charge transfer form CE to the electrolyte. To avoid this problem, an alternative CE material will be investigated. Au is also chosen as an alternative CE due to its similar properties as Pt such as high conductivity and can act as good catalyst for charge transfer at interface of CE and electrolyte while PbS was chosen since it could provide auxiliary tandem effect in the device.

1.4 Scope of Dissertation

This dissertation contained eight chapters. Chapter 1 discusses research background objectives and dissertation content. Chapter 2 is an overview on QDSSCs working principle, components and comparison of the QDSSCs studies reported in the literature. Chapter 3 describes all experimental details that have been done in this work including preparation, optimization, characterization and fabrication of MC–PGPE, photoanode, CE and QDSSCs. Chapter 4 displays results on all investigations and optimizations carried out to achieve the first objective of this research i.e. to develop and optimize the conductivity of the PGPE system using MC as host polymer. Chapter 5 displays results on all investigations and optimizations carried out to achieve the second objective of this research i.e. to optimize photoanode sensitized with CdS. Chapter 6 displays results on all investigations and optimizations carried out to achieve the third objective of this research i.e. to investigate the alternative material for CE. Chapter 7 discusses all the investigations and optimizations carried out in this work. There are three sections within Chapter 7: Section 7.2 discusses on optimization and characterization of MC–PGPE, Section 7.3 discusses the results on optimization and characterization of CdS photoanode and Section 7.4 Investigations of alternative materials for CE. Section 7.2, 7.3 and 7.4. discuss and analyse the result from Chapter 4, 5 and 6 respectively. Finally, Chapter 8 draws the overall conclusion and plans for future work.

CHAPTER 2: LITERATURE REVIEW

2.1 Introduction

Quantum dot sensitized solar cell (QDSSC) is an electrochemical device that functions to convert solar energy into electricity using quantum dots (QDs) to produce charge separation. QDSSCs was categorized as the third generation solar cell along with dye sensitized solar cells, perovskite solar cells, organic solar cells and polymer solar cells. Compared to the earlier generation solar cell technologies, third generation solar cells have a great potential for giving an outstanding performance with cheap production cost. Due to the high performance to production ratio, third generation solar cells have been actively researched to improve performance and stabilize the device. The idea of QDSSCs emerged as researchers tried to replace the organic dye in DSSCs with an inorganic nano sized semiconductor (quantum dot). QDSSCs and DSSCs have the same operating mechanism and components except for the sensitizer part. QDSSC has three important components which are photoanode (anode), electrolyte and counter electrode (cathode). In order to get the best performance and stability, a lot of research on all three QDSSC components must be done.

This chapter composes of three main sections i.e. Sections 2.2, 2.3 and 2.4. Firstly, this chapter will discuss on the working mechanism of QDSSC and followed by a discussion on QDSSC components, which are photoanode, electrolyte and counter electrode (CE). The last section compares QDSSCs studies reported in the literature. The comparison emphasizes the materials used for the components and its overall performance (*J–V* characteristics).

2.2 QDSSCs Working Mechanism

QDSSC has three important components: photoanode as a charge producer, CE as cathode and electrolyte as the charge transport medium between CE and photoanode. Electricity generation process in QDSSC is similar to that of DSSC. Sensitizer used in QDSSCs is inorganic quantum dot material while DSSCs used organic dye (Peter, 2011; Yeh et al., 2011). Figure 2.1 shows a schematic illustration for better understanding on QDSSC working mechanism.

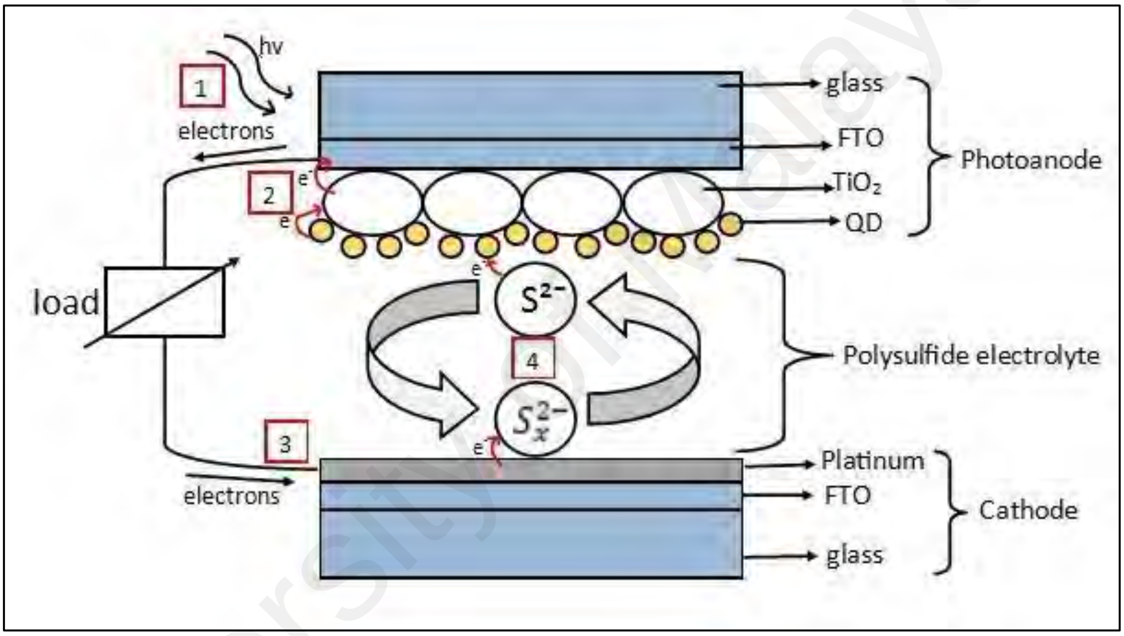

Figure 2.1: An illustration on how the QDSSC generate electricity (Mingsukang et al., 2017).

The generation of electricity in QDSSC starts with electrons from the valence band (VB) of the QD being excited to its conduction band (CB). The energy for excitation is gained from the incoming photons (*hv*). As the electrons leave the QDs, holes are left in the VB of the QD. With sufficient amount of energy, excited electrons in the CB of QD is injected into the CB of the wide band gap semiconductor (TiO$_2$). As electrons enter the TiO$_2$, the QD is in the state of electron deficiency. From CD of TiO$_2$, electrons migrate to the substrate (glass) conducting layer and reach the CE through the external circuit. At the CE/electrolyte interface, electrons from the photoanode are received by the S_x^{2-}ions (redox mediator), which are then transformed into S^{2-} ions. This is represented by Equation (2.1). The process described by Equation (2.1) occurs at the CE/electrolyte interface (Yang et al., 2011):

$$S_x^{2-} + 2e^{2-} \rightarrow S_{x-1}^{2-} + S^{2-} (x = 2 - 5) \tag{2.1}$$

The S^{2-}ions diffuse to the photoanode and transfer electrons to the electron deficient QD molecules. Equations (2.2), (2.3) and (2.4) describe the chemical processes that occur at the photoanode/electrolyte interface (Yang et al., 2011). Equation (2.2) shows that S^{2-} ions donate electrons to the QD molecules and transform into S (intermediate form). Equation (2.3) shows the same process, but involving holes. Equation (2.4) describes the transformation of S into S_x^{2-} ion by combining with S_{x-1}^{2-} ion.

$$S^{2-} \rightarrow S + 2e^- \tag{2.2}$$

$$S^{2-} + 2h^{2+} \rightarrow S \tag{2.3}$$

$$S + S_{x-1}^{2-} \rightarrow S_x^{2-} \tag{2.4}$$

Electricity is eventually produced when the circuit is completed when the holes in the QDs have been filled by electrons, see Figure 2.1. The magnitude of photocurrent produced depends on the number of effective electrons that succeed to complete the whole circuit. The number of electrons produced depends on how effective the QDs produce electrons while the amount of electrons that succeed to complete the whole circuit i.e. photocurrent depends on many factors that will be discussed in the later part of this thesis. These factors include recombination rate at the photoanode/electrolyte interface, morphology of QDs attached on the wide band gap semiconductor, conductivity of the electrolyte and catalytic degree of the CE (Feng et al., 2016; Radich et al., 2011; Shen et al., 2008; Sun et al., 2008). Photovoltage generated in the QDSSC also depends on so many factors but the major contribution to the photovoltage is the difference between the quasi-Fermi level of the photoanode and the redox potential of the polysulphide electrolyte (Sayama et al., 1998). An illustration on the difference between the Fermi level of the photoanode and redox potential in the electrolyte can be seen in Figure 2.2:

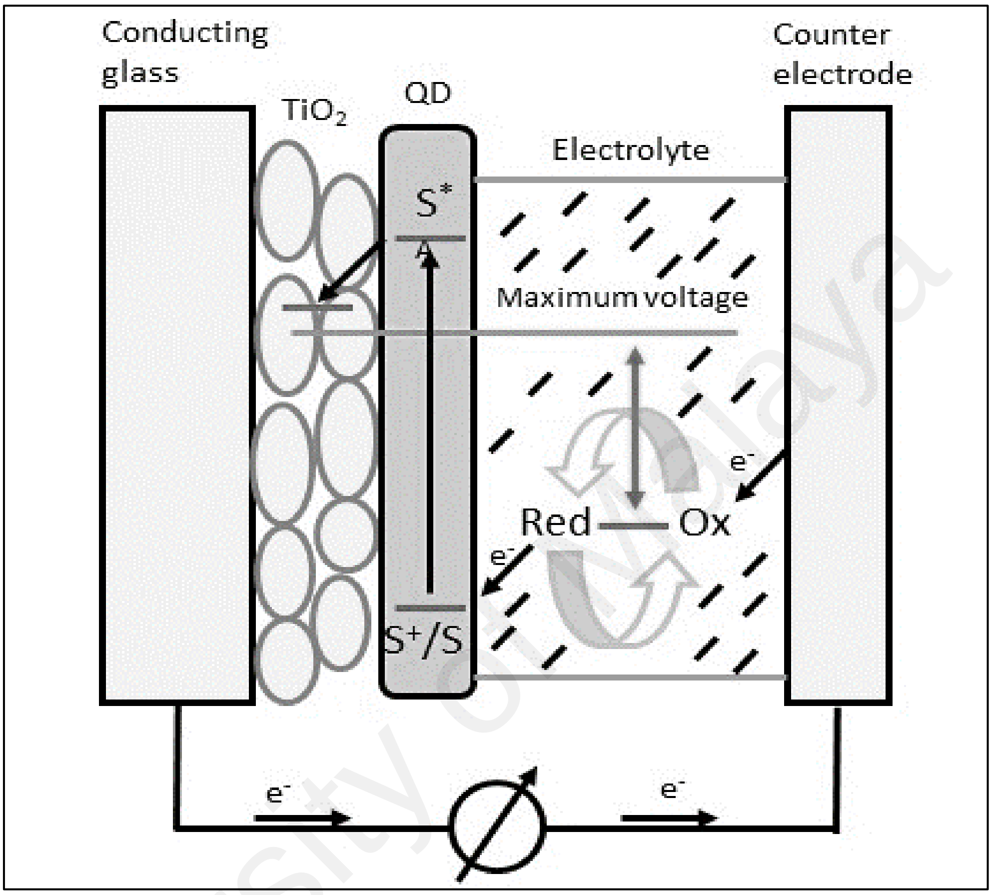

Figure 2.2: Generation of voltage in QDSSC.

2.3 QDSSC Components

As mentioned in the previous section, the working principle and components of the QDSSC are similar to that of DSSC. QDSSC has 3 main components which are photoanode, electrolyte and CE (refer Figure 2.1). Although QDSSC and DSSC have the same working principle and components, the sensitizing materials used in both devices are different. Also, compatibility of the chemicals used in the components need to be considered. For instance, DSSCs with iodide–based electrolytes will give excellent performance, however utilization of iodide–based electrolytes in QDSSCs will give a bad performance (Chang et al., 2007; Shalom et al., 2009). In this section, each QDSSC component will be discussed:

2.3.1 Photoanode

Generally, the structure of QDSSC photoanode resemble the very famous structure of DSSC photoanode introduced by Gratzel et al. (1991). The photoanode consists of a fluorine doped tin oxide (FTO) glass substrate with mesoporous metal oxide layer of wide band gap semiconductor (e.g. TiO_2, ZnO and SnO_2) and QDs sensitizer (e.g. CdS, CdSe, CdTe and Ag_2S) (Vogel et al., 1994). Figure 2.3 shows a simple illustration for a QDSSC photoanode. The QD sensitizer is a charge or electron producer. The wide band gap TiO_2 functions as the electron collector produced by QD sensitizer. The passivation layer is an additional component that can suppress recombination of electrons with the S_x^{2-} ions in the electrolyte. This can be explained using the chemical reaction: $\mathrm{S_x^{2-}} + 2\mathrm{e}^{2-} \rightarrow \mathrm{S_{x-1}^{2-}} + \mathrm{S^{2-}}(\mathrm{x} = 2 \text{ to } 5)$. It has been proven that QDSSCs with passivation layer exhibited better performance compared to without passivation layer.

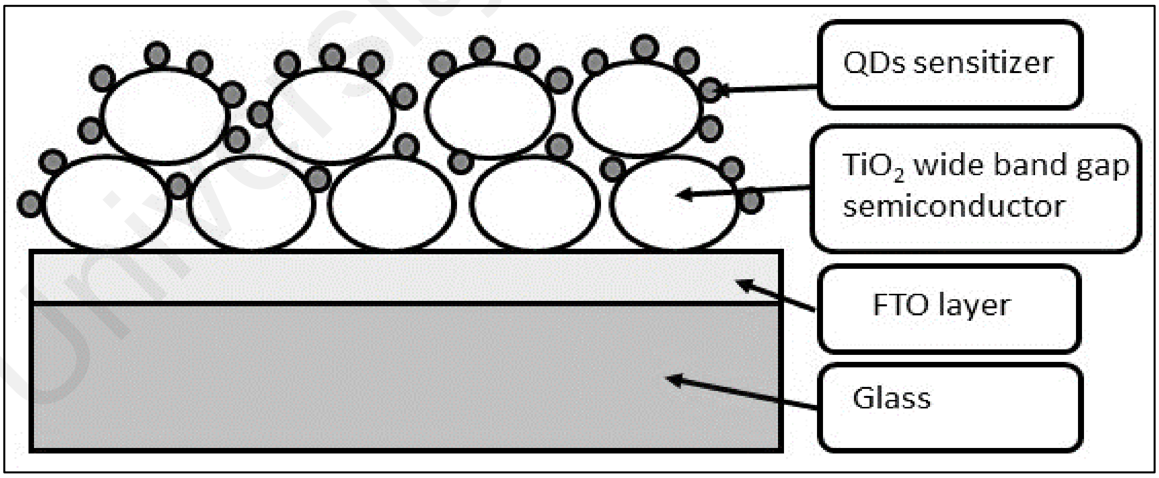

Figure 2.3: A simple illustration for understanding the structure of QDSSC photoanode.

The metal oxides such as TiO_2, zinc oxide (ZnO) and niobium oxide (Nb_2O_5) have the ability of providing mesoporous and ordered structure (Ren et al., 2012). In the field of sensitized solar cells, the mesoporous structure of metal oxide semiconductor is crucial for sensitizer adsorption since a mesoporous structure could provide more surface area for sensitizer loading. One of the common metal oxides widely used in many applications due to its excellent properties is TiO_2. TiO_2 has been used in many research on sensitized solar cells since it can be prepared to provide a mesoporous structure, suitable band adjustment for electron injection from the sensitizer (refer Figure 2.4) and high electron mobility for photo-generated electron (Marie-Isabelle, 2012).

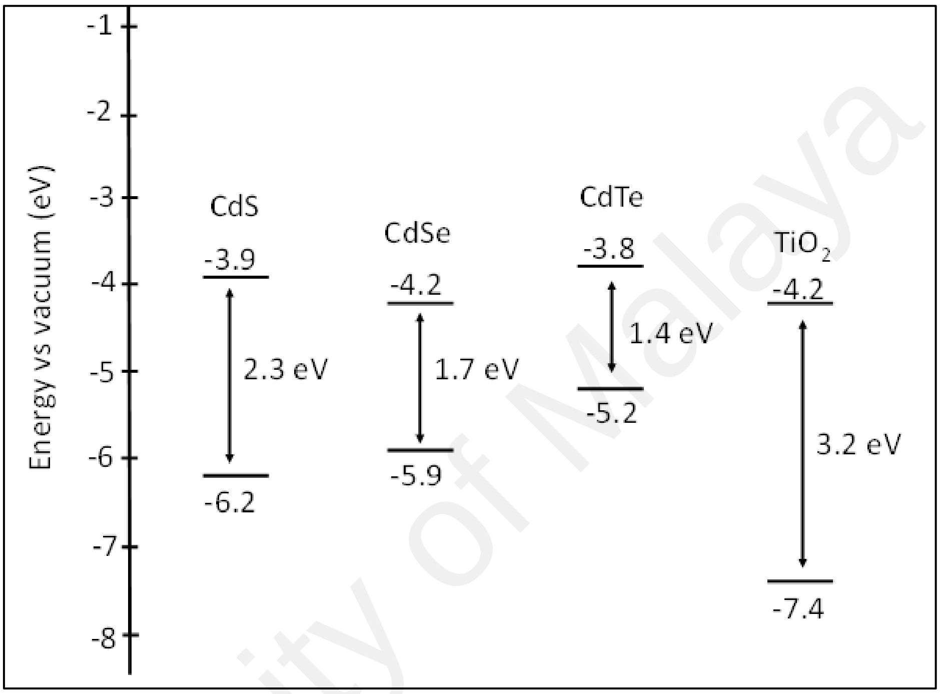

Figure 2.4: Energy levels of cadmium chalcogenide quantum dots and TiO_2 (Mingsukang et al., 2017).

QDs are semiconductors with nano-range dimensional structures and possess narrow band gap suitable for absorbing light. Its size ranges from 1 to 10 nanometres and its optical and electronic properties are different from its bulk size. Due to its fascinating properties, QDs have been used in many applications such as light emitting diodes (Gong et al., 2016), display devices (Patel, 2012), photodetector (De Iacovo et al., 2016), photovoltaics (Jasim, 2015) and photocatalysis (Caputo et al., 2017).

After Gratzel and co-workers introduced highly porous TiO_2 DSSC, a lot of research has been geared to replace the organic dye sensitizers with inorganic QDs (Liu et al., 1993; Vogel et al., 1994; Vogel et al., 1990). QDs exhibit several advantages over organic dyes such as easier to produce and good durability (Lee et al., 2009). Another advantage is the tuneability of its band gap (Chang et al., 2007). Also QDs can produce two excitons per photon with hot electrons i.e. ionization impact (Nozik, 2005). With their high extinction coefficient, QDs can reduce dark current in the photovoltaic device (Lee et al., 2009). Furthermore, the theoretical *PCE* for QDSSCs was 44%, after consideration of carrier multiplication due to ionization (Hanna et al., 2006).

Cadmium chalcogenides are the most frequently used QD sensitizers in QDSSCs research due to their excellent traits that consequently give good impact to the performance of the QDSSCs (Peter, 2011; Rhee et al., 2013). Cadmium chalcogenides can be easily prepared and their band gaps can be tuned by manipulating their sizes. The band gap of CdS, CdSe and CdTe of 2.3, 1.7 and 1.4 eV respectively. The range of light wavelength that can be absorbed by CdS, CdSe and CdTe is 350–540 nm, 350–731 nm and 350–887 nm respectively. There are a lot of works reported on the combination of two sensitizers in a single cell for example combination of CdS/CdSe, CdTe/CdSe and CdTe/CdS (Lee et al., 2009; McElroy et al., 2014; Yu et al., 2011). The contact between two QD sensitizers will give rise to a phenomena of electron redistribution resulting in the band edge of the quantum dot sensitizer to shift to a more positive or less positive potential respectively. The shifting process of band edge is referred to Fermi level alignment (Lee et al., 2009). The effective electron injection that resulted from the combination of CdTe/CdSe and CdS/CdSe are shown in Figure 2.5. In addition, the combination of two quantum dot sensitizers in one cell could widen the range of the wavelength of light that can be absorbed (Pan et al., 2012).

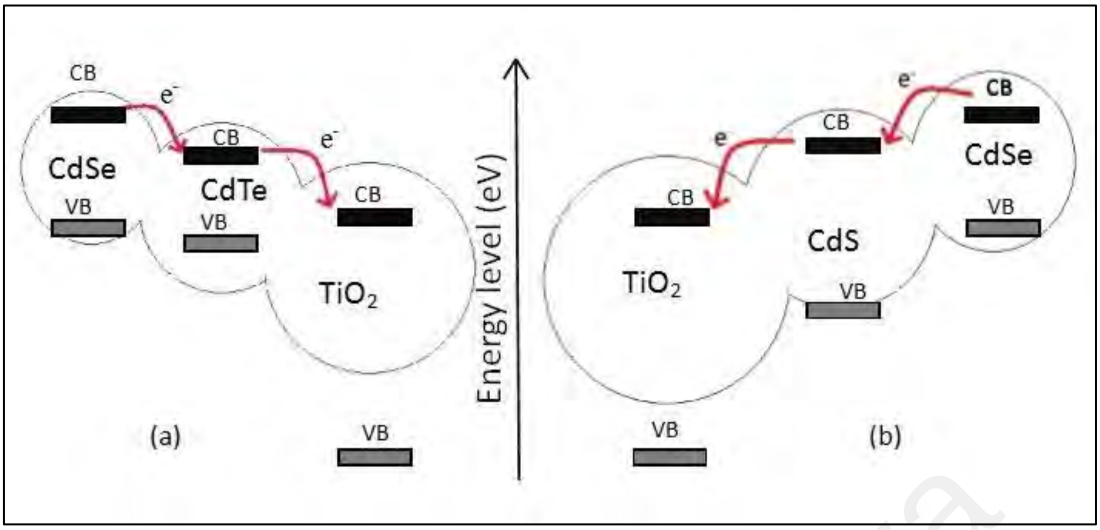

Figure 2.5: Band gap edge level of QD sensitizers after electron distribution in: (a) CdTe/CdSe and (b) CdS/CdSe due to Fermi level alignment favouring electron injection into TiO_2 (Mingsukang et al., 2017).

The ability to tune the band gap of QD sensitizers to improve the performance of QDSSCs can lead to stability problem (Wang et al., 2007). To counter this problem, alloyed cadmium chalcogenides QD sensitizers have been introduced to manipulate the band gap of the QD sensitizer without altering the size of the particle (Bailey et al., 2003; Wang et al., 2007). Alloyed cadmium chalcogenides have the structure of AB_xC_{1-x} where A is Cd, B and C are either S or Se or Te. $CdTe_xS_{1-x}$ is one of the alloyed QD sensitizer example that has been used in the fabrication of QDSSCs. The band gap of $CdTe_xS_{1-x}$ quantum dot sensitizer can be altered by changing the molar ratio of tellurium so that the QDSSC fabricated will absorb light in the visible and favour the performance of the QDSSC (Badawi et al., 2014). Another outstanding alloyed cadmium chalcogenide QD sensitizer utilized in QDSSC is $CdSe_xTe_{1-x}$. Utilization of $CdSe_xTe_{1-x}$ in QDSSCs show excellent performances with *PCE* of over 9% (Ren et al., 2015; Yang et al., 2015).

There are various methods used to deposit QD sensitizer to the TiO_2 wide band gap semiconductor. Among all the methods available, three methods were considered as major methods. The methods are chemical bath deposition (CBD), successive ionic layer and reaction (SILAR) and molecular linker (ML) attachment. CBD is the simplest and easiest method to deposit the QD sensitizer. In CBD, the growth of QD sensitizer on the TiO_2 is simply by soaking the TiO_2 layered photoanode in the solution containing cationic and anionic precursors of the desired QD. For example, deposition of CdS QDs is simply by soaking the TiO_2 layered assembly in the solution consist of cadmium acetate ($Cd(CH_3COO)_2$) and sodium sulphide (Na_2S). The cadmium salt contributes Cd^{2+} and the sodium sulphide salt contributes S^{2-} ions respectively. By varying the soaking time, the deposition of quantum dot sensitizer can be controlled. This method has been used to deposit CdS (Al-Azab et al., 2000), CdSe (Choi et al., 2014), CdTe (Daud et al., 2012) and many more. However, the yield is low (Hariskos et al., 2001). In addition, this method takes a long time to perform which are not effective for industrial usage. The product is sodium acetate that insoluble in water.

SILAR method is an advancement of the CBD method. In CBD method, the cations and anions are combined in one solution while in SILAR method, the cation and anion are separated in two different solutions. By using this method, the deposition of QD sensitizer to the TiO_2 layer can be controlled by controlling the number of SILAR cycles. One SILAR cycle is when the TiO_2 layer in the photoanode undergo two soaking processes (Lindroos et al., 2000): the TiO_2 layer photoanode is first soaked in a solution containing the desired cation ions for a certain time followed by rinsing and drying. During the first dipping process, the desired cations adsorbed to the TiO_2 surfaces. This process resembles the hydrolysis of metal ion reaction. The TiO_2 is then soaked again in a solution containing the desired anions for the same length of time as for the cations. This is then followed by rinsing and drying. During the second dipping process, the anions in the solution react with the adsorbed cations on the surface of TiO_2 to form the desired QD. Example of SILAR method for deposition of CdS QDs is the study carried out by Mukherjee et al. (2015) which composed of two dipping processes. The first dipping process witnessed the substrate being dipped into cadmium chloride (CdCl) solution followed by rinsing and drying. Then the substrate was dipped in ammonium sulphide ($(NH_4)HS$) solution followed by rinsing and drying process. SILAR method has a number of advantages such as (Lokhande et al., 2004):

- Simplicity, inexpensive, easy to perform, appropriate for large area deposition, does not require substrates with high quality and it can be performed in normal atmospheric condition. These advantages are favourable in industrial application.
- The deposition condition can be controlled by controlling the number of cycles.
- The deposition can be done on the less robust materials.
- There are no limitations on substrates condition such as surface profile and its dimensions.

The third major method used in QDSSCs research is the deposition through a molecular linker (ML). Deposition of cadmium chalcogenides to the TiO_2 layered photoanode using this method has been first reported by Murray et al. (1993). The molecular linker is a special molecule that has two functional groups. One of the functional groups can attach to the TiO_2 surface and the other is responsible for capping the QD sensitizer. By using this method, size, optical properties and shape of the QD sensitizer can be controlled depending on the type of molecular linker used. Examples of molecular linkers that have been used for deposition of QD sensitizer include mercaptopropionic acid (MPA) (Gao et al., 2014), trioctylphosphine (TOP) (Villarreal et al., 2011) and trioctylphosphine oxide (TOPO) (Kashyout et al., 2012). The deposition usually starts with the process of capping the QD sensitizers with the molecular linker by simply mixing the solution containing the molecular linker with the solution containing the desired QD at a certain temperature. After completing the process of QD capping, the TiO_2 layered assembly was soaked into the solution containing the QD sensitizers capped with molecular linker. However, the soaking process takes a long time from a few hours to few days. Compared to the SILAR method, this method is very time consuming.

One of the major problems in QDSSCs is that the cells suffer from very high recombination rate at the photoanode/electrolyte interface (Tubtimtae et al., 2012). Recombination process is a parasitic process that will reduce the cell's performance. Recombination happens when the electron produced does not result in the generation of electricity. In QDSSC, excited electrons produced by QD sensitizer follows one of three possible routes. The first route is the excited electrons are injected into the conduction band (CB) of TiO_2. The electrons find their way to the CE via the external circuit and sent are back to regenerate the QDs through the S_x^{2-}/S^{2-} redox mediator. Completion of the full passage of the electrons generates electricity. The second route returns the excited electrons back to the VB of the QD and emits energy. The final route is the recombination with the S_x^{2-} ions in the electrolyte. A passivation layer is a successful strategy to reduce the recombination rate in the QDSSC (Guijarro et al., 2011). ZnS is an example of passivation layer to overcome the recombination problem in QDSSC. Other examples include SiO_2 and a thin layer of amorphous TiO_2 (am-TiO_2) (Yang et al., 2015). Ren et al., 2015 have reported a new strategy to suppress the recombination of electrons in QDSSCs by introducing three passivation layers which are am-TiO_2/ZnS/SiO_2 resulting in *PCE* of 9%. Thus, the passivation layer is considered as the important part in the photoanode of the QDSSCs.

2.3.2 Electrolyte

In sensitized solar cells, electrolyte plays a crucial role as a medium for charge transfer between the CE and photoanode. Charge transfer is via the redox mediator ions (S^{2-}/S_x^{2-}). S^{2-} ions are responsible for the transfer of electrons from the electrolyte to photoanode while S_x^{2-} ions are responsible for the transfer of electrons from the CE to the electrolyte. The redox mediator ions are therefore responsible for replenishing the oxidized QD sensitizers by providing electrons to the QD sensitizers. In DSSC research, iodide–based electrolyte has some beneficial properties toward the cell's performance and has been widely used (Yasuo et al., 2006). However, utilization of iodide–based electrolyte in QDSSCs will give a negative impact on the cell performance. This is because of iodide–based electrolyte could erode and destroy the QD sensitizers which eventually leads to a drop in overall cell performance (Chang et al., 2007; Samadpour et al., 2011; Shalom et al., 2009). Since iodide–based electrolytes are not compatible with QDSSCs, polysulphide–based electrolytes with S^{2-}/S_x^{2-} redox species has been used. Polysulphide–based electrolyte could provide stability and good performance of the QDSSC (Jun et al., 2013; Lee et al., 2008; Shalom et al., 2009). Majority of the high performance QDSSCs reported in the literature utilize liquid polysulphide–based electrolytes (Ren et al., 2015; Yang et al., 2015; Zhao et al., 2015). Utilization of liquid electrolytes in QDSSC pose several problems as mentioned before. This will eventually affect the performance of the device. The problems are leakage of the electrolyte and its vaporization that could cause instability in the cell performance. It is also difficult to fabricate QDSSC using liquid electrolyte. Due to this difficulty and problems caused by utilization of liquid electrolyte in QDSSCs, researchers have turned to polymer electrolytes. Polymer electrolytes have a great potential to overcome the problems caused by liquid electrolytes and have been used in many electrochemical devices such as electrochromic windows (Solovyev et al., 2016), solar cells (Nei et al., 2009), batteries (Long et al., 2016) and supercapacitors (Ortega et al., 2016).

Generally, polymer electrolytes can be classified into two major types which are solid polymer electrolytes (SPEs) and gel polymer electrolytes (GPEs). GPEs and SPEs have been used in order to overcome the problems and difficulties caused by utilization of liquid electrolytes (Duan et al., 2015; Duan et al., 2014; Kim et al., 2014; Yu et al., 2010). However, the reports on the implementation of SPEs in QDSSCs in literature showed weak performance compared to the QDSSCs fabricated with GPEs. The weak performance exhibited by QDSSCs fabricated with SPEs is due to the low ionic conductivity that limited ionic transport. The progress in development of GPE based QDSSCs is comparable with that of QDSSCs fabricated with liquid electrolyte. The highest *PCE* of QDSSCs fabricated with liquid electrolyte is around 9% while the highest *PCE* of the QDSSCs fabricated with GPEs is around 8% (Feng et al., 2016; Yang et al., 2015). Thus, it can be said that GPE is the best alternative to the liquid electrolytes for application in QDSSCs.

2.3.3 Counter Electrode

The electrons produced at the photoanode that succeeded in reaching the external circuit will be collected at the counter electrode (CE). From CE, electrons from the external circuit will be transferred back to the photoanode by the redox mediator ions in the electrolyte. Electron transportation properties at the CE/electrolyte interface will influence the performance of sensitized solar cells (Sixto et al., 2009). Ideal CE for the sensitized solar cells should possess two main criteria which are highly conducting and good catalytic properties (Lee et al., 2014). CE material with high conductivity property will provide easy pathway to the electrons in order to complete the circuit. Furthermore, series resistance (R_s) of the device will be lowered with the presence of highly conducting CE material and eventually will lead to the improvement of the *FF* and *PCE* of the device (Meng et al., 2015). Catalytic properties are an important characteristic for the CE material since it defines the rate of electrons transfer from CE to the S_x^{2-} ions. Materials with high catalytic properties will provide fast electron transfer while low catalytic material will cause slow rate of electron transfer.

Pt is the most popular material to be used as CE in sensitized solar cells. This is because Pt is stable and catalytic towards iodide–based electrolytes commonly used in DSSC studies. With Pt CE, reduction of I_3^- ions to I^- ions (movement of electrons from CE to the electrolyte) are faster and stable, which eventually favours the electron transfer process between CE and electrolyte. However, QDSSCs studies employing polysulphide electrolyte and platinum CE show poor performance with low *FF* and *PCE* (Jun et al., 2013; Lee et al., 2008; Mingsukang et al., 2017). The low *FF* value is due to instability in performance caused by problems arising from the utilization of Pt CE. Some studies suggested that Pt is unsuitable when used with polysulphide electrolytes (Chen et al., 2014; Tachan et al., 2011; Yeh et al., 2011). Pt is not catalytic to the polysulphide–based electrolyte and this will affect performance of the QDSSCs (Radich et al., 2011). Utilization of Pt CE with polysulphide–based electrolyte will lead to "Pt poisoning effect" where S compounds in the electrolyte adsorb to the Pt surface. This will eventually suppress electron transfer to the redox mediator in the electrolyte (Hodes et al., 1977; Hodes et al., 1980; Lee et al., 2009). Another problem with utilization of Pt in QDSSCs is Pt would corrode with presence of sulphur in the polysulphide electrolyte system (Seo et al., 2011).

To find an alternative for Pt CE in studies of QDSSCs, researchers have come out with various materials such as noble metals, conducting polymers, carbon–based materials and metal chalcogenides (Seo et al., 2011). Gold (Au) a noble metal, has a great potential to replace Pt and may be a good CE material. Just like Pt, Au is catalytic towards reduction of redox mediator in iodide–based electrolyte. Au has been used as CE in many sensitized solar cell studies such as DSSCs, QDSSCs and perovskite solar cells. Seo et al. (2011) have replaced Pt CE with Au CE in QDSSC. According to this study, QDSSC fabricated with Au CE showed a 42% improvement in *PCE* compared to the QDSSC fabricated with Pt CE.

Another interesting material for use as CE is metal sulphides. Metal sulphides have proven to be a good material (Seo et al., 2011). Many metal sulphides have been studied in QDSSCs with polysulphide electrolyte system and they showed a positive impact to the performance of the device for example copper monosulphide (CuS) (Lin et al., 2013), copper(I) sulphide (Cu_2S) (Radich et al., 2011), cobalt sulphide (CoS) (Faber et al., 2013), and nickel sulphide (NiS) (Hodes et al., 1977). Compared to Pt CE, metal sulphide CE is much more catalytic toward reduction of redox mediator in polysulphide electrolyte and provide ease charge transfer between CE and electrolyte which can result in a generation of large current density. Among all metal sulphides available, lead sulphide (PbS) could provide an auxiliary tandem effect (Figure 2.6) that has been reported by Lin et al. (2013).

With presence of auxiliary tandem effect in the QDSSC, CE could functionalize as photocathode that provides additional electron source (improve J_{sc}) and additional V_{oc} as described in Figure 2.6. PbS is p-type semiconductor with small band gap which possessed wide absorption range to the near infrared region. This will make the remnant light that could not be absorbed by the photoanode to be absorbed by the PbS CE which will generate additional electrons to the QDSSC system and eventual improve the cell's J_{sc}. According to the auxiliary tandem effect, the V_{oc} of the cell is the energy difference between the quasi-Fermi levels ($_{q}E_{f}$) of the photoanode (n–type) and cathode (p–type) (Shalom et al., 2011) i.e. $V_{oc} = V_{oc1} + V_{oc2}$. The quasi-Fermi level of an electrode, either the anode or the cathode, depends on the equilibration between the electrode to the electrolyte. Illuminating the photoactive electrode shifts the quasi-Fermi level toward the vacuum Fermi level.

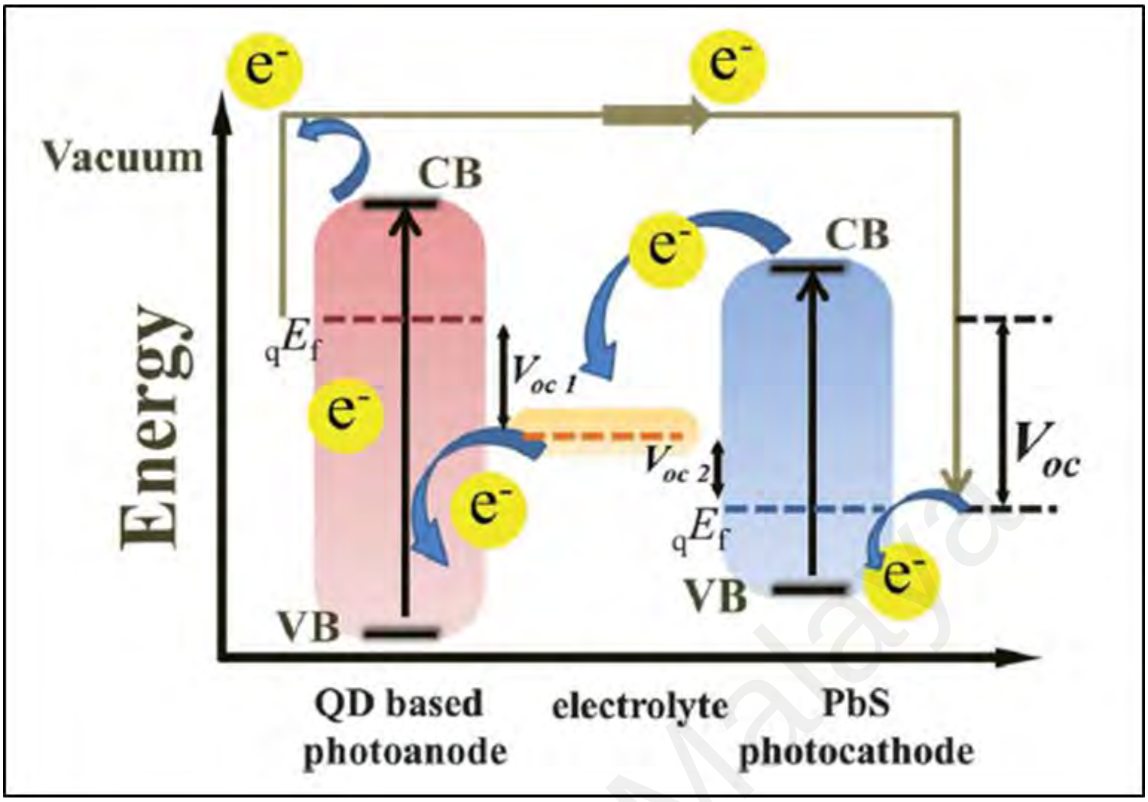

Figure 2.6: The schematic diagram of auxiliary tandem effect with the movement of the electrons, the energy band gap and fermi level of the QDSSC with PbS CE (Lin et al., 2013).

2.4. List of the CdS QDSSC Studies Reported in the Literature

Table 2.1 summarizes some of the QDSSCs work obtained from literature using CdS QD as sensitizer. From Table 2.1, it can be seen that CdS based QDSSCs fabricated with iodide–based electrolyte exhibited the lowest *PCE*. This is because the iodide containing electrolyte will corrode the CdS QD. The material used at the CE also affects the performance of the CdS based QDSSCs. From Table 2.1, QDSSCs fabricated with Pt cathode exhibited *PCE* below than 2% while majority of QDSSCs fabricated with metal sulphide CE exhibited more than 3% *PCE*.

Table 2.1: QDSSCs work obtained from literature with CdS QD as sensitizer.

Electrolyte	**Photoanode arrangement**	**CE**	**Deposition method**	***PCE* (%)**	**reference**
ILE	TiO_2/CdS	Pt	ML	0.30	(Jen et al., 2008)
ILE	ZnO/CdS	Pt	CBD	0.54	(Lee et al., 2009)
IGPE	TiO_2/RGO/CdS	Pt	SILAR	0.37	(Badawi, 2015)
PLE	TiO_2/CdS	Pt	CBD	1.15	(Lee et al., 2008)
PLE	TiO_2/CdS	Pt	CBD	1.28	(Sudhagar et al., 2009)
PLE	TiO_2/CdS	Au	SILAR	1.62	(Zhu et al., 2010)
PLE	TiO_2/CdS	Au	SILAR	2.01	(Chou et al., 2010)
PLE	TiO_2/CdS	Au	CBD	1.03	(Zhu et al., 2011)
PLE	TiO_2/CdS/ZnS/P3HT	Cu_2S	SILAR	3.07	(Pasarán et al., 2016)
PLE	TiO_2-nanorod/CdS/ZnS	CuS	SILAR	3.22	(Lan et al., 2016)
PGPE	TiO_2/CdS/ZnS	Pt	SILAR	1.72	(Jung et al., 2012)
PGPE	TiO_2/CdS/ZnS/SiO_2	Pt	SILAR	1.42	(Mingsukang et al., 2016)
PGPE	TiO_2/CdS/ZnS/SiO_2	PbS	SILAR	2.90	(Mingsukang et al., 2017)

ILE= iodide liquid electrolyte; IGPE= iodide gel polymer electrolyte; PLE= polysulphide liquid electrolyte; PGPE= polysulphide gel polymer electrolyte.

2.5 Summary

In this chapter (literature review), overall topics on QDSSCs have been discussed. These include working mechanism and its components i.e. photoanode, electrolyte and CE. The discussion in this chapter also included the progress of the QDSSCs. Although the overview is inexhaustive, it is hoped that this chapter will provide understanding on QDSSCs and also some insight on the development of this device.

CHAPTER 3: EXPERIMENTAL METHODS

3.1 Introduction

In this chapter, the preparation and characterization of all components (viz., electrolyte, photoanode and CE) and fabrication of the QDSSC have been described. The work started with the preparation, characterization and optimization of the methylcellulose–polysulphide gel polymer electrolyte (MC–PGPE), which is the first objective in this work. The work continues with the second objective i.e. optimizing the photoanode sensitized with CdS QDs. Successive ionic layer absorption and reaction (SILAR) method has been used for depositing CdS QDs to the surface of the TiO_2–photoanode. 10 different TiO_2/CdS photoanodes with different number of SILAR cycles i.e. 1–10 SILAR cycles have been prepared to investigate which number of SILAR cycles will give the best performance to the QDSSC (fabricate with Pt CE). The optimized TiO_2/CdS photoanode then will be included with the passivation layer i.e. ZnS and SiO_2 to further improve the performance of the QDSSC. The last part of this work is the investigation of the best CE material which is the third objective. Au and PbS have been chosen for the subject study because of Au is noble metal and possesses same properties with Pt while PbS is chosen because it's can provide tandem auxiliary effect that will improve the current and voltage of the QDSSCs.

3.2 Preparation of MC–PGPEs

MC–PGPEs prepared in this work consist of methylcellulose (host polymer), distilled water (solvent), Na_2S and S (polysulphide contributor). MC–PGPEs have been prepared in small transparent sample bottles. The first step of the preparation of the MC–PGPEs is by forming the gel by mixing the distilled water with methylcellulose (MC) under constant stirring by using small magnetic bar and the magnetic stirrer. The amount of MC and distilled water for every samples have been fixed at 0.1 g and 0.25 g respectively. Na_2S and S were introduced when gels are formed. The amount of Na_2S and S were varied in order to optimize the ionic conductivity of the MC–PGPEs. The composition of the MC–PGPE samples are shown in Table 3.1 (in grams) and Table 3.2 (in weight percentage). The amount of sulphur used was fixed at 2.8 *wt.%* of the amount of Na_2S. The amount of Na_2S used was not more than 7.78 *wt.%* since above that the Na_2S salt can no longer dissolve.

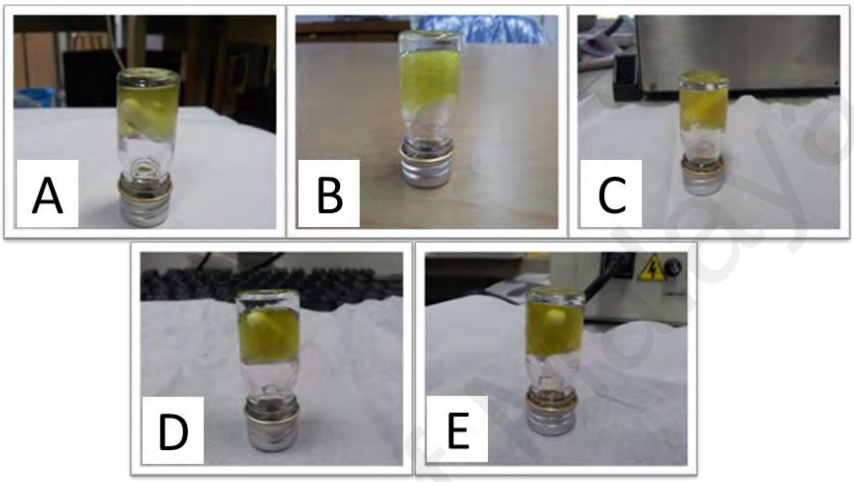

Figure 3.1: Images of MC–PGPEs. (Sample A, B, C, D and E).

Table 3.1: Composition of MC–PGPEs in gram (g).

Samples	Methylcellulose (g)	Distilled water (g)	Na_2S (g)	sulphur (g)
A	0.1	2.5	0.10	0.0028
B	0.1	2.5	0.15	0.0041
C	0.1	2.5	0.20	0.0056
D	0.1	2.5	0.21	0.0058
E	0.1	2.5	0.22	0.0062

Table 3.2: Composition of MC–PGPEs in weight percentage (wt. %).

Samples	Methylcellulose (*wt.%*)	Distilled water (*wt.%*)	Na_2S (*wt.%*)	sulphur (*wt.%*)
A	3.70	92.50	3.70	0.10
B	3.63	90.77	5.45	0.15
C	3.56	89.11	7.13	0.20
D	3.55	88.78	7.46	0.21
E	3.54	88.46	7.78	0.22

3.3 Characterization of MC–PGPEs

3.3.1 Electrochemical Impedance Spectroscopy

Electrochemical impedance spectroscopy (EIS) is a very useful technique to analyse the impedance and electrical properties of the electrolyte such as ionic conductivity (σ), ionic number of density (n), ionic mobility (μ) and ionic diffusion coefficient (D). In this work, impedance of the GPE samples were measured using HIOKI 3532–50 LCR HiTESTER instrument from 50 Hz to 1 MHz with applied voltage of 10 mV. During the EIS measurement, GPE samples was placed in the coin cell so that the GPE sample possesses cylindrical shape (0.3 cm length (l) and 1.61 cm^2 surface area (A)) and sandwiched in between stainless-steel electrodes. The ionic conductivity of the GPE samples were calculated by using the Equation (3.1). R_b is bulk resistance which can be obtained from the Nyquist plot shown in Figure 3.2(a) and (c).

$$\sigma = \frac{l}{A \times R_b} \tag{3.1}$$

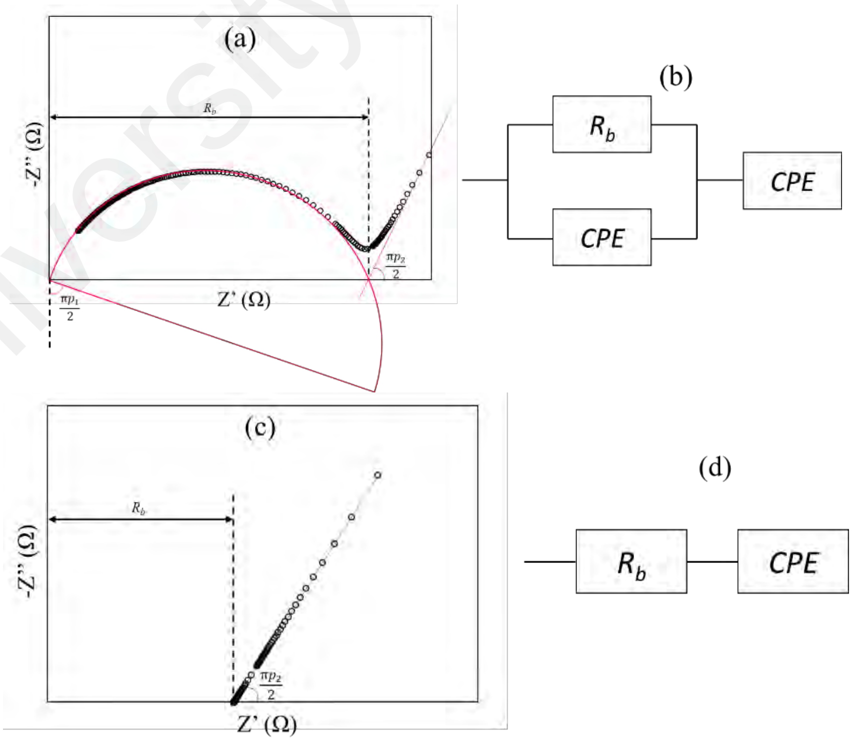

Figure 3.2: (a) and (c) show examples of Nyquist plots that could be obtained from EIS measurement. (b) and (d) are the corresponding equivalent circuit to the Nyquist plot in (a) and (c) respectively.

The impedance obtained from the EIS measurement is in complex form which consist of real part (*Z'*) and imaginary part (*Z''*). There are two possibilities of Nyquist plot shape obtained from the GPEs EIS measurement which are tilted semicircle with tilted spike and tilted spike only as shown in Figure 3.2(a) and (c) respectively. Figure 3.2(b) and (d) represent the equivalent circuit for the Nyquist plot in Figure 3.2(a) and (c) respectively.

The equivalent circuit of Nyquist in Figure 3.2(b) can be expressed using Equation (3.2) (Teo et al., 2012):

$$Z = \left[\frac{R_b + R_b^2 k_1^{-1} \omega^{p_1} cos\left(\frac{\pi p_1}{2}\right)}{1 + 2R_b k_1^{-1} \omega^{p_1} \cos\left(\frac{\pi p_1}{2}\right) + R_b^2 k_1^{-2} \omega^{2p_1}} + \frac{\cos\frac{\pi p_2}{2}}{k_2^{-1} \omega^{p_2}}\right] + \left[\frac{R_b^2 k_1^{-1} \omega^{p_1} sin\left(\frac{\pi p_1}{2}\right)}{1 + 2R_b k_1^{-1} \omega^{p_1} \cos\left(\frac{\pi p_1}{2}\right) + R_b^2 k_1^{-2} \omega^{2p_1}} + \frac{sin\left(\frac{\pi p_2}{2}\right)}{k_2^{-1} \omega^{p_2}}\right] i \tag{3.2}$$

Where, *R* correspond to the bulk resistance (*R_b*) of the GPE, k_1^{-1} is correspond to bulk GPE capacitance, k_2^{-1} correspond to double layer capacitance, *ω* is angular frequency, p_1 is the angle between y–axis (Z'') with the diameter of the semicircle, and p_2 is the angle between the tilted spike with the x–axis (Z').

In this work, the Nyquist plot obtained for MC–PGPE samples only possessed the tilted spike as shown in Figure 3.2(b), the complex impedances obtained from tilted spike Nyquist plot can be express and fit through the equivalent circuit (Figure 3.2 (b)) by using Equation (3.3):

$$Z = \left[R_b + \frac{\cos\frac{\pi p_2}{2}}{k^{-1} \omega^{p_2}}\right] + \left[R_b + \frac{sin\left(\frac{\pi p_2}{2}\right)}{k^{-1} \omega^{p_2}}\right] i \tag{3.3}$$

According to Bandara et al. (2011) and Tiong et al. (2016), the ionic transport properties of the MC–PGPE samples such as *D*, *μ* and *n* can be calculated by using equations:

$$D = \frac{d^2}{\tau\delta^2} \tag{3.4}$$

$$\mu = \frac{eD}{k_b T} \tag{3.5}$$

$$n = \frac{\sigma}{e\mu} \tag{3.6}$$

where, d is ½ the sample thickness, τ is $1/\omega$ ($\omega = 2\pi f$, f is a frequency of the applied voltage) (Bandara et al., 2011; Tiong et al., 2016), $\delta = d/\lambda$ (λ is the electrical double layer which equal to $\lambda = \varepsilon'\varepsilon_o A/k^{-1}$), k_b is Boltzmann's constant, k^{-1} is correspond to the double layer capacitance (obtain from Nyquist plot fitting), ε_o is the vacuum permittivity, ε' is the dielectric constant of the MC–PGPE sample which can be calculated by using Equation (3.7):

$$\varepsilon' = \frac{Z''}{\omega\left(\frac{\varepsilon_o A}{t}\right)[(Z')^2+(Z'')^2]} \tag{3.7}$$

Another important information that can be obtained in order to understand the electrical behaviour of the GPE is activation energy (E_a). In this experiment, E_a value is considered as a minimum energy required for the ionic conduction in the GPE. In this work, the relationship between σ–T of the GPEs follow the Arrhenius equation:

$$\sigma = \sigma_o \exp(\frac{E_a}{kT}) \tag{3.8}$$

Where σ_o is a material constant, T is absolute temperature, N is Avogadro's constant and k is Boltzman's constant. Equation (3.9) can be modified into straight line equation and the E_a can be calculated from the gradient of graph of log (σ) versus 1000/T. Below is the modified Arrhenius equation straight line equation for the E_a calculation:

$$\log(\sigma) = (0.4343)\frac{Ea}{kT} + \log(\sigma_o) \tag{3.9}$$

3.3.2 Tafel Polarization Measurement by Linear Sweep Voltammetry (LSV)

Tafel polarization is a well-known test to measure the electrochemical process that occurred at the interface of the CE and electrolyte in sensitized solar cells (Hwang et al., 2015). In this part, the symmetric dummy cell of CE used for the measurement will be made up of two Pt CEs sandwiching the MC–PGPE samples spaced by Scotch tape with thickness of 53 μm. Figure 3.3 shows the schematic diagram of the symmetric dummy cell. By using LSV, the corresponding output current density of the symmetric cell is measured under a varying bias voltage. The applied voltage was swept from -0.6 to 0.6 V at the slow rate (10 mV/s) and the linear sweep voltammogram schematic diagram obtained is as shown in Figure 3.4.

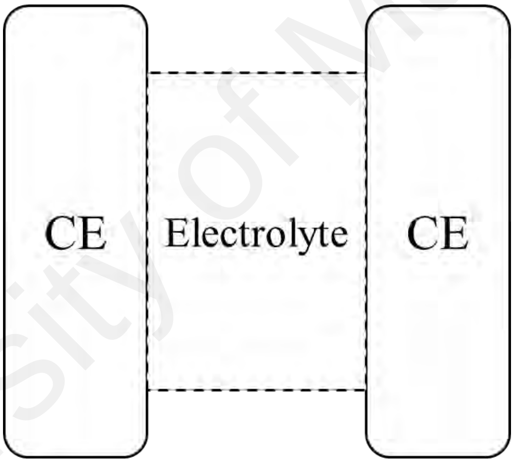

Figure 3.3: Schematic diagram of symmetric dummy cell.

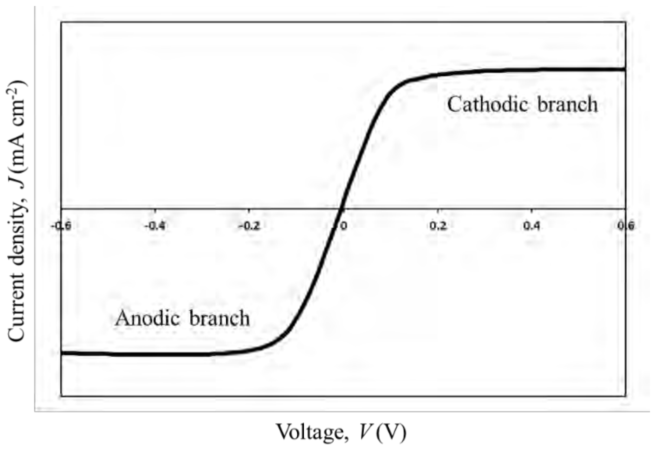

Figure 3.4: An example of a linear sweep voltammogram of a symmetric dummy cell.

The Tafel curve (Figure 3.5) was obtained from the linear sweep voltammogram by plotting the current density as a function of the bias voltage. There are three regions in the Tafel curve which are polarization zone, Tafel zone and diffusion zone. Polarization zone is located at a very low potential, the Tafel zone at a moderate potential, has a high Tafel gradient and the diffusion zone is located in the high potential region. Diffusion and Tafel zones are related to the charge transfer process in between CE to the electrolyte (S_x^{2-} ions). From diffusion zone, limiting current density (J_{lim}) can be obtained and exchange current density (J_o) can be obtained from the Tafel zone. J_{lim} is the maximum current density that can be used to get the desired electrode reaction without interference from polarization and J_o is the current in the absence of net electrolysis and at zero potential. Also, J_o can be considered as background current to which the net current observed at various overpotentials is normalized.

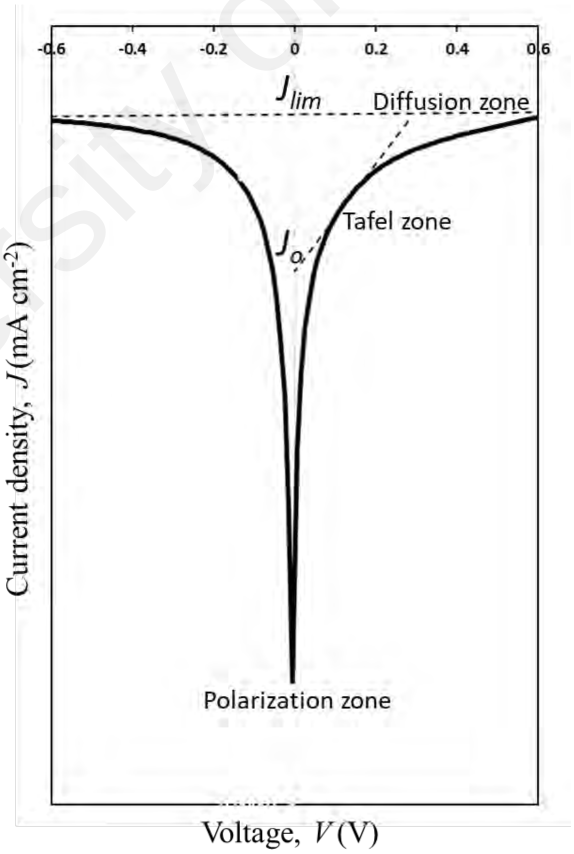

Figure 3.5: The example of Tafel polarization curve for J_o and J_{lim} measurement.

From Tafel polarization curve, J_{lim} obtained from current density at diffusion zone while J_o obtained by extrapolating the curve in its Tafel zone to zero potential. In this research, the J_{lim} was considered for S_x^{2-} ions as sulphide concentration was greater than the concentration of S in the GPE samples (Papageorgiou et al., 1996; Gopi et al., 2018; Vijayakumar et al., 2018) . From J_{lim} and J_o in the Tafel curve, the diffusion of the S_x^{2-}ions ($D_{S_x^{2-}}$) and charge transfer resistance at interface of CE/electrolyte of symmetrical dummy cell (R_{dc}) can be calculated using the equations below:

$$D_{S_x^{2-}} = \frac{d}{2nFC} J_{lim} \tag{3.10}$$

$$R_{dc} = \frac{RT}{nF} J_o \tag{3.11}$$

where *d* is the electrolyte thickness, *n* is the number of electrons involved for the reduction of the S_x^{2-}ion to S^{2-}ion, *F* is Faraday's constant, *C* is the initial S_x^{2-} ions concentration, *R* is gas constant and *T* is the temperature in kelvin.

3.3.3 Fourier Transform Infrared Spectroscopy

Fourier transform infrared (FTIR) spectroscopy was used to determine the composition interaction in the MC–PGPE sample. The instrument used to collect the FTIR spectrum for GPE samples in this work is Thermo Scientific model Nicolet iS10 spectrometer. The FTIR spectrum has been collected by using attenuated total reflectance (ATR) method in the wavenumber range of 500–4000 cm^{-1}. The advantages of ATR method in collecting FTIR spectrum is it requires minimal sample preparation, no additional condition for the measurement and easy to clean up the experimental waste by simply wipe off the sample.

When GPE sample radiated with infrared radiation, functional groups inside the GPE will absorb the radiation if the frequency of the radiation is same with the functional group vibration. Different functional groups have different characteristic frequency for absorption. Hence, functional groups in the GPE sample can be determine from FTIR spectrum. However, compound with ionic bond which absorb radiation far from the IR range is invisible in the FTIR spectra due to they are not capable in absorbing IR radiation. Hence, the FTIR spectra obtained from MC–PGPEs in this work are mainly from the MC host polymer and distilled water.

3.4 Preparation of Photoanode

3.4.1 Preparation of TiO_2 Electrode

TiO_2 photoanode consist of fluorine tine oxide (FTO) glass, TiO_2 compact layer and TiO_2 mesoporous layer. The resistance of FTO glass used in this work was 14 Ω cm^2 which has been bought from local company. The formation of the TiO_2 photoanode can be seen in Figure 3.6 in which the compact and the mesoporous layers were deposited on the FTO glass. The TiO_2 mesoporous layer is the place where the QDs sensitizer will be deposited. The porosity of this layer is important for QDs deposition and contact area between photoanode and electrolyte. The purpose of compact layer is to prevent electrolyte from making contact with the FTO substrate in order to avoid recombination of electrons from FTO substrate to the electrolyte.

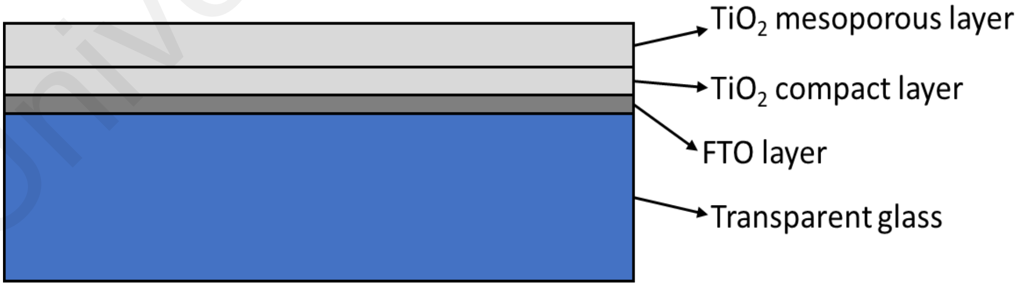

Figure 3.6: An illustration of TiO_2 electrode which consist of FTO conducting glass and two layers of TiO_2 i.e. compact and mesoporous layers.

TiO_2 which has particles size ~14 nm (P90) was used in the preparation of the TiO_2 compact layer. P90 has been purchased from Evonik Degussa GmbH. TiO_2 compact layer has been deposited by spin–coating P90 TiO_2–HNO_3 paste on the FTO glass at 2350 rpm for 50 seconds. Then followed by drying and sintering process. Sintering process has been done at 450 °C for 30 minutes under the normal atmosphere condition.

In the preparation of the mesoporous layer, P25 TiO_2 has been used which has particle size of 21 nm. P25 TiO_2 also has been purchased from Evonik Degussa GmbH. TiO_2 mesoporous layer was deposited on top of the compact layer by spreading the P25 TiO_2 paste containing HNO_3, surfactant and carbowax by using Doctor Blade technique. Then followed by drying and sintering process. Sintering process has been done at 450 °C for 30 minutes under the normal atmosphere condition.

3.4.2 Deposition of CdS QDs Sensitizer and Passivation Layers

Figure 3.7: Image of 10 different photoanodes prepared with 1–10 SILAR cycles.

An economic and facile method i.e. successive ionic layer absorption and reaction (SILAR) has been used for depositing CdS QDs to the surface of TiO_2 photoanode. Figure 3.7 shows the 1–10 SILAR cycle photoanodes prepared in this work. The prepared TiO_2 electrode was dipped in 0.1 M cadmium nitrate [$Cd(NO_3)_2$] solution for one minute and followed by process of rinsing and drying. Then the TiO_2 electrode was dipped again in the 0.1 M Na_2S solution for one minute followed by process of rinsing and drying. These two dipping in different solutions were considered as one SILAR cycle. To optimize the photoanode, 10 photoanodes with different number of SILAR cycles (1–10 SILAR cycles) have been prepared.

The optimized TiO_2/CdS will be employed with two type of passivation layers which are zinc sulphide (ZnS) and silicon dioxide (SiO_2). SILAR method has been used for deposition of ZnS passivation layer by using 0.1 M zinc acetate ($ZnC_4H_6O_4$) and 0.1 M Na_2S solution. Two SILAR cycles was used for depositing ZnS passivation layer. The deposition of SiO_2 passivation layer was done by soaking the photoanode in the tetraethyl orthosilicate solution for 24 h followed by rinsing and drying process.

3.5 Characterizations of Photoanode

3.5.1 Field Effect Scanning Electron Microscopy

Field effect scanning electron microscopy (FESEM) is a powerful microscope to study the morphology of the photoanodes on a very fine scale (resolution up to 1 nm). FESEM producing an image by bombarding the sample target with high energy electrons. As the target sample interact with the high energy electrons, the target will emit signals that will be collected by the instrument to generate the image. In this work, the morphology of the photoanode surface will be studied by using FESEM. In addition, FESEM will help with determination of the material layer thickness deposited at the photoanode. FESEM instrument used in this work is Hitachi SU8220.

3.5.2 Energy Dispersive X–ray

Usually FESEM will be equipped with energy dispersive X–ray (EDX) spectroscopy that is useful for the elemental analysis/compositional studies of the samples. In EDX analysis, the sample will be bombarded with high energy electrons and the sample will interact by emitting radiation (X–ray). The emitted X–ray radiation will be collected to generate the EDX spectrum. Different elements will emit different unique amount of X–ray energy, hence, the elemental analysis can be done by referring to the EDX spectrum.

3.5.3 UV–Vis Spectroscopy

Ultraviolet–visible (UV–Vis) spectroscopy is an instrument that measuring absorption of the target sample at the wavelength range of ultraviolet to visible light. During UV–Vis measurement, the sample will be illuminated under light at the range of UV to visible light and the instrument will measure the attenuation of the light pass through at every wavelength. In this work, UV–Vis absorption of the photoanodes have been done by using Shimadzu PC3101 UV–Vis NIR spectroscopy at the range of 300–800 nm. Energy band gap (E_g) of the photoanode samples have been estimated based on Beer–Lamber's law (Ghobadi, 2013):

$$\alpha hv = B(hv - E_g) \tag{3.12}$$

Where, α is the absorption, hv is the incident photon energy and B is a constant. The Equation (3.12) has been rearranged to form a straight-line equation [shown in Equation (3.13)] and the E_g can be estimated by plotting the graph of of $(\alpha hv)^2$ versus hv as shown in Figure 3.8.

$$(\alpha hv)^2 = B_1(hv - E_g) + B_2 \tag{3.13}$$

Where B_1 and B_2 are constants.

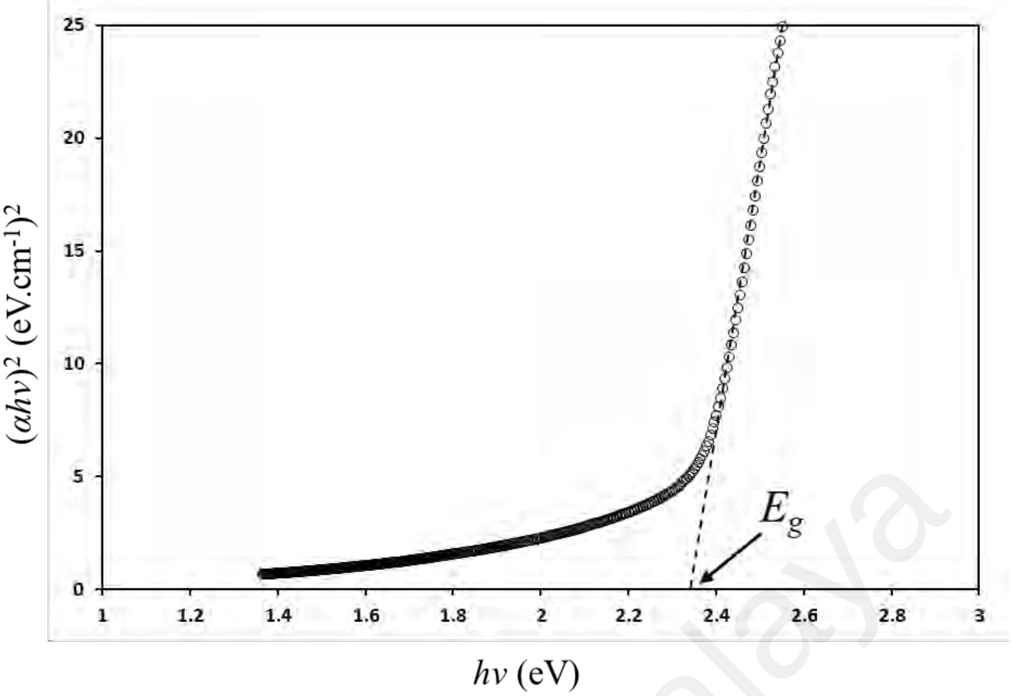

Figure 3.8: The example of graph of $(\alpha hv)^2$ versus hv or also known as Tauc's plot for E_g determination.

3.6 Preparation of Counter Electrodes (CEs)

3.6.1 Platinum CE

Platinum (Pt) CE has been prepared by using spin coating technique. A layer of platinum has been coated on top of FTO glass by spin coating plastisol solution on top of FTO glass and followed by sintering process at 450 °C for 30 minutes under the normal atmosphere condition.

3.6.2 Gold CE

Gold (Au) CE was prepared by using sputtering technique. Au particles have been deposited on the FTO glass by using sputtering instrument followed by sintering process at 450 °C for 30 minutes under normal atmosphere condition.

3.6.3 Lead Sulphide CE

Lead sulphide (PbS) CE has been prepared by using procedure that was introduced by Tachan et al. (2011). In this procedure, PbS has been formed on the surface of Pb foil. Pb foil was cleaned by using sand paper to remove the oxide layer on the foil surface followed by washing process by using distilled water. After the cleaning process, the foil was then soaked in a solution of sulfuric acid (H_2SO_4) and distilled water in a 1:1 volume ratio for 24 h. After 24 h soaked in the acid solution, the foil then was soaked again in the polysulphide solution composed of 1 M Na_2S, 0.1 M sulphur and 0.1 M NaOH for 24 h. PbS was formed on the surface of the Pb foil during soaking process in the polysulphide solution.

3.7 Characterization of Counter electrode

3.7.1 Field Effect Scanning Electron Microscopy

FESEM was used to study the morphology of the Pt, Au and PbS CE surfaces in the very fine scale. The FESEM instrument used in this part is same with the previous section (characterization of photoanode) which is Hitachi branded model SU8220. The morphology and topography of CE surface is important to understand the surface contact between CE and the electrolyte.

3.7.2 Electrochemical Impedance Spectroscopy Measurement of Symmetrical Dummy Cells

EIS also can be used to study the interfacial properties in between any kind of material for example in this case in between electrolyte and CE. In this part of experiment, the impedance of Pt, Au and PbS symmetrical dummy cells (Figure 3.3) have been collected by using EIS measurement. Symmetrical dummy cell is a cell fabricated with both electrodes being Pt or Au or PbS sandwiching with electrolyte in the form of thin film (MC–PGPE) separated by Scotch tape of 53 µm. The impedances of the CE symmetrical dummy cells can be observed in the range of high frequencies due to the rate of charge transfer at the interface of CE/electrolyte is fast (Kavan et al., 2014). Hence, the frequency region used for the impedance measurement of symmetrical dummy cells is from 23 kHz to 1 Hz.

According to Hwang et al. (2015) symmetrical dummy cell EIS measurement will give Nyquist plot shape and respective equivalent circuit shown in Figure 3.9. In Figure 3.9, the first semicircle is responsible for the charge transfer at interface of CE/electrolyte and the second semicircle is responsible for the electrolyte diffusion. However, electrolyte diffusion is not related to the charge transfer in between CE/electrolyte. In addition, the semicircle responsible for the electrolyte diffusion does not appeared in Nyquist plot obtained from this work for example as shown in Figure 3.10. Based on the equivalent circuit in Figure 3.10, the Nyquist plots obtained have been fitted by using Equation (3.14):

$$Z_{dc} = R_s + \frac{2R_{dc}}{1+[(j\omega)^{n_{dc}}(2R_{dc})(Q_{dc})]} \quad (3.14)$$

Where, R_s is a series resistance, R_{dc} and Q_{dc} are the charge transfer resistance and CPE at the interface of CE/electrolyte, n_{dc} is the CPE index and ω is angular frequency $(2\pi f)$.

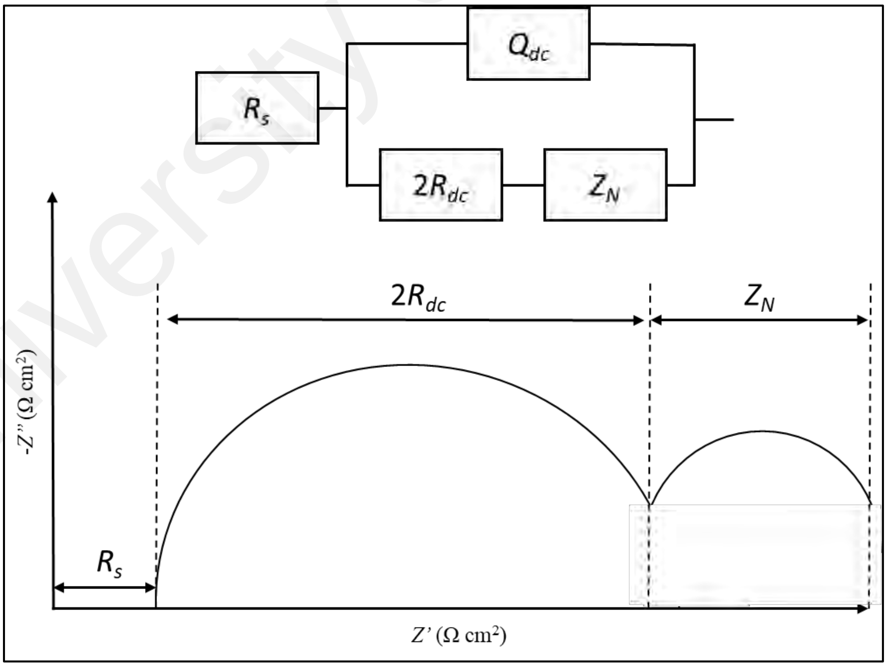

Figure 3.9: The usual Nyquist plot of the symmetrical dummy cell and the inset is the equivalent circuit corresponding to the Nyquist plot. Z_N is electrolyte diffusion (Hwang et al., 2015).

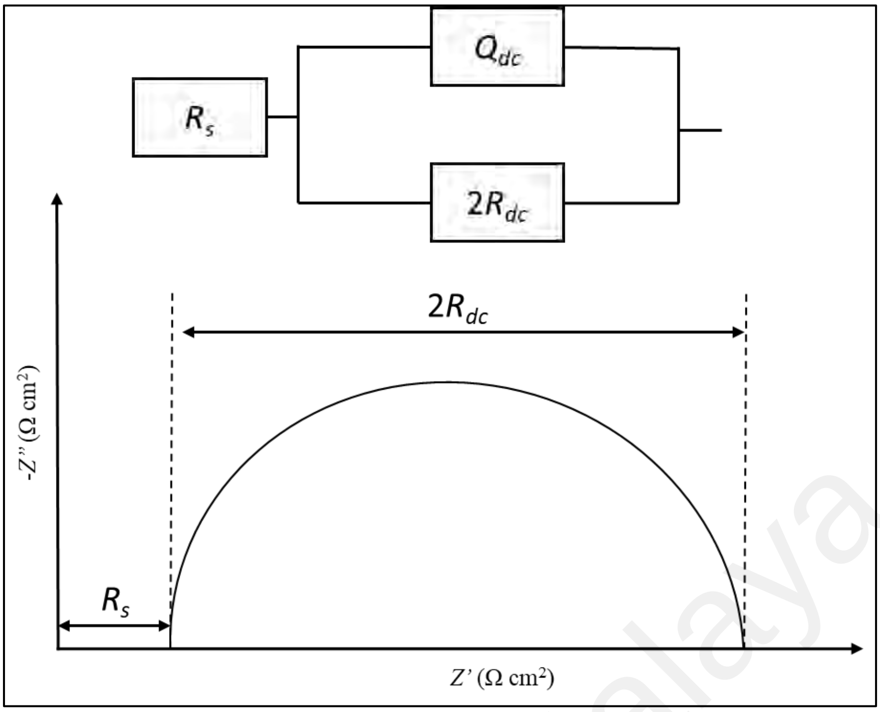

Figure 3.10: The example of Nyquist plot obtained from this work which consist of one semicircle that refer to the charge transfer process at the interface of the CE/electrolyte. Inset of this figure is the equivalent circuit correspond to the plot (Huang et al., 2012).

3.7.3 Tafel Polarization Measurement by Linear Sweep Voltammetry (LSV)

This characterization has been discussed in the earlier section under characterization of MC–PGPE (3.3.2). This method is a technique to characterize the electrocatalytic activity of the target CE toward the MC–PGPE. A symmetrical dummy cell was used for the measurement of current densities, which was constituted of two Pt or Au or PbS CEs separated by Scotch tape of 53 µm. In this experiment the applied voltage was swept from - 0.6 V to 0.6 V at the slow rate of 10 mV/s. Four important parameters can be obtained from this measurement i.e. J_{lim} and J_o which are related to the diffusion of the polysulphide ions ($D_{S_x^{2-}}$) and the charge transfer resistance at CE/electrolyte interface (R_{dc}) in the symmetric dummy cell respectively.

3.8 Fabrication of QDSSCs

One of the interesting properties of QDSSCs is the fabrication process is easy and can be done under normal atmospheric condition. The fabrication process was simply performed by sandwiching optimized MC–PGPE between photoanode and CE as shown in Figure 3.11. Fabrication of QDSSCs have been made in studies of photoanodes (second objective) and CE (third objective). Characterization of the QDSSCs for the studies of photoanodes have been made with optimized MC–PGPE (obtained from the first objective experiments) and Pt CE. Characterization of QDSSCs for the studies of CEs have been made with optimized MC–PGPE and the best photoanode.

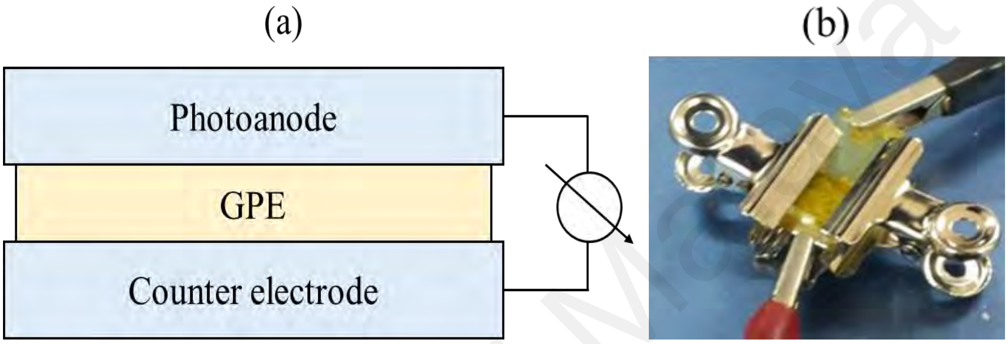

Figure 3.11: (a) shows the schematic diagram of the QDSSC and (b) is the real picture of QDSSC fabricated in this work.

3.9 Characterization of QDSSC

3.9.1 Photocurrent Density–Voltage (*J-V*) Characteristics

During *J–V* characterization, the QDSSCs were illuminated under 100 mW cm^{-2} intensity light source by using Xenon bulb (Orial LCS 100) and the cell was connected to the Autolab potentiostat–galvanostat to measure the *J–V* characteristic. Figure 3.12 shows the example of *J–V* characteristic measured from the photovoltaic device and this plot often called as *J–V* curve. From *J–V* characteristic, power conversion efficiency (*PCE*) of the QDSSCs fabricated can be calculated by using Equation (3.15):

$$PCE(\%) = \frac{J_{sc} \times V_{oc} \times FF}{P_{in}} \times 100 \tag{3.15}$$

where,

$$FF = \frac{J_{max} \times V_{max}}{J_{sc} \times V_{oc}} = \frac{\text{Area B}}{\text{Area A}} \tag{3.16}$$

J_{sc} is short circuit a current density of the cell, V_{oc} is an open circuit voltage of the cell, FF is a fill factor, J_{max} is current density at maximum power output and V_{max} is voltage at maximum power output.

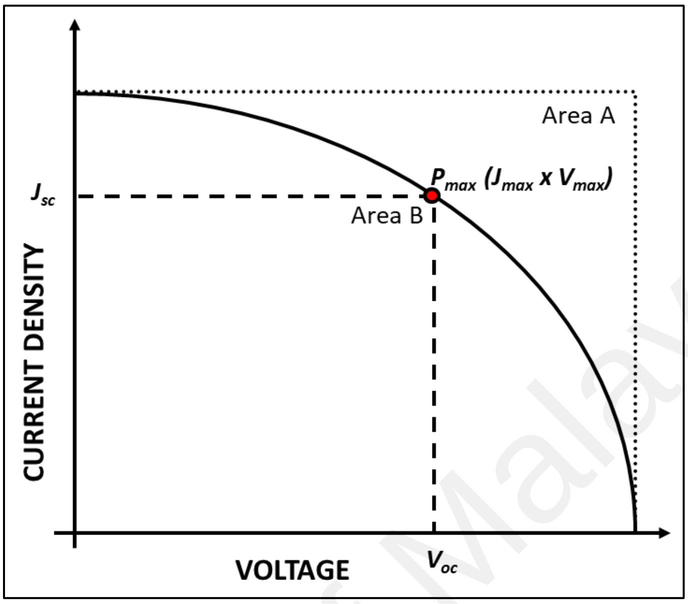

Figure 3.12: Example of *J–V* curve measured from photovoltaic device.

3.9.2 Impedance Study of the QDSSC

The impedance of the QDSSCs were measured using EIS technique. This technique can determine the interfacial behaviour in between electrodes and electrolyte (Bisquert et al., 2000; Fabregat-Santiago et al., 2007). From EIS analysis of the QDSSCs, the resistance and capacitance at the electrodes/electrolyte interface will provide some information that could relate to the performance of the devices. In this work, the EIS analysis of the QDSSCs have been done by using Autolab potentiostat/galvanostat under 100 mW cm^{-2} intensity light source by using Xenon bulb (Orial LCS 100). In addition, the EIS measurement were performed at open circuit voltage of the respective QDSSC in order to generate the maximum impedance. In general, Nyquist plot generate by QDSSC compose of three semicircles: first semicircle (at high frequencies) is correspond to the CE/electrolyte interfacial, second semicircle (at medium frequencies) is correspond to the photoanode/electrolyte interfacial and the last semicircle (at low frequencies) which not appear in this work (Figure 3.13) is correspond to the electrolyte diffusion (Ng et al., 2015).

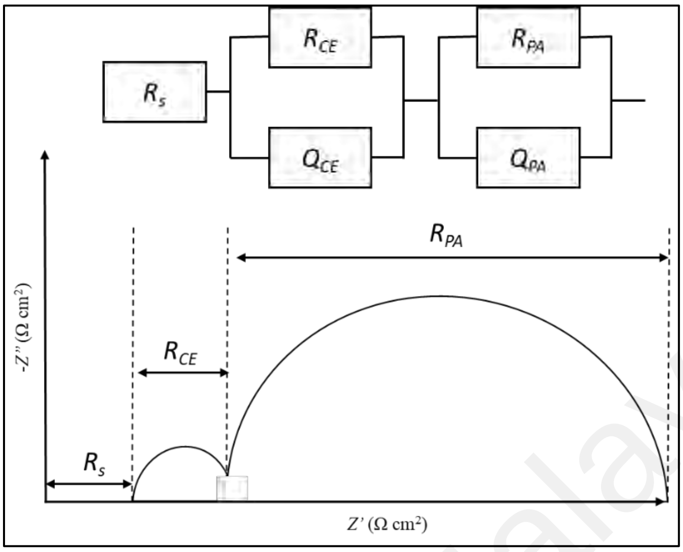

Figure 3.13: The schematic Nyquist plot obtained from this work which consist of two semicircles correspond to the CE/electrolyte and photoanode/electrolyte interfacial.

Based on the equivalent circuit in Figure 3.13, the Nyquist plots obtained from the EIS measurement can be fitted by using Equation (3.17) (Sarker et al., 2014):

$$Z_{QDSSC} = R_s + \frac{R_{CE}}{1+(j\omega)^{n_{CE}} R_{CE} Q_{CE}} + \frac{R_{PA}}{1+(j\omega)^{n_{PA}} R_{PA} Q_{PA}} \tag{3.17}$$

where, R_{CE} and Q_{CE} are resistance and constant phase element at CE/electrolyte interface respectively. R_{PA} and Q_{PA} are the resistance and constant phase element at photoanode/electrolyte interface respectively. n_{CE} and n_{PA} are the CPE index at the interfaces of CE/electrolyte and photoanode/electrolyte respectively. The interfacial capacitance at interface of CE/electrolyte (C_{CE}) and photoanode/electrolyte (C_{PA}) can be calculated using Equation (3.18) and Equation (3.19) respectively:

$$C_{CE} = \frac{(Q_{CE} \times R_{CE})^{\frac{1}{n_{CE}}}}{R_{CE}} \tag{3.18}$$

$$C_{CE} = \frac{(Q_{CE} \times R_{CE})^{\frac{1}{n_{CE}}}}{R_{CE}} \tag{3.19}$$

An electron lifetime in the QDSSC can be estimated using Bode phase plot that can be established from the EIS results. Bode phase plot is a plot of phase versus frequency as shown in Figure 3.14. From the Bode phase plot, the electron lifetime, τ can be calculated by using Equation (3.18):

$$\tau = \frac{1}{2\pi f_{peak}} \tag{3.18}$$

Here f_{peak} is the frequency where the characteristic peak can be obtained from the Bode plot of the EIS (Kern et al., 2002). The τ value will indicate that the electron recombination process occurs in the QDSSC i.e. highest τ resulted from the highest electron recombination process rate and vice versa (Bisquert et al., 2009).

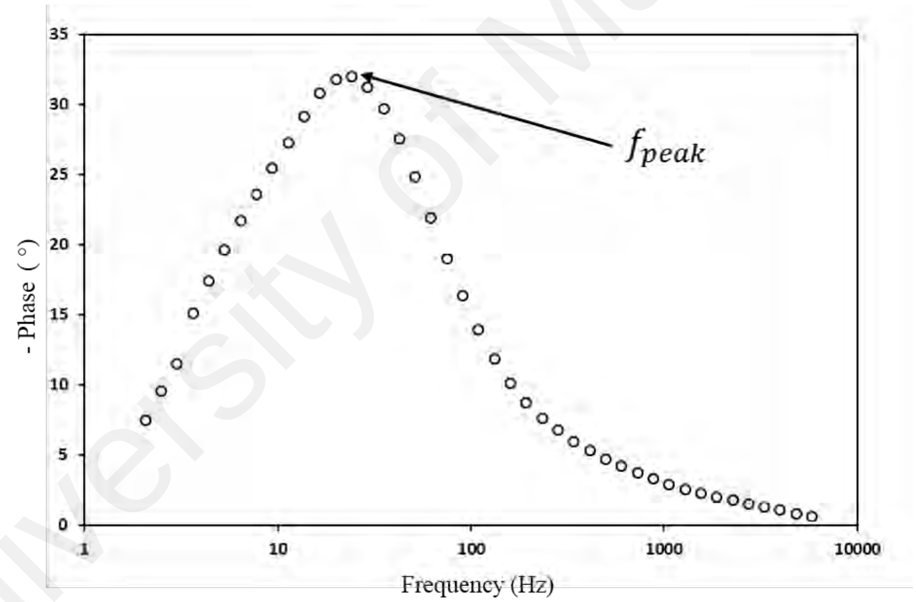

Figure 3.14: Example of bode plot for the electron lifetime measurement.

3.9.3 Incident Photon to Current Efficiency (IPCE)

IPCE or also known as quantum efficiency (QE) is a measure of the efficiency (percentage) of the device converting incident light into electrical energy at a given wavelength. From this measurement, the quality of the QDSSC converting light into electricity can be measured in percentage.

3.10 Summary

QDSSC has three major components which is photoanode, electrolyte and CE. All the component fabrication, fabrication process and characterization details of the QDSSC have been discussed in this chapter. The next chapter be discussed on the result of the experiment in this project.

CHAPTER 4: RESULTS FOR CHARACTERIZATION AND OPTIMIZATION OF MC–PGPEs.

4.1 Introduction

This chapter will display the results acquired from experiments to achieve the first objective which is “to develop and optimize the conductivity of the polysulphide GPE system with methylcellulose (MC) as the host polymer”. Characteristics of the prepared methylcellulose–polysulphide gel polymer electrolyte (MC–PGPE) samples will be presented in this chapter. Eventually, the optimized MC–PGPE will be determined and will be utilized in the fabrication of the QDSSCs in order to fulfil the second and third objectives. EIS, Tafel polarization measurements and FTIR were used to characterize the MC–PGPEs. EIS analysis was done to examine the electrical, ionic transport and dielectric properties of the MC–PGPEs, Tafel polarization measurements were done to examine the effect of electrochemical properties toward the counter electrode (CE) and FTIR analysis has been done to study some molecular structural aspects of the GPE samples.

4.2 Electrochemical Impedance Spectroscopy Analysis

4.2.1 Nyquist Plots

Five samples of the MC–PGPEs with different compositions shown in Table 3.1 and Table 3.2 have been analysed using EIS. Figure 4.1 shows the Nyquist plots obtained for each GPE samples at room temperature. It is to be noted that the Nyquist plots presented in Figure 4.1 have been fitted to the equivalent circuit (inset) by using Equation (3.3).

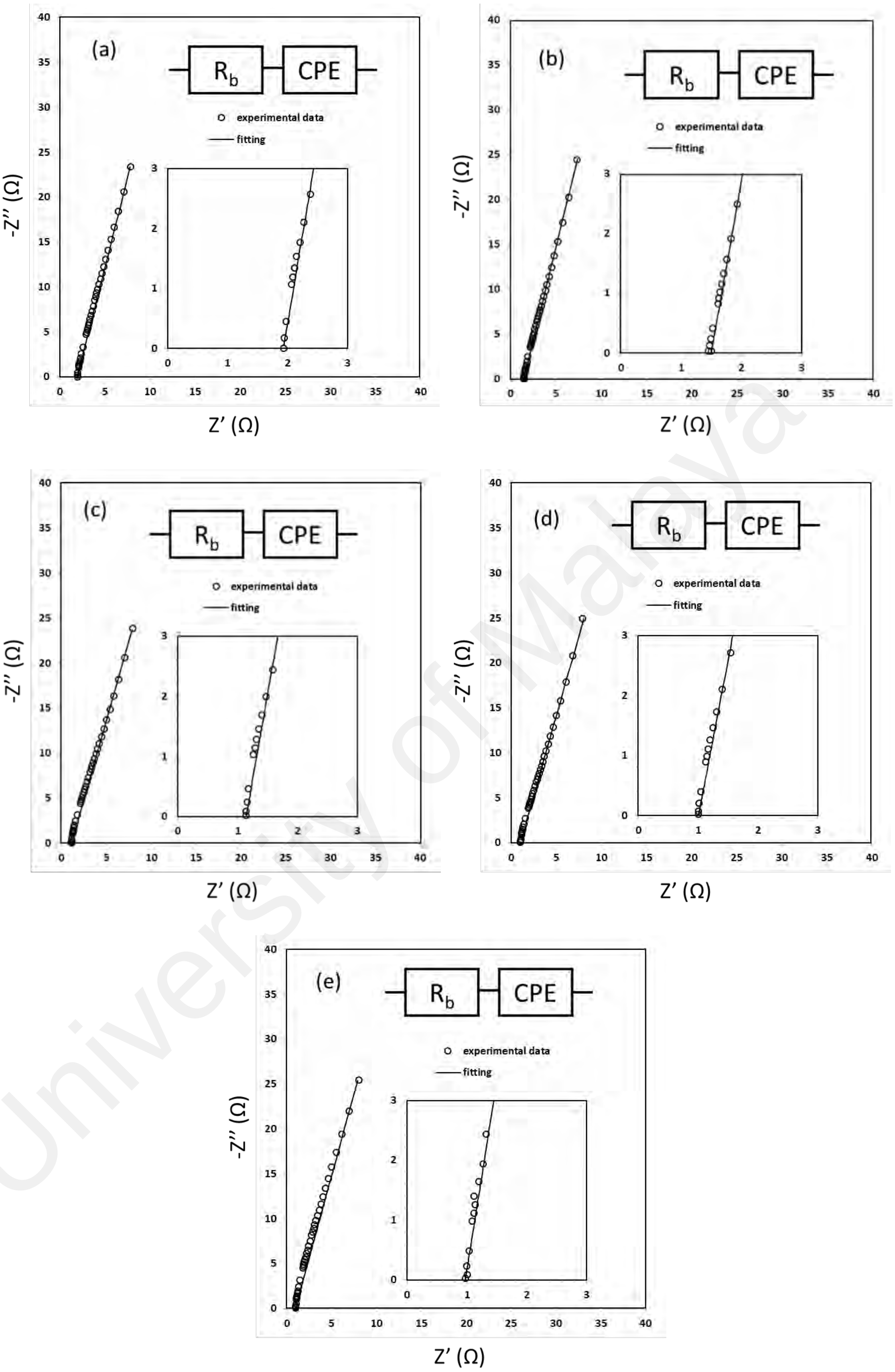

Figure 4.1:(a), (b), (c), (d) and (e) show the Nyquist plots obtained from EIS analysis for GPE sample A, B, C, D and E. The equivalent circuit of the Nyquist plot are also depicted.

4.2.2 Ionic Conductivity of the GPEs at Room Temperature

From the Nyquist plots, the ionic conductivities of MC–PGPE samples have been obtained using Equation (3.1). Figure 4.2 shows the ionic conductivity of the GPE samples at room temperature. From Figure 4.2, it can be seen that the ionic conductivity increased as the concentration of salt increased and sample E possessed the highest ionic conductivity which is (0.19 ± 0.00) S cm^{-1}. It is to be noted that the salt concentration more than the salt concentration in sample E cannot be reached since the salt will not dissolve in the GPE beyond that concentration.

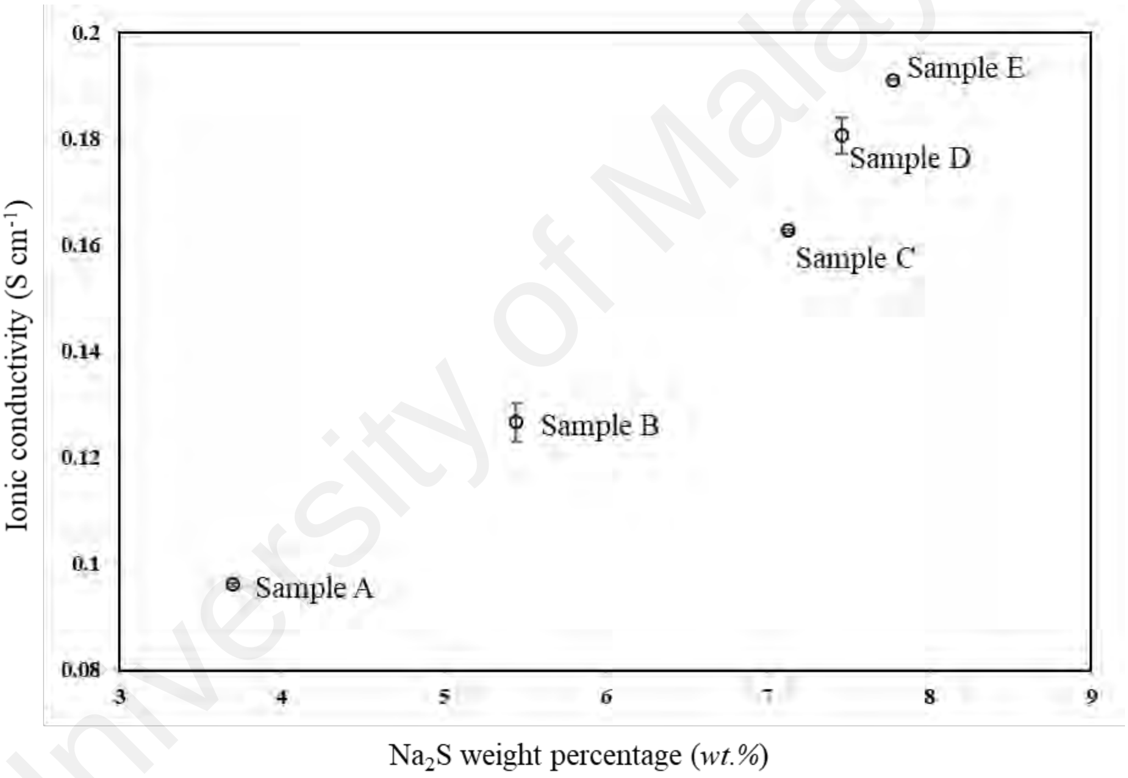

Figure 4.2: The ionic conductivity for different sample of GPEs with different composition of Na_2S at room temperature.

Table 4.1 lists the bulk resistance (R_b) and the calculated ionic conductivity (σ) at room temperature for every GPE samples obtained from the EIS analysis. R_b value was obtained from the fitting of the Nyquist plot while σ values were calculated by using Equation (3.1).

Table 4.1: The parameters obtained from the Nyquist plots which are bulk resistance and ionic conductivity.

GPE	R_b (Ω)	σ (S cm^{-1})
Sample A	1.94 ± 0.01	0.096 ± 0.001
Sample B	1.47 ± 0.05	0.127 ± 0.004
Sample C	1.15 ± 0.01	0.163 ± 0.001
Sample D	1.03 ± 0.02	0.181 ± 0.004
Sample E	0.97 ± 0.01	0.191 ± 0.001

4.2.3 Ionic Transport Studies of the GPEs at Room Temperature

Table 4.2 and Table 4.3 show the calculated ionic transport properties [i.e. ionic diffusion coefficient (D), ionic number of density (n) and ionic mobility (μ)] of the GPE samples at room temperature at frequencies of 0.2 kHz and 2 kHz respectively. The ionic transport properties have been studied at two different frequencies for comparison purposes. D, n and μ have been calculated by using Equations (3.4), (3.5) and (3.6) respectively. Figure 4.3, Figure 4.4 and Figure 4.5 shows the plot of D, n and μ of GPE samples respectively at 0.2 kHz and 2 kHz. From Figure 4.3, can be seen that the D of the GPE samples decreased as the concentration of Na_2S salt increased at both frequencies i.e. 0.2 kHz and 2 kHz. The same trend can be seen in Figure 4.4 for μ of the GPE sample, which decreased with increasing Na_2S salt concentration. The trend of n is however opposite from D and μ which increased with increasing Na_2S salt concentration as can be seen in Figure 4.5.

Table 4.2: The ionic transport properties of every samples which are diffusion coefficient, mobility and number of density at 0.2 kHz.

GPE	D (cm^2 s^{-1})	μ (cm^2 V^{-1} s^{-1})	n (cm^{-3})
Sample A	(2.61 ± 0.49) x 10^2	(1.02 ± 0.17) x 10^4	(0.75 ± 0.21) x 10^{14}
Sample B	(2.40 ± 0.50) x 10^2	(0.94 ± 0.20) x 10^4	(1.00 ± 0.21) x 10^{14}
Sample C	(1.71 ± 0.12) x 10^2	(0.67 ± 0.05) x 10^4	(1.47 ± 0.11) x 10^{14}
Sample D	(1.27 ± 0.37) x 10^2	(0.50 ± 0.15) x 10^4	(2.19 ± 0.64) x 10^{14}
Sample E	(0.79 ± 0.08) x 10^2	(0.31 ± 0.03) x 10^4	(3.69 ± 0.35) x 10^{14}

Table 4.3: The ionic transport properties of every samples which are diffusion coefficient, mobility and number of density at 2 kHz.

GPE	D (cm^2 s^{-1})	μ (cm^2 V^{-1} s^{-1})	n (cm^{-3})
Sample A	$(0.92 \pm 0.13) \times 10^2$	$(3.57 \pm 0.50) \times 10^3$	$(2.20 \pm 0.72) \times 10^{14}$
Sample B	$(0.73 \pm 0.12) \times 10^2$	$(2.85 \pm 0.47) \times 10^3$	$(3.21 \pm 0.51) \times 10^{14}$
Sample C	$(0.54 \pm 0.01) \times 10^2$	$(2.10 \pm 0.01) \times 10^3$	$(4.68 \pm 0.12) \times 10^{14}$
Sample D	$(0.43 \pm 0.11) \times 10^2$	$(1.68 \pm 0.45) \times 10^3$	$(6.95 \pm 1.90) \times 10^{14}$
Sample E	$(0.32 \pm 0.03) \times 10^2$	$(1.24 \pm 0.12) \times 10^3$	$(9.25 \pm 0.85) \times 10^{14}$

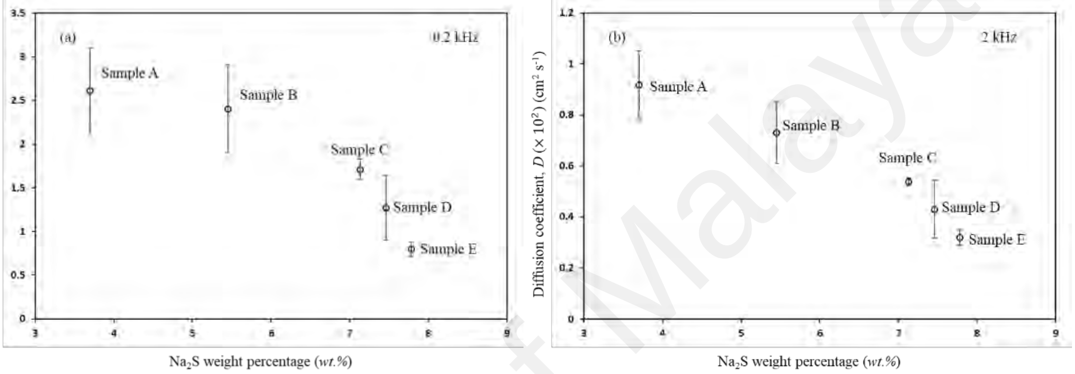

Figure 4.3: Variation of D for every GPE samples at (a) 0.2 kHz and (b) 2 kHz.

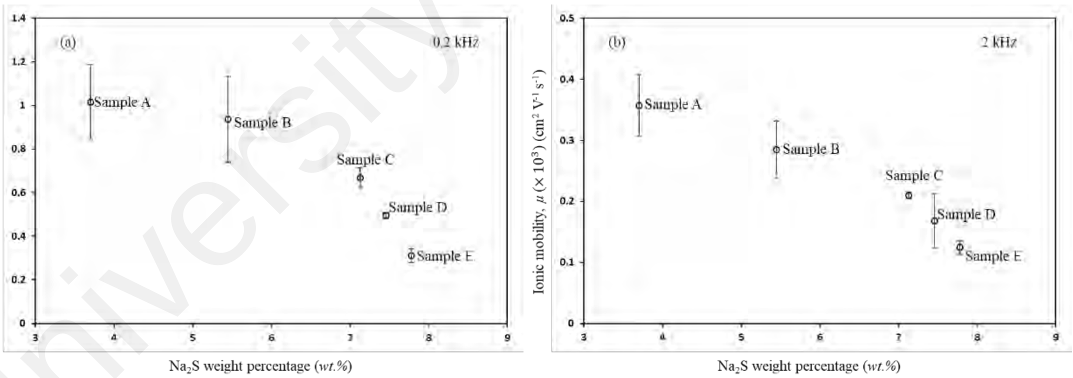

Figure 4.4: Variation of μ for every GPE samples at (a) 0.2 kHz and (b) 2 kHz.

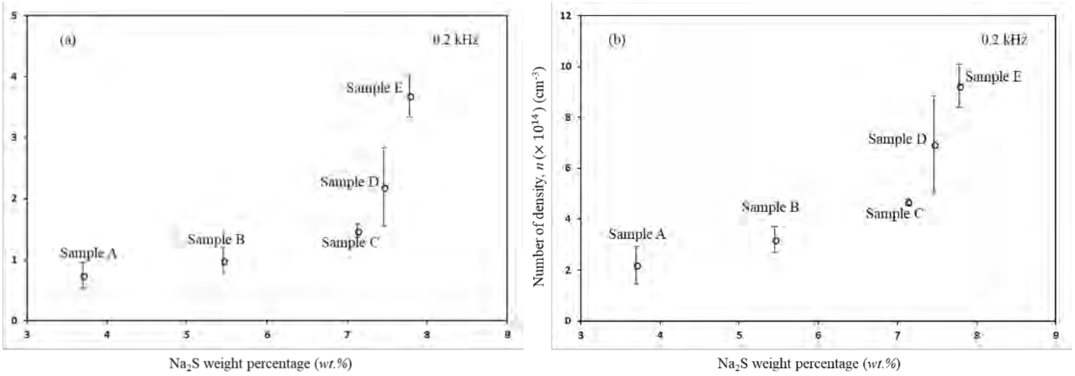

Figure 4.5: Variation of n for every GPE samples at (a) 0.2 kHz and (b) 2 kHz.

4.2.4 Variation of Ionic Transport Properties (*D*, *μ* and *n*) of the Highest Conducting GPE with Temperature

Figure 4.6 and Figure 4.7 depict the ionic transport properties of the highest conducting GPE (Sample E) at various temperatures at frequencies 0.2 kHz and 2 kHz respectively. From the two frequencies, the variation of *D* and *μ* are observed to increase with increasing temperature while the opposite trend is shown by *n* which decreased with the increasing temperature. Table 4.4 and Table 4.5 summarize the variation of ionic transport properties with temperature for the highest conducting GPE at 0.2 kHz and 2 kHz respectively. The ionic transport properties have been calculated by using Equation (3.4), Equation (3.5) and Equation (3.6) respectively.

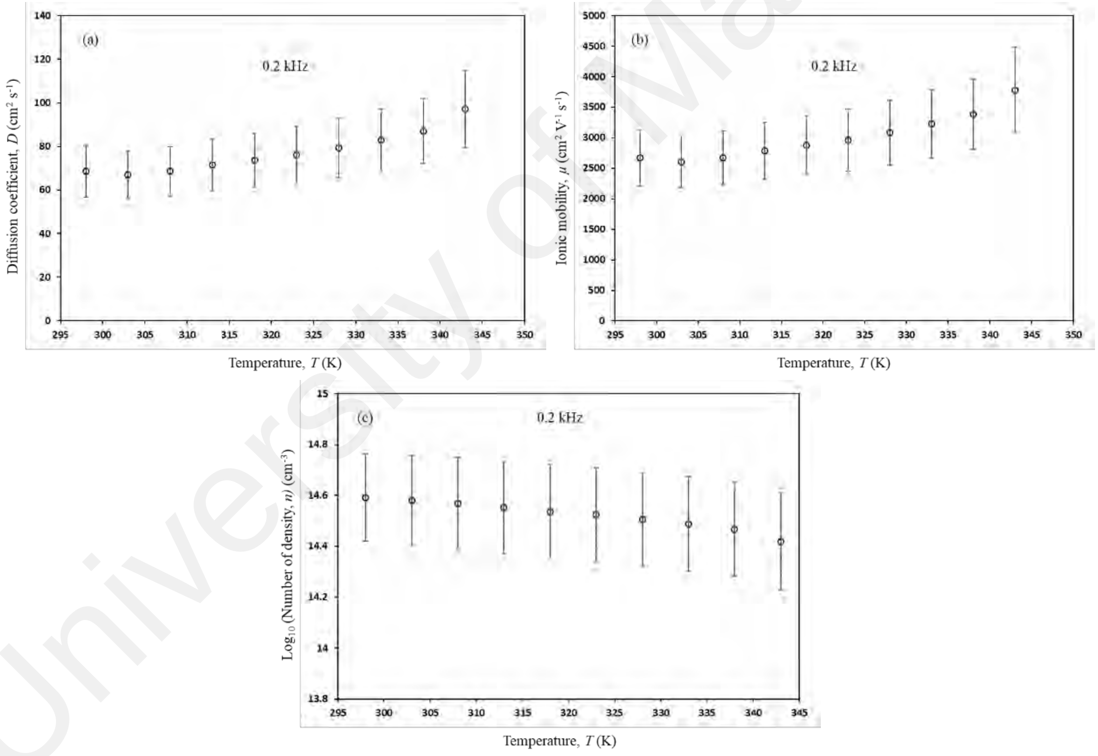

Figure 4.6: Variation of ionic transport properties with temperature for the highest conducting GPE (sample E) at 0.2 kHz frequency. (a), (b) and (c) show the variation of *D*, *μ* and *n* respectively.

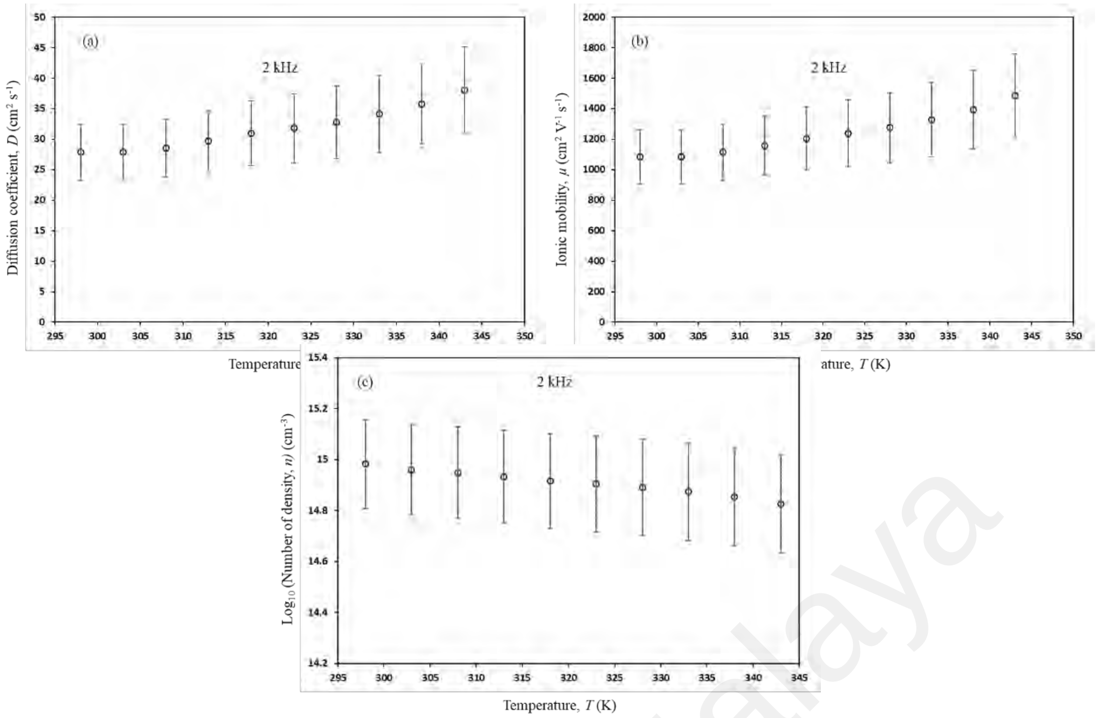

Figure 4.7: Variation of ionic transport properties with temperature for the highest conducting GPE (sample E) at frequency of 2 kHz. (a), (b) and (c) show the variation of *D*, *μ* and *n* respectively.

Table 4.4: The variation of ionic transport properties with temperature of the highest conducting GPE at low frequency (0.2 kHz).

T **(K)**	***D*** **(cm^2 s^{-1})**	***μ*** **(cm^2 V^{-1} s^{-1})**	***n*** **(cm^{-3})**
298	$(0.69 \pm 0.12) \times 10^2$	$(0.27 \pm 0.05) \times 10^4$	$(3.90 \pm 1.45) \times 10^{14}$
303	$(0.67 \pm 0.11) \times 10^2$	$(0.26 \pm 0.04) \times 10^4$	$(4.00 \pm 1.46) \times 10^{14}$
308	$(0.69 \pm 0.12) \times 10^2$	$(0.27 \pm 0.05) \times 10^4$	$(3.91 \pm 1.43) \times 10^{14}$
313	$(0.71 \pm 0.12) \times 10^2$	$(0.28 \pm 0.05) \times 10^4$	$(3.76 \pm 1.38) \times 10^{14}$
318	$(0.73 \pm 0.12) \times 10^2$	$(0.29 \pm 0.05) \times 10^4$	$(3.64 \pm 1.33) \times 10^{14}$
323	$(0.76 \pm 0.13) \times 10^2$	$(0.30 \pm 0.05) \times 10^4$	$(3.54 \pm 1.30) \times 10^{14}$
328	$(0.79 \pm 0.14) \times 10^2$	$(0.31 \pm 0.05) \times 10^4$	$(3.39 \pm 1.25) \times 10^{14}$
333	$(0.83 \pm 0.14) \times 10^2$	$(0.32 \pm 0.06) \times 10^4$	$(3.24 \pm 1.20) \times 10^{14}$
338	$(0.89 \pm 0.15) \times 10^2$	$(0.34 \pm 0.06) \times 10^4$	$(3.09 \pm 1.14) \times 10^{14}$
343	$(0.97 \pm 0.18) \times 10^2$	$(0.39 \pm 0.07) \times 10^4$	$(2.78 \pm 1.04) \times 10^{14}$

Table 4.5: The variation of ionic transport properties with temperature of the highest conducting GPE at low frequency (2 kHz).

T (K)	**D (cm^2 s^{-1})**	**μ (cm^2 V^{-1} s^{-1})**	**n (cm^{-3})**
298	$(0.28 \pm 0.05) \times 10^2$	$(0.11 \pm 0.02) \times 10^4$	$(9.61 \pm 3.52) \times 10^{14}$
303	$(0.28 \pm 0.05) \times 10^2$	$(0.11 \pm 0.02) \times 10^4$	$(9.61 \pm 3.51) \times 10^{14}$
308	$(0.29 \pm 0.05) \times 10^2$	$(0.11 \pm 0.02) \times 10^4$	$(9.38 \pm 3.43) \times 10^{14}$
313	$(0.30 \pm 0.05) \times 10^2$	$(0.12 \pm 0.02) \times 10^4$	$(9.04 \pm 3.31) \times 10^{14}$
318	$(0.31 \pm 0.05) \times 10^2$	$(0.12 \pm 0.02) \times 10^4$	$(8.69 \pm 3.20) \times 10^{14}$
323	$(0.32 \pm 0.06) \times 10^2$	$(0.12 \pm 0.02) \times 10^4$	$(8.48 \pm 3.15) \times 10^{14}$
328	$(0.33 \pm 0.06) \times 10^2$	$(0.13 \pm 0.02) \times 10^4$	$(8.23 \pm 3.07) \times 10^{14}$
333	$(0.34 \pm 0.06) \times 10^2$	$(0.13 \pm 0.02) \times 10^4$	$(7.29 \pm 2.97) \times 10^{14}$
338	$(0.36 \pm 0.07) \times 10^2$	$(0.14 \pm 0.03) \times 10^4$	$(7.55 \pm 2.83) \times 10^{14}$
343	$(0.38 \pm 0.07) \times 10^2$	$(0.15 \pm 0.03) \times 10^4$	$(7.09 \pm 2.65) \times 10^{14}$

4.2.5 Determining Activation Energy Using Arrhenius Equation

Another important parameter that can be obtained from EIS analysis is activation energy (E_a). From Figure 4.8, it can be seen that the conductivity and temperature of the GPE samples have an Arrhenian relationship with E_a and can be calculated using Equation (3.9). Table 4.6 lists all the E_a values for the GPE samples calculated from the gradient of the Arrhenius plots. Sample E which is the highest conducting GPE sample exhibited the lowest E_a (55.25 ± 1.15) meV compared to other GPEs. The trend of E_a value of the GPE samples decreases with increasing of the GPE conductivity.

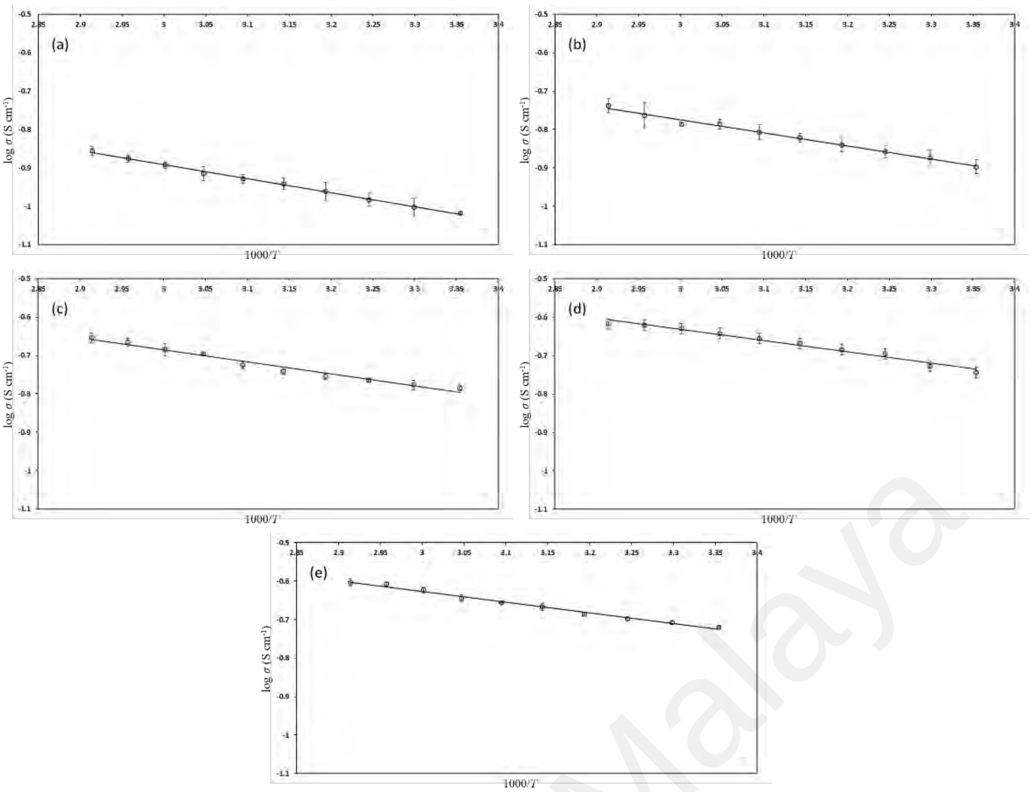

Figure 4.8: Graph of log (σ) versus 1000/T or also known as Arrhenius plot for determining the activation energy of the GPEs samples prepared. (a), (b), (c), (d) and (e) show the Arrhenius plot of GPE sample A, B, C, D and E respectively.

Table 4.6: The activation energy values of the GPE samples acquired from the Arrhenius plot.

GPE	E_a **(meV)**
Sample A	72.49 ± 0.09
Sample B	67.56 ± 1.76
Sample C	62.49 ± 1.46
Sample D	58.19 ± 0.03
Sample E	55.25 ± 1.15

4.2.6 Dielectric of the GPEs at Selected Frequencies

Another important parameter of an electrolyte is the dielectric constant which is related to the stored charge capacity of the electrolyte. Figure 4.9 shows the real part of the dielectric constant versus the Na_2S weight percentage at of 2 kHz. The trend of the GPE dielectric constant in Figure 4.9 followed the same trend of ionic conductivity of the GPE samples shown in Figure 4.2. The dielectric constant increased with increasing salt concentration.

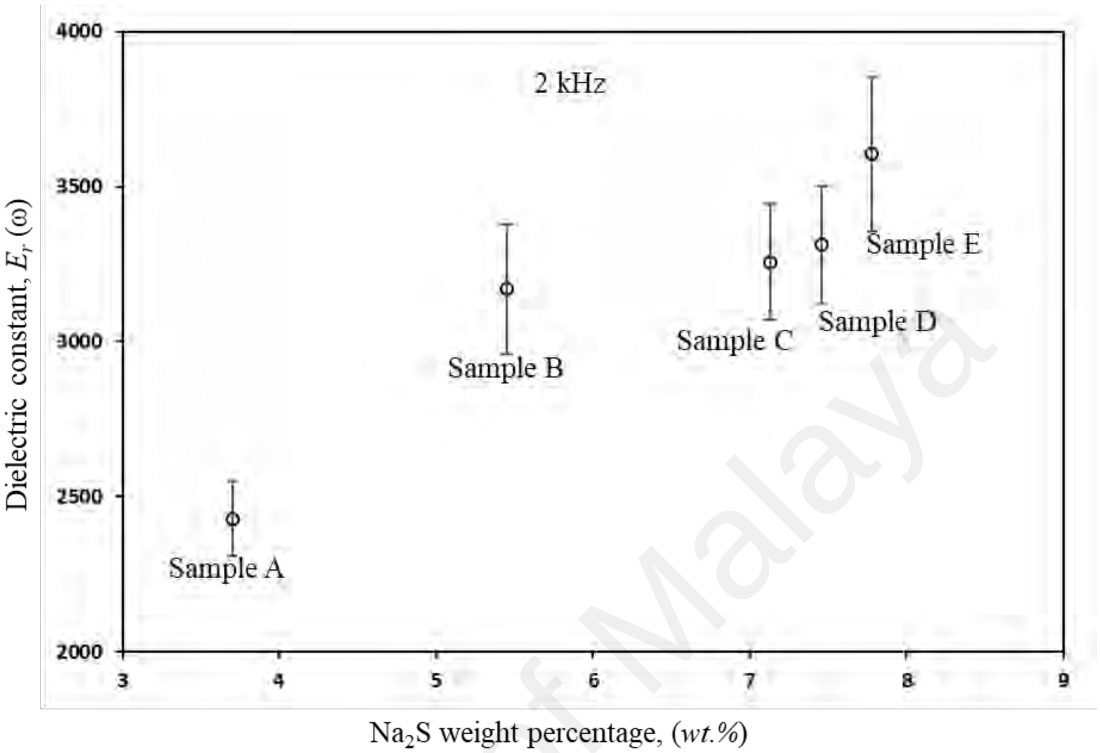

Figure 4.9: Dielectric constant of the GPEs depend on the weight percentage of salt at selected frequency (2 kHz).

4.2.7 Dielectric of the GPEs at Different Temperature

To gain more information on dependence of the dielectric constant with the temperature, graph of dielectric constant (real part) temperature dependence for sample E has been plotted in Figure 4.10. From Figure 4.10, can be seen that the dielectric constant increased with increasing temperature.

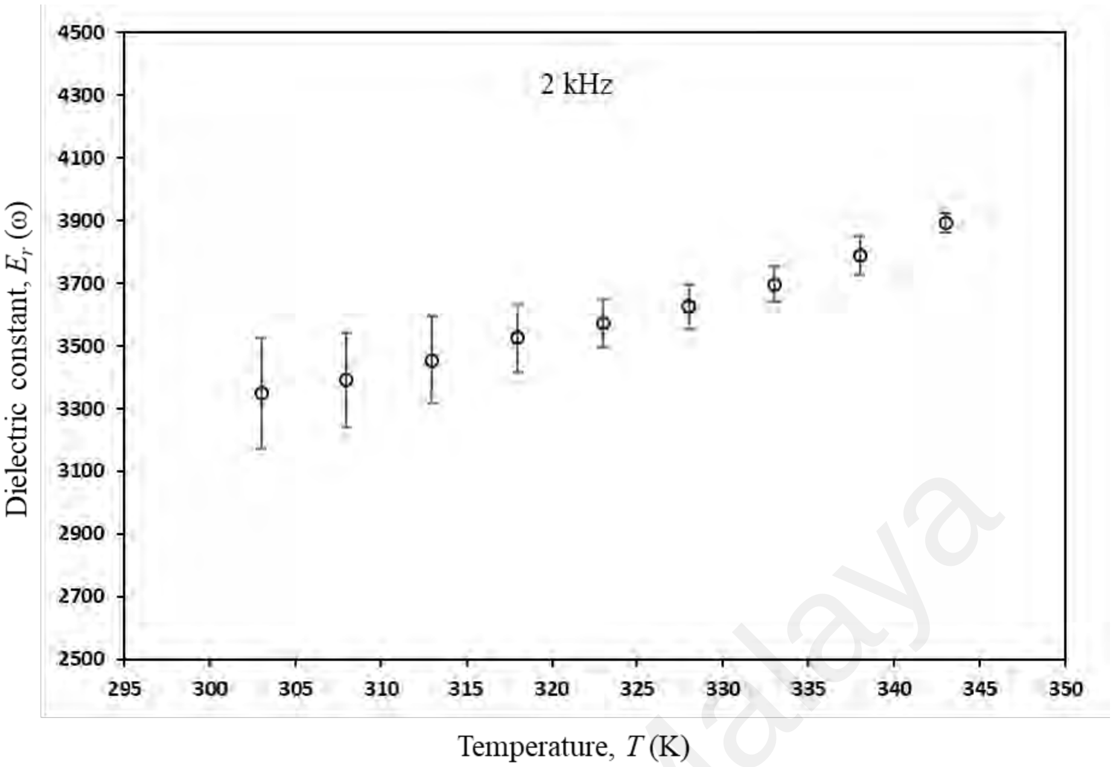

Figure 4.10: The dielectric constant of GPE sample E dependency on temperature.

4.3 Tafel Polarization Measurements

LSV test from potential of -0.6 V to 0.6 V was done to the GPE samples to study the electrocatalytic activity with the Pt CE. Pt CEs were used for the electrodes of the symmetrical dummy cells. Figure 4.11 shows the LSV curves for the electrolyte samples containing different Na_2S composition. From the LSV curves, it can be observed that the current density for every sample attained saturation at above 0.3 V for both polarities. In addition, the equilibrium steady state conditions can be seen as the anodic and cathodic part of the LSV curves are quite similar.

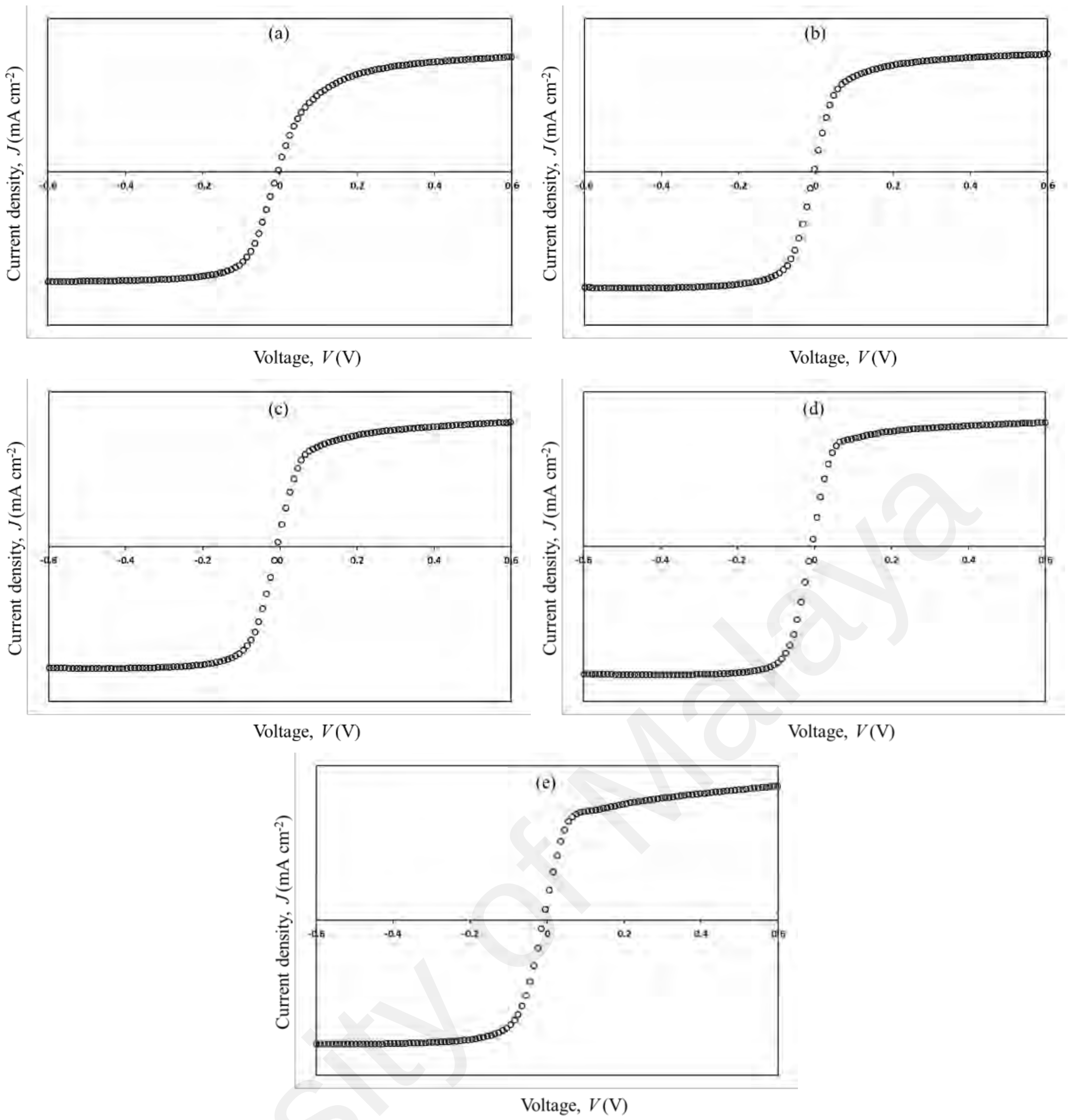

Figure 4.11: Linear sweep voltammograms of GPE samples at different concentration of Na$_2$S with the scan rate of 10 mV/s. (a)–(b) display the LSV curves of GPE sample A–B respectively.

From LSV curves, the Tafel polarization curves of the GPE samples have been plotted by absolute and logarithmic current density value as shown in Figure 4.12. The diffusion of the polysulphide ions ($D_{S_x^{2-}}$) and charge transfer resistance in between Pt CE/electrolyte (R_{dc}) can be calculated from J_{lim} and J_o obtained from the plotted Tafel polarization curve by using Equation (3.10) and (3.11) respectively.

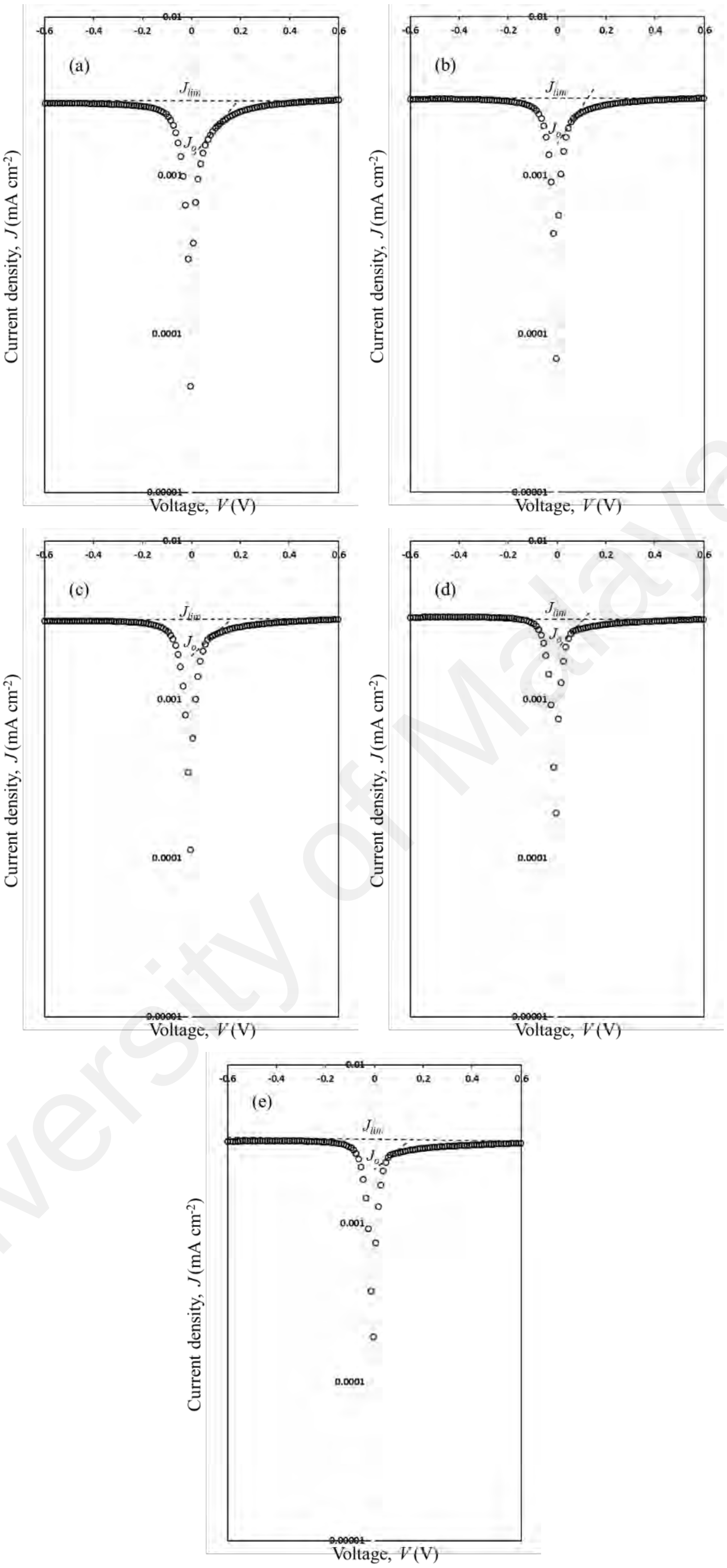

Figure 4.12: Tafel polarization curves for the GPE with different Na_2S composition. (a)–(b) display the LSV curves of GPE sample A–B respectively.

The parameters obtained from Tafel polarization measurement such as J_{lim}, J_o, $D_{S_x^{2-}}$ and R_{dc} are summarized in Table 4.7. The trend of J_{lim} increased with increasing Na_2S concentration. The same trend was observed with J_o parameter i.e. increased with increasing Na_2S concentration. Also, the same trend for R_{dc} was observed with salt concentration. However, the $D_{S_x^{2-}}$ trend from Tafel measurement decreased with increasing salt concentration.

Table 4.7: Parameters obtained from the Tafel polarization measurements of GPEs with different Na_2S compositions.

Sample	**J_{lim} (mA cm^{-2})**	**J_o (mA cm^{-2})**	**$D_{S_x^{2-}}$ (x 10^{-6} cm^2 s^{-1})**	**R_{dc} (Ω cm^2)**
A	3.07 ± 0.49	1.43 ± 0.12	1.93 ± 0.31	8.99 ± 0.76
B	3.16 ± 0.01	1.57 ± 0.01	1.39 ± 0.03	8.20 ± 0.31
C	3.26 ± 0.01	1.83 ± 0.12	1.08 ± 0.00	7.02 ± 0.46
D	3.36 ± 0.05	2.03 ± 0.06	1.08 ± 0.01	6.32 ± 0.18
E	3.54 ± 0.03	2.27 ± 0.06	1.08 ± 0.01	5.67 ± 0.15

4.4 Fourier Transform Infrared Analysis (FTIR)

4.4.1 FTIR Spectra for MC–PGPEs, MC and Distilled Water

FTIR analysis have been done in order to study the structural aspect of the MC–PGPE. Figure 4.13 shows the FTIR spectra of every GPE samples in the absorbance mode. Figure 4.14 and Figure 4.15 show the FTIR spectra of distilled water and MC respectively. From the FTIR spectrum of distilled water, there are two peaks appeared at 1630 cm^{-1} and 3350 cm^{-1} which correspond to the O–H stretching (Morales-Ortega et al., 2013). Several peaks have been observed from the FTIR spectrum of MC: 950 cm^{-1}, 1320 cm^{-1}, 1380 cm^{-1}, 1460 cm^{-1} and 2900 cm^{-1} are the peaks corresponding to the C–H stretching of CH_2 and CH_3, 1050 cm^{-1} correspond to C–O–C stretching and 3350 cm^{-1} correspond to O–H stretching (Oliveira et al., 2015). In the FTIR spectra of GPE samples, two peaks are observed which are 1630 cm^{-1} and 3350 cm^{-1} and there are no peak observed responsible for the presence of MC. This is due to the very small absorbance of MC compared to the distilled water as can be seen in the FTIR spectrum. In addition, the composition of distilled water is much bigger compared to MC. In the next section, influence of MC toward FTIR spectra of MC–PGPE samples will be revealed.

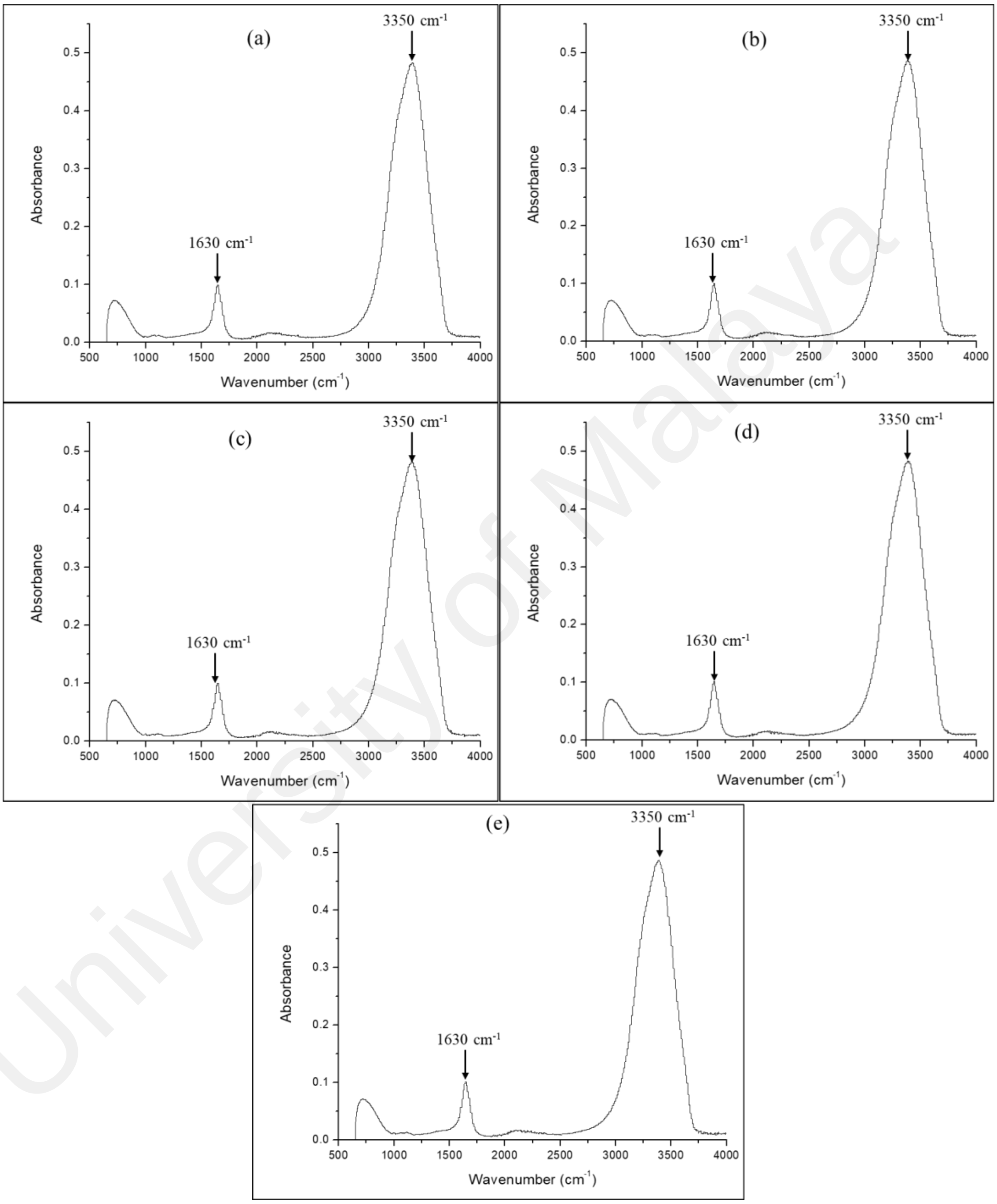

Figure 4.13: FTIR spectra of the GPE samples. (a), (b), (c), (d) and (e) are the FTIR spectrum of sample A, B, C, D and E respectively.

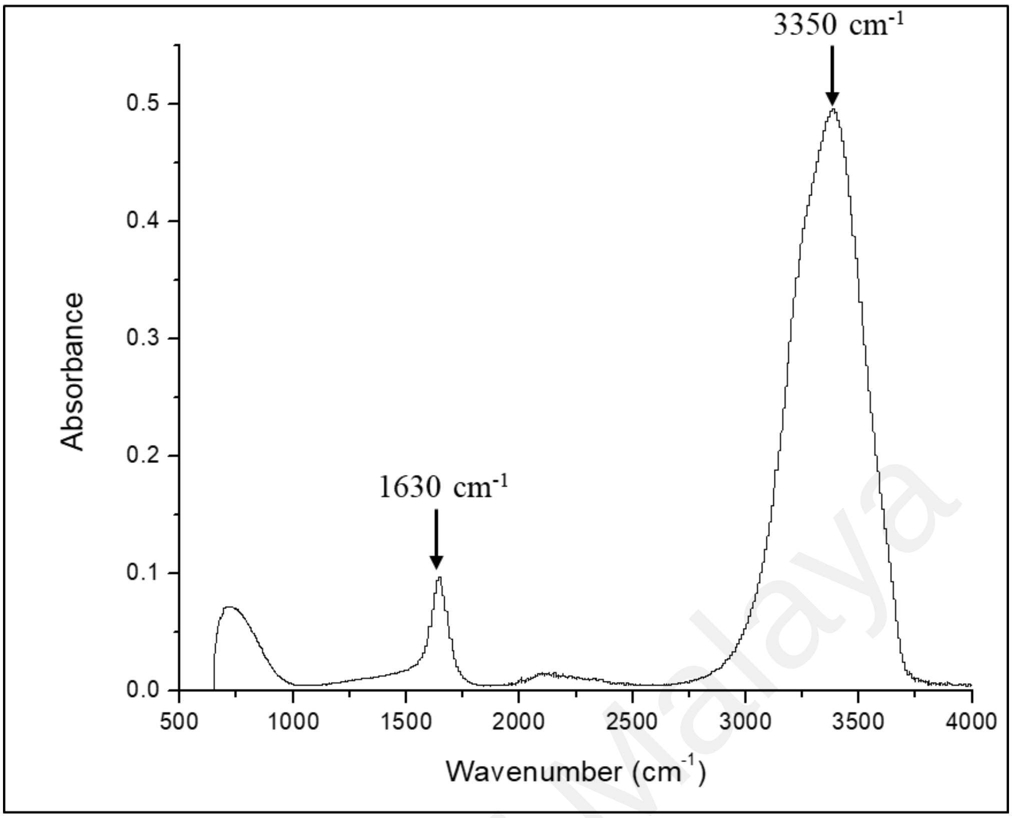

Figure 4.14: The FTIR spectra of distilled water.

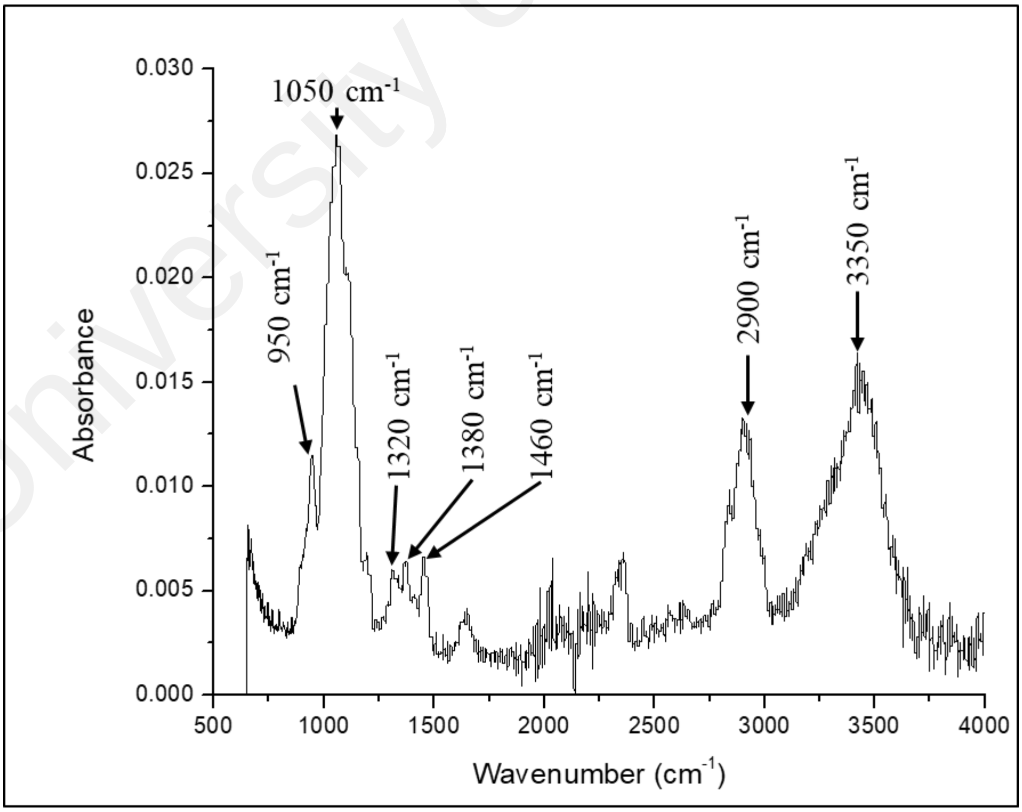

Figure 4.15: The FTIR spectra of MC.

4.4.2 Combined FTIR Spectra for Every GPE Samples, MC and Distilled Water

The combined FTIR spectra of GPE samples, distilled water and MC are shown in Figure 4.16. This is for purpose of tracing the characteristics of the GPE samples based on its composition (distilled water and MC). The composition of distilled water in the GPEs is high (84.6–92.5 *wt.%*). The FTIR spectra of GPE samples is similar to distilled water. However, there are some differences in the spectra of GPE samples compared to that of distilled water due to the presence of the MC as shown in the box at wavenumber 850–1200 cm^{-1} and 2350–3250 cm^{-1}. Due to the presence of the MC, the absorbance in FTIR spectra of GPE samples is slightly higher compared to the FTIR spectrum of distilled water in the boxes shown in the figure below.

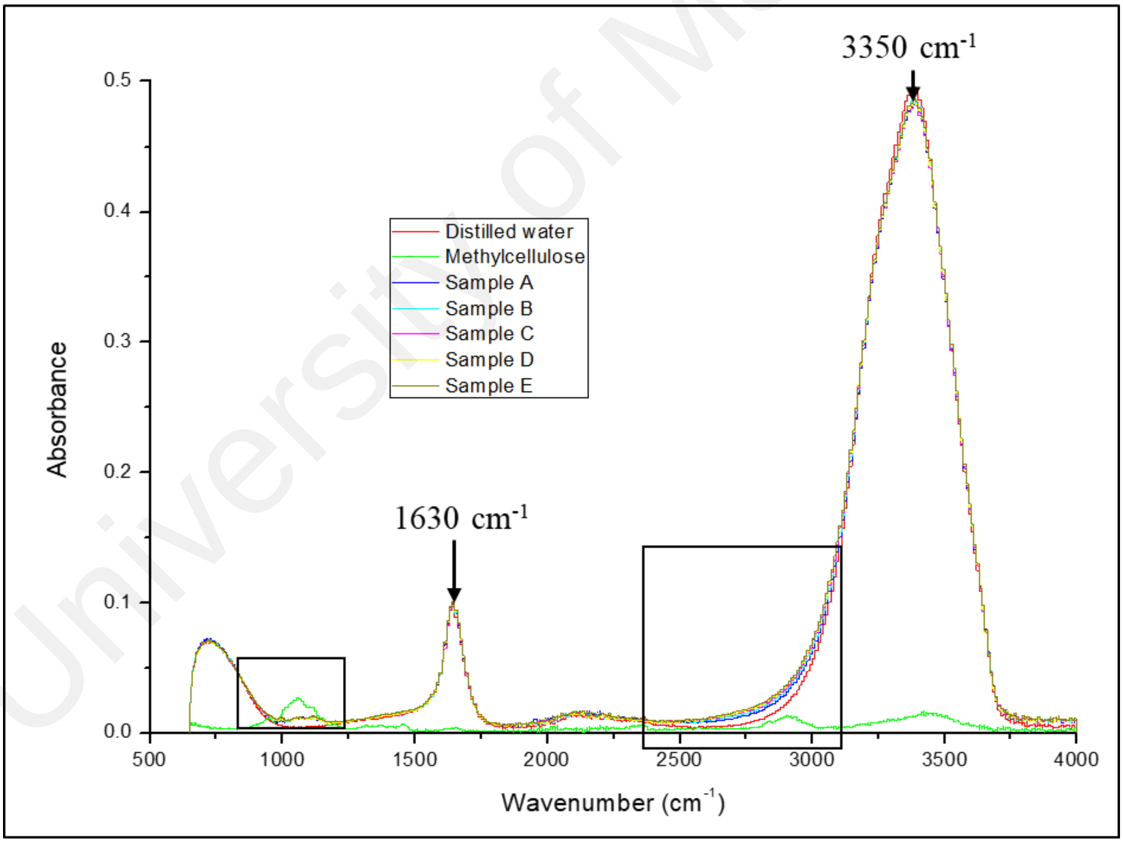

Figure 4.16: The combined FTIR spectra from GPE samples, MC and distilled water. From this figure, can be seen that the spectra of GPE samples are similar to the distilled water spectra. However, there is some differences at several regions (in the box) due to the presence of MC.

4.4.3 Combined FTIR Spectra Focused at Wavenumber of 850-1200 cm^{-1}

At wavenumbers from 850 cm^{-1} to 1200 cm^{-1}, it can be seen that the FTIR spectra of GPE samples differ to that of distilled water FTIR spectrum. The absorbance of the GPE samples spectra is slightly higher than the distilled water spectrum. This is due to the presence of MC in the composition of GPE samples. At wavenumber 850–1200 cm^{-1}, there are two peaks corresponding to the C–O–C and C–H stretching at 1050 cm^{-1} and 950 cm^{-1} respectively. These peaks have influenced the GPE samples FTIR spectra to exhibit slightly higher absorbance compared to that of distilled water. Figure 4.17 shows the FTIR spectra focused at wavenumber 850–1200 cm^{-1}.

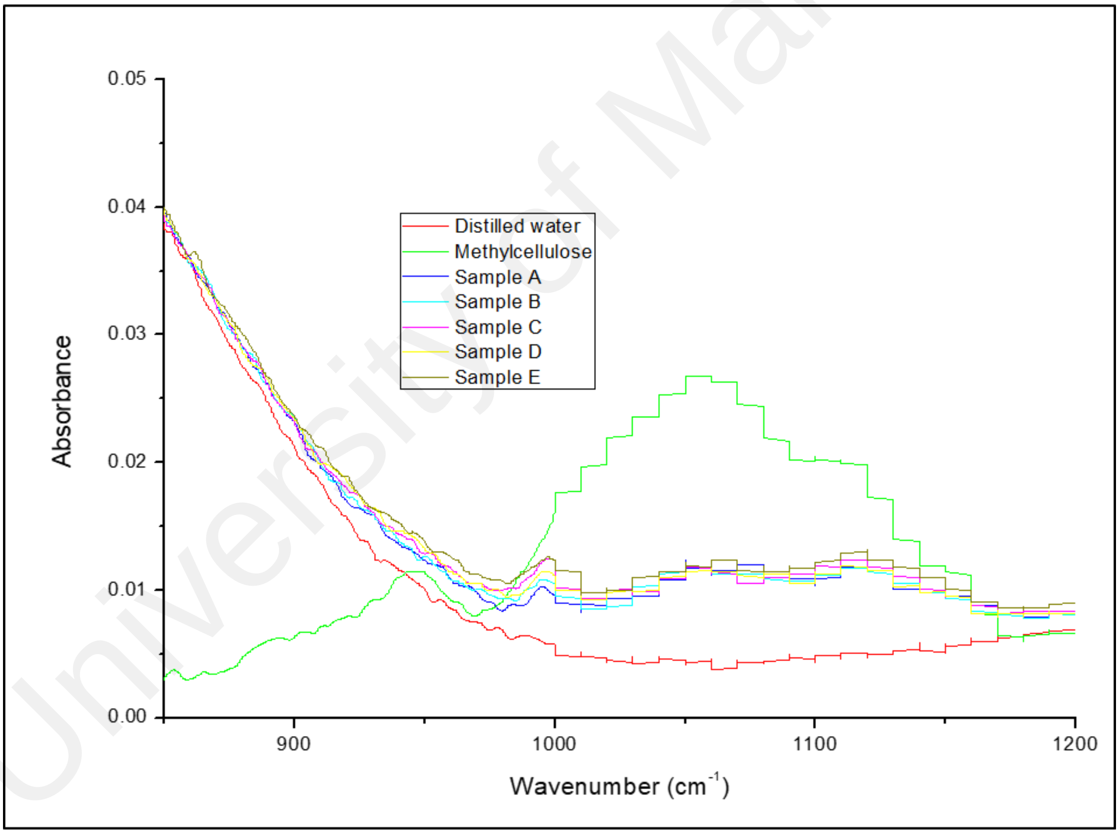

Figure 4.17: The difference between of MC–PGPE spectra compared to that of distilled water due to the presence of MC.

4.4.4 Combined FTIR Spectra Focused at Wavenumber of 2350–3250 cm^{-1}

Another difference of GPE spectra can be observed at wavenumbers between 2350 cm^{-1} to 3250 cm^{-1} as show in Figure 4.18. Absorbance revealed in the spectra of the GPE samples is higher compared to that of distilled water. This is due to the presence of MC in the composition of the GPE samples. At wavenumber 2350 to 3250 cm^{-1}, there is one peak corresponding to the C–H stretching in the structure of MC which is at 2900 cm^{-1}. This peak has influenced the GPE samples FTIR spectra to exhibit slightly higher absorbance compared to that of distilled water as shown in the figure below.

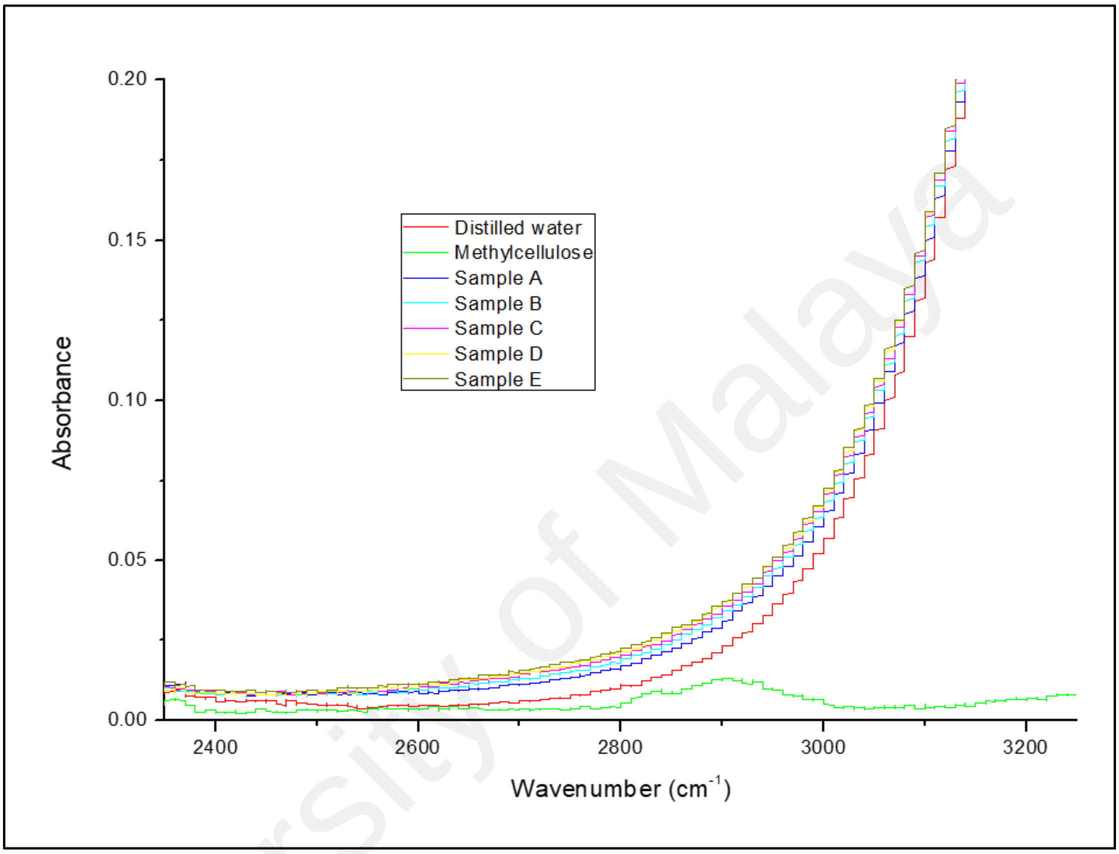

Figure 4.18: FTIR spectra of GPE samples, distilled water and MC at wavenumber of 2350–3250 cm^{-1}. The difference between the FTIR spectra of the GPE samples from that of distilled water is due to the MC included in the GPEs sample composition.

4.5 Summary

- The ionic conductivity increased as the concentration of salt increased and sample E (7.78 *wt.%* Na_2S, 3.54 *wt.%* MC, 88.46 *wt.%* distilled water, 0.22 *wt.%* S) possessed the highest ionic conductivity which is (0.19 ± 0.00) S cm^{-1}.
- The trend of E_a value of the GPE samples decreased with increasing of the GPE conductivity. Sample E which is the highest conducting GPE sample exhibited the lowest E_a (55.25 ± 1.15) meV.

- Ionic transport properties versus Na_2S concentration: D and μ of the GPE samples decreased with increasing concentration of Na_2S salt at 0.2 kHz and 2 kHz frequencies. While the trend of n is opposite from D and μ which increased with increasing Na_2S salt concentration.
- Ionic transport properties versus T: From 0.2 kHz and 2 kHz frequencies, the variation of D and μ are observed to increase with increasing temperature while the opposite trend is shown by n which decreased with the increasing temperature.
- From Tafel polarization measurement, the trend of J_{lim} and J_o are increased with increasing Na_2S concentration. The trend of R_{dc} observed decrease with increasing salt concentration. However, the $D_{S_x^{2-}}$ trend from Tafel measurement decreased with increasing salt concentration.
- There are some differences in the spectra of GPE samples compared to that of distilled water spectrum due to the presence of the MC as shown at wavenumbers from of 850 to 1200 cm^{-1} and 2350 to 3250 cm^{-1}. Due to the presence of the MC, the absorbance in FTIR spectra of GPE samples is slightly higher compared to that of distilled water.

CHAPTER 5: RESULTS FOR OPTIMIZATION OF PHOTOANODE

5.1 Introduction

This chapter will present the results obtained from the experiment to achieve the second objective of this work which is “to optimize the photoanode sensitized with CdS”. To achieve this, the photoanode will be deposited with CdS QDs at different SILAR cycles (1 to 10) designated as TiO_2/CdS(1–10) and characterized. QDSSCs will be fabricated with TiO_2/CdS(1–10) photoanodes in order to determine the best number of SILAR cycles to be used for the CdS QDs deposition. To further improve the performance of the QDSSC, passivation layers i.e. ZnS and SiO_2 have been coated to the optimized photoanode deposited with CdS QDs. The electrolyte and CE used for the QDSSCs fabrication in this chapter were the optimized methylcellulose–polysulphide gel polymer electrolyte (MC–PGPE) obtained from previous experiment and Pt CE respectively. FESEM, EDX and UV–Vis absorption were used for the characterization of the photoanode. *J–V*, EIS and IPCE analysis were used to characterize the QDSSCs fabricated in this section.

5.2 Optimization of SILAR Cycles

5.2.1 Morphology Study of the TiO_2 Photoanode Using FESEM

FESEM has been used to determine the morphology of the TiO_2 particles and the thickness of the TiO_2 layers that have been deposited. There are two layers of TiO_2 deposited i.e. the compact/first layer and mesoporous/second layer. Figure 5.1(a) shows the morphology of the photoanode surface containing only the nanocrystalline TiO_2 porous network formed with particle size of ~21 nm. It can be seen that the morphology of nanocrystalline semiconductor TiO_2 is granular in shape and also the layer of TiO_2 is porous. Granular particle shape and a porous nature of TiO_2 layer are essential for the good performance of QDSSCs. These properties will enhance the amount of quantum dot sensitizers attached to the TiO_2 surface. In addition, granular particle shape and a porous of TiO_2 layer could promote more surface contact between photoanode and electrolyte. Figure 5.1(b) shows the cross-sectional image of the TiO_2 layers deposited on the FTO glass which revealed the thickness of the TiO_2 compact (P90) and mesoporous (P25) layer to be around ~1 µm and ~13 µm respectively. The compact layer is to prevent the possibility of electron recombination from FTO substrate with the redox mediator in electrolyte while the porous layer is site for the QDs deposition.

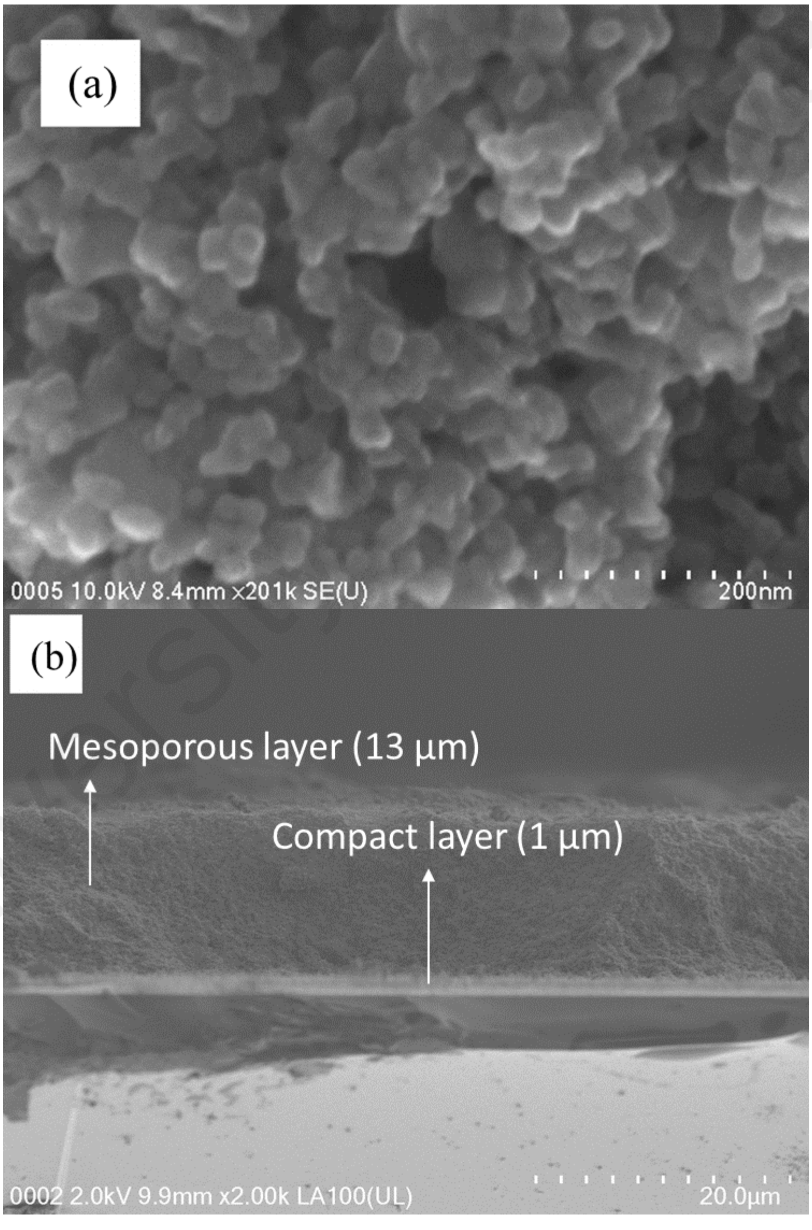

Figure 5.1: (a) and (b) shows the FESEM images of the TiO_2 particles and cross sectional of TiO_2–photoanode respectively.

5.2.2 UV-Vis Characterization of TiO_2/CdS–Photoanodes Prepared with 1–10 SILAR Cycles

Deposition of CdS on the photoanode with TiO_2 has been controlled by varying the SILAR cycles. Figure 5.2 shows the UV–Vis absorption of photoanode with TiO_2 layer, Figure 5.3 shows the UV–Vis absorption of TiO_2/CdS photoanodes deposited with different number of SILAR cycles and Figure 5.4 combine all the spectra obtained.

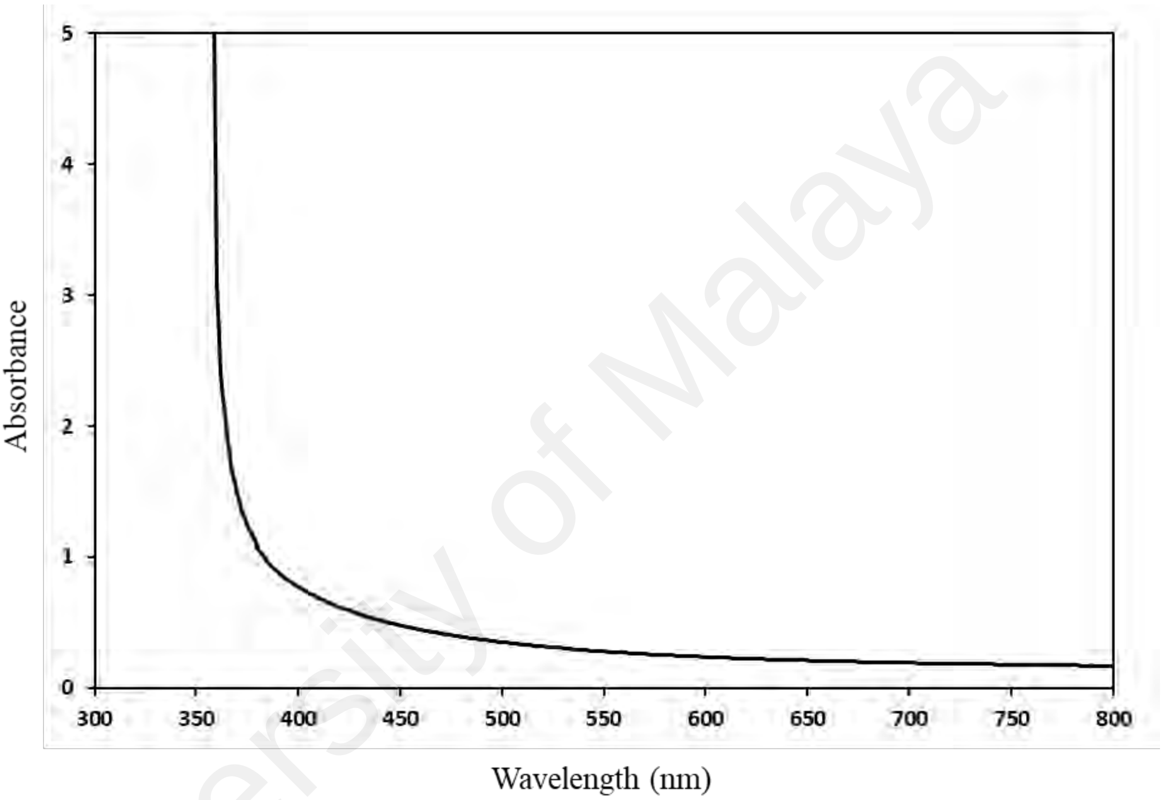

Figure 5.2: UV–Vis absorption of TiO_2 photoanode.

From Figure 5.3, the absorption peak which is related to the energy gap can be obtained. The absorption peaks of TiO_2/(1–5) photoanodes are located at 480 nm, 482 nm, 483 nm, 504 nm and 511 nm respectively. Different absorption peaks obtained from TiO_2/CdS(1–5) photoanodes indicate that different SILAR cycles will result in different optical band gap value. The number of SILAR cycle applied will influence the size of the CdS QDs deposited (Lokhande et al., 2004). The optical band gap value will be shown in the next section.

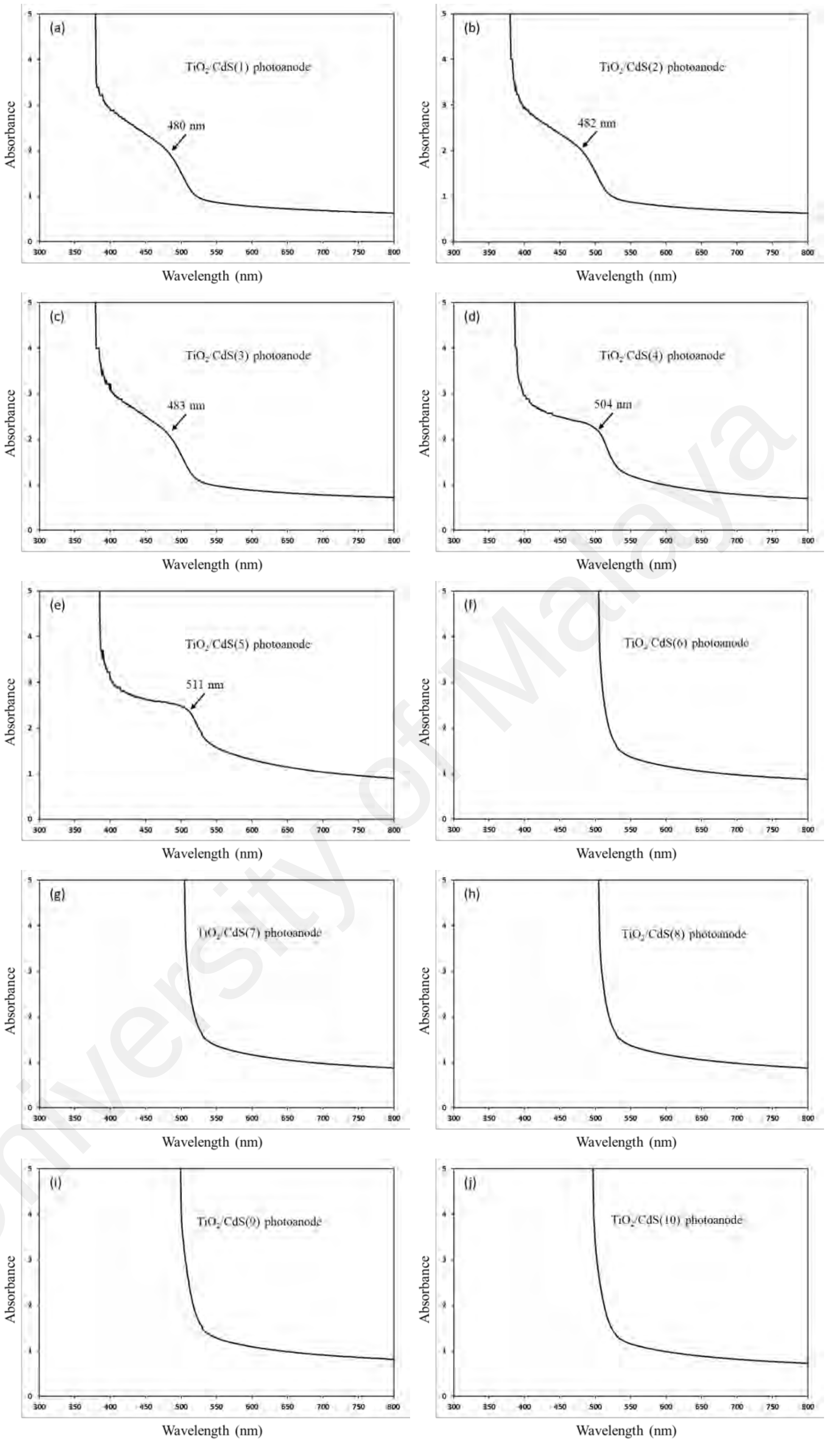

Figure 5.3: UV–Vis absorption of TiO_2/CdS(1–10) photoanodes. (a)–(j) represent the absorption of photoanode deposited with CdS by 1–10 SILAR cycles respectively.

Obviously, photoanodes with CdS QDs show higher absorption compared to the photoanode with only TiO_2 layers as can be seen in Figure 5.4. This showed that the CdS QDs deposited using SILAR method exhibited excellently in absorbing light. From TiO_2/CdS(1) to TiO_2/CdS(5), the trend of absorption increased with increasing the number of SILAR cycles in the range of 380 nm to 800 nm. However, there is no absorption observed in the range from 380 nm to 540 nm by photoanodes deposited with CdS QDs using 6 to 10 SILAR cycles [TiO_2/CdS(6) to TiO_2/CdS(10)]. These indicate that the photoanodes deposited with CdS QDs using higher than five SILAR cycles no longer absorb light in the range of 380 nm to 540 nm as shown in the absorption spectra below.

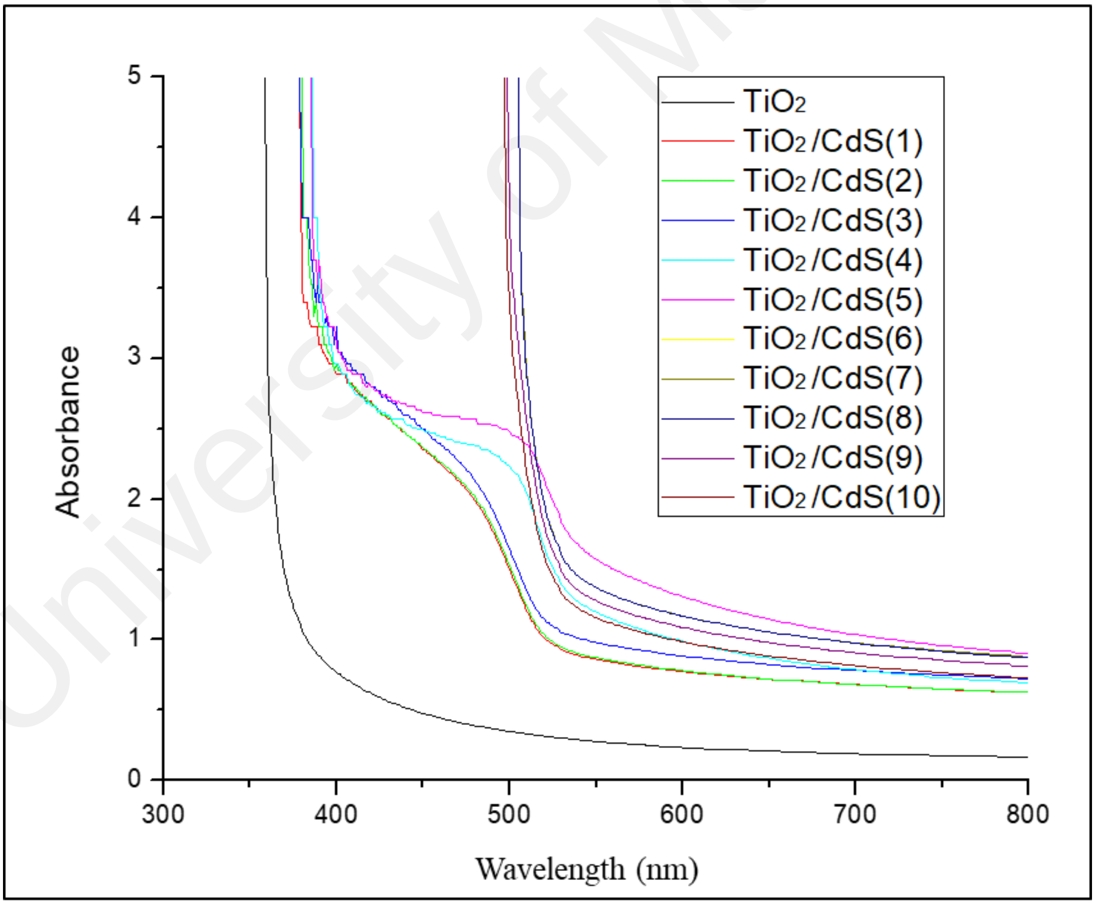

Figure 5.4: UV–Vis spectra from TiO_2 and TiO_2/CdS(1–10) photoanodes.

5.2.3 Determination of Optical Energy Transition of TiO_2/CdS–Photoanodes (1–10 SILAR Cycles)

Based on Beer–Lambert's equation, optical energy transition or band gap of the TiO_2/CdS(1–10) photoanodes have been determined by plotting a graph of $(\alpha hv)^2$ versus (hv) where α is absorbance (obtained from UV-vis measurement), h is Plank's constant and v is a frequency of electromagnetic wave. Figure 5.5 shows the Tauc's plot of TiO_2 photoanode with band gap estimated at 3.21 eV which is the same as the standard value, 3.2 eV.

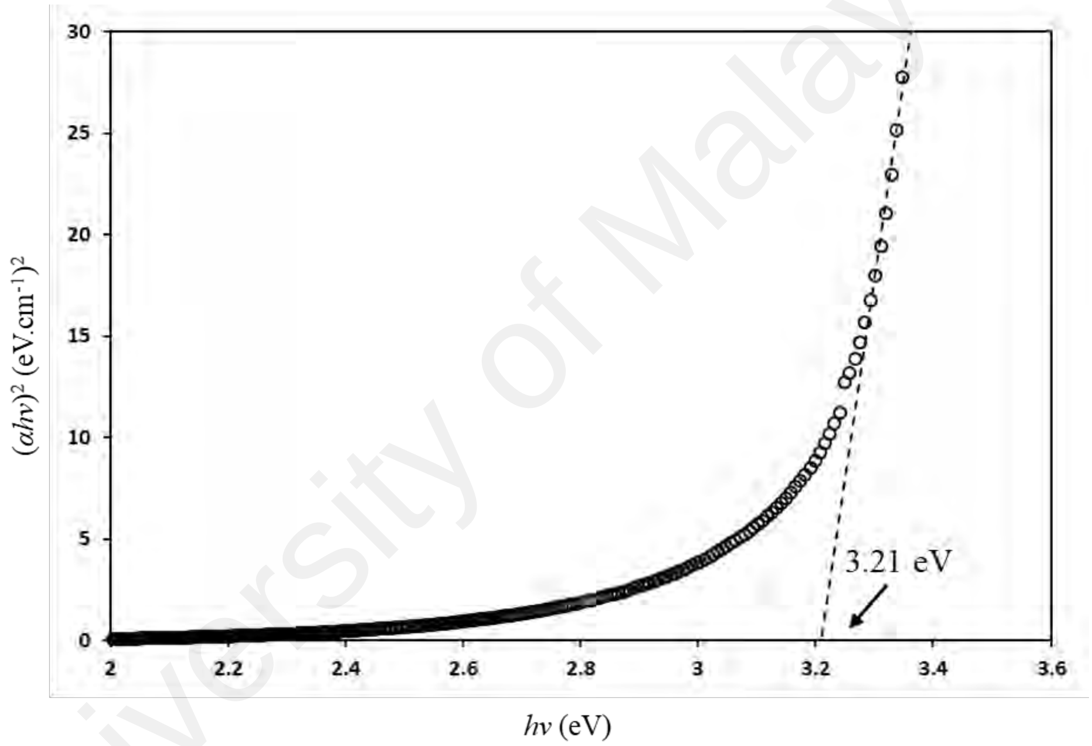

Figure 5.5: $(\alpha hv)^2$ versus hv plot of TiO_2 photoanode for band gap estimation.

$(\alpha hv)^2$ versus hv plot for the TiO_2 photoanode that have been deposited with 1–10 SILAR cycles CdS QDs are shown in Figure 5.6. The band gap of the TiO_2/CdS(1–10) photoanodes that have been estimated are listed in Table 5.1. From TiO_2/CdS(1) to TiO_2/CdS(5), the energy band gap of the TiO_2/CdS photoanode decreased with increasing of number of SILAR cycles. From TiO_2/CdS(6) to TiO_2/CdS(10), the energy band gap of the TiO_2/CdS photoanode is almost constant with increasing of number of SILAR cycles.

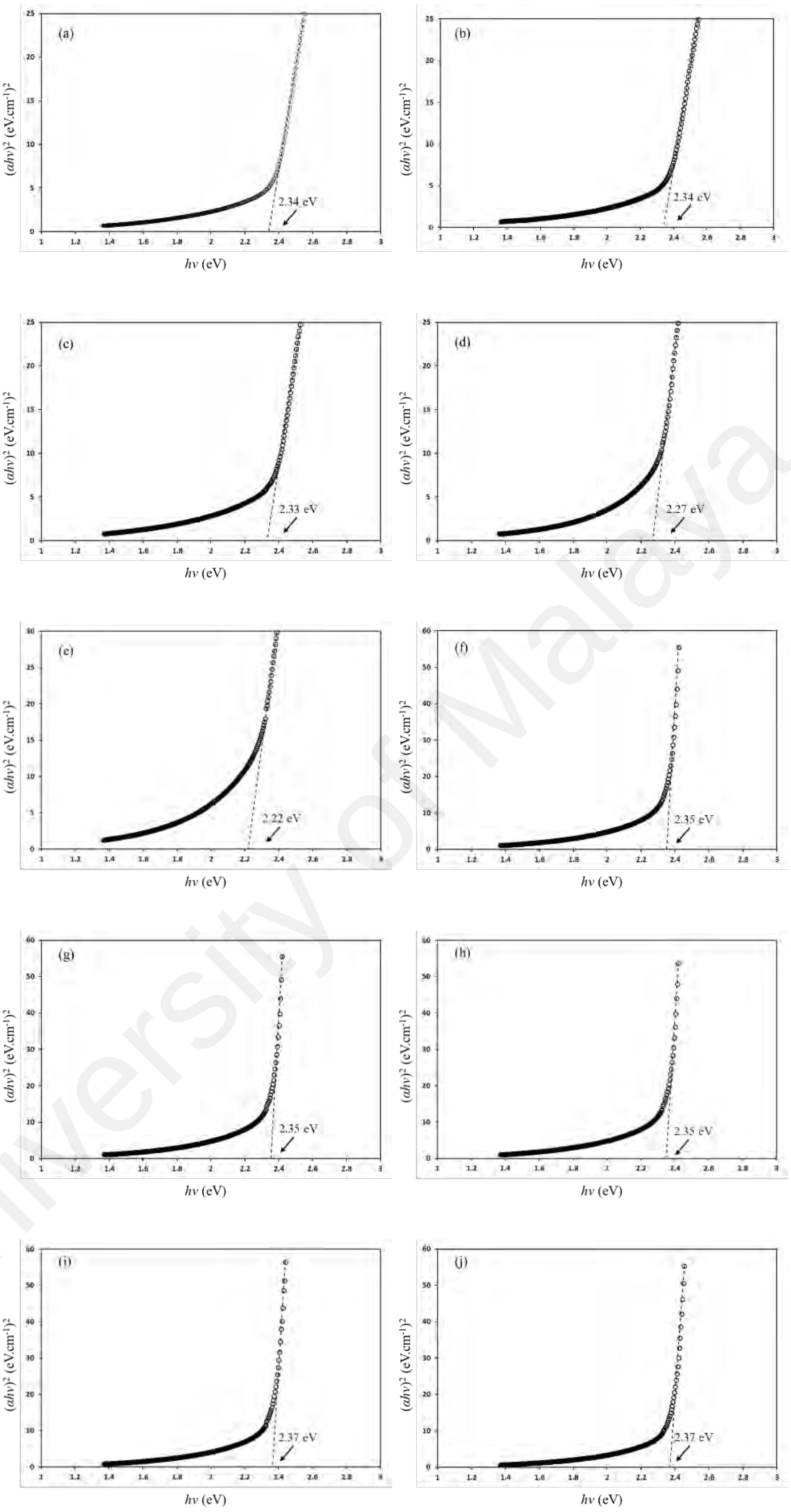

Figure 5.6: $(\alpha h\nu)^2$ versus $(h\nu)$ graph of TiO_2/CdS(1–10) photoanodes for the band gap estimation.

Table 5.1: The absorption edge and energy band gap obtained from the UV–Vis absorption spectra.

Photoanode	Absorption peak (nm)	Band gap (eV)
TiO_2	-	3.22
TiO_2/CdS(1)	480	2.34
TiO_2/CdS(2)	482	2.34
TiO_2/CdS(3)	483	2.33
TiO_2/CdS(4)	504	2.27
TiO_2/CdS(5)	511	2.22
TiO_2/CdS(6)	-	2.35
TiO_2/CdS(7)	-	2.35
TiO_2/CdS(8)	-	2.35
TiO_2/CdS(9)	-	2.37
TiO_2/CdS(10)	-	2.37

5.2.4 *J–V* characterization of MC–PGPE Based QDSSCs Fabricated with Different Types of TiO_2/CdS photoanode (1–10 SILAR cycles)

J–V characterization has been done with QDSSCs fabricated with 10 different TiO_2/CdS photoanodes (1–10 SILAR cycles). The electrolyte used in the fabrication of the QDSSCs is the MC–PGPE that has been optimized and the CE material used is Pt. Figure 5.7 shows the *J–V* curves obtained from this experiment while Table 5.2 lists the *J–V* parameters obtained from this experiment. From the *J–V* characterization, the *PCE* increased from QDSSCs fabricated with TiO_2/CdS(1) to TiO_2/CdS(5) photoanode. However, the trend of *PCE* is decreasing when the number of SILAR used for the CdS deposition is beyond 5 SILAR cycles i.e. QDSSCs fabricated by using TiO_2/CdS(6) to TiO_2/CdS(10) photoanodes. This trend can be seen in Table 5.2 and the QDSSC fabricated with TiO_2/CdS(5) photoanode exhibited the highest *PCE* of (0.77 ± 0.01)% with J_{sc} of (4.54 ± 0.10) mA cm^{-2}, V_{oc} of (0.51 ± 0.01) V and *FF* of (0.34 ± 0.03).

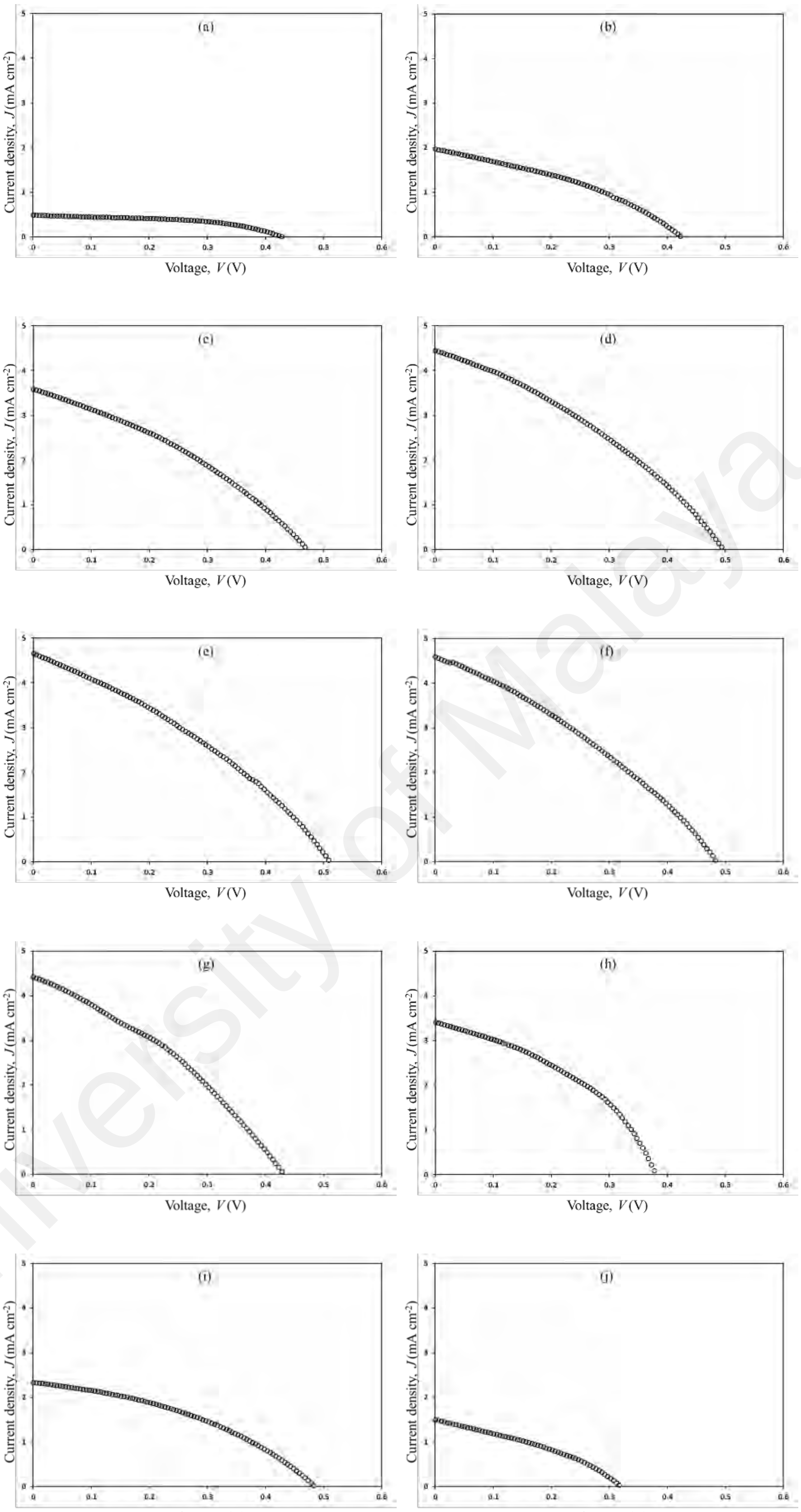

Figure 5.7: (a)–(j) show the *J–V* curves of the QDSSCs fabricated with different TiO_2/CdS photoanodes prepared with 1–10 SILAR cycles respectively.

Table 5.2: The *J–V* characterization of QDSSCs fabricated with different type of TiO$_2$/CdS photoanode which prepared with 1–10 SILAR cycles.

Photoanode used for QDSSC fabrication	J_{sc} (mA cm^{-2})	V_{oc} (V)	*FF*	*PCE* (%)
TiO$_2$/CdS(1)	0.56 ± 0.07	0.34 ± 0.08	0.49 ± 0.01	0.10 ± 0.01
TiO$_2$/CdS(2)	1.81 ± 0.30	0.42 ± 0.00	0.39 ± 0.06	0.29 ± 0.01
TiO$_2$/CdS(3)	3.41 ± 0.16	0.44 ± 0.03	0.34 ± 0.01	0.52 ± 0.05
TiO$_2$/CdS(4)	3.92 ± 0.59	0.50 ± 0.00	0.36 ± 0.01	0.70 ± 0.05
TiO$_2$/CdS(5)	4.54 ± 0.10	0.51 ± 0.01	0.34 ± 0.03	0.77 ± 0.01
TiO$_2$/CdS(6)	4.25 ± 0.29	0.50 ± 0.02	0.34 ± 0.01	0.72 ± 0.01
TiO$_2$/CdS(7)	4.24 ± 0.27	0.43 ± 0.00	0.34 ± 0.03	0.63 ± 0.01
TiO$_2$/CdS(8)	3.43 ± 0.02	0.37 ± 0.01	0.39 ± 0.01	0.49 ± 0.02
TiO$_2$/CdS(9)	2.30 ± 0.10	0.48 ± 0.03	0.39 ± 0.01	0.43 ± 0.01
TiO$_2$/CdS(10)	1.25 ± 0.44	0.35 ± 0.05	0.38 ± 0.07	0.16 ± 0.02

5.2.5 EIS Study of MC–PGPE based QDSSCs Fabricated with Different Type of TiO$_2$/CdS Photoanode (1–10 SILAR cycles)

5.2.5.1. Nyquist Plots

EIS study has been done to gain the information on the interfacial properties of the MC–PGPE based QDSSCs fabricated with different photoanode: TiO$_2$/CdS(1–10). Figure 5.8(a)–(j) show the Nyquist plots obtained from the EIS measurement of the MC–PGPE based QDSSCs fabricated with TiO$_2$/CdS(1–10) photoanodes respectively while Table 5.3 lists the interfacial properties obtained from the Nyquist plots i.e. R_s, R_{CE}, C_{CE} and R_{PA} and C_{CE}. Values of R_s, R_{CE} and R_{PA} were obtained through fitting the Nyquist plot to the equivalent circuit in Figure 3.13 using Equation (3.17) while interfacial capacitance values (i.e. C_{CE} and C_{PA}) were calculated using Equation (3.18) and (3.19) respectively. From the Nyquist plots obtained, the interfacial resistance at interface of photoanode/electrolyte or R_{PA} value increased as the number of SILAR cycles increased for the CdS deposition. The same trend can be seen with the interfacial capacitance at the interface of photoanode/electrolyte or C_{PA}. Large C_{PA} implies that high amount of charges accumulates at the interface of electrode/electrolyte. Increment of C_{PA} with increasing number of SILAR cycles is due to the amount of charges accumulated at the interface of photoanode/electrolyte increases with increased R_{PA}. This implies that the electron transfer between electrolyte/photoanode is affected by the interfacial resistance in between electrolyte and electrode or R_{PA}.

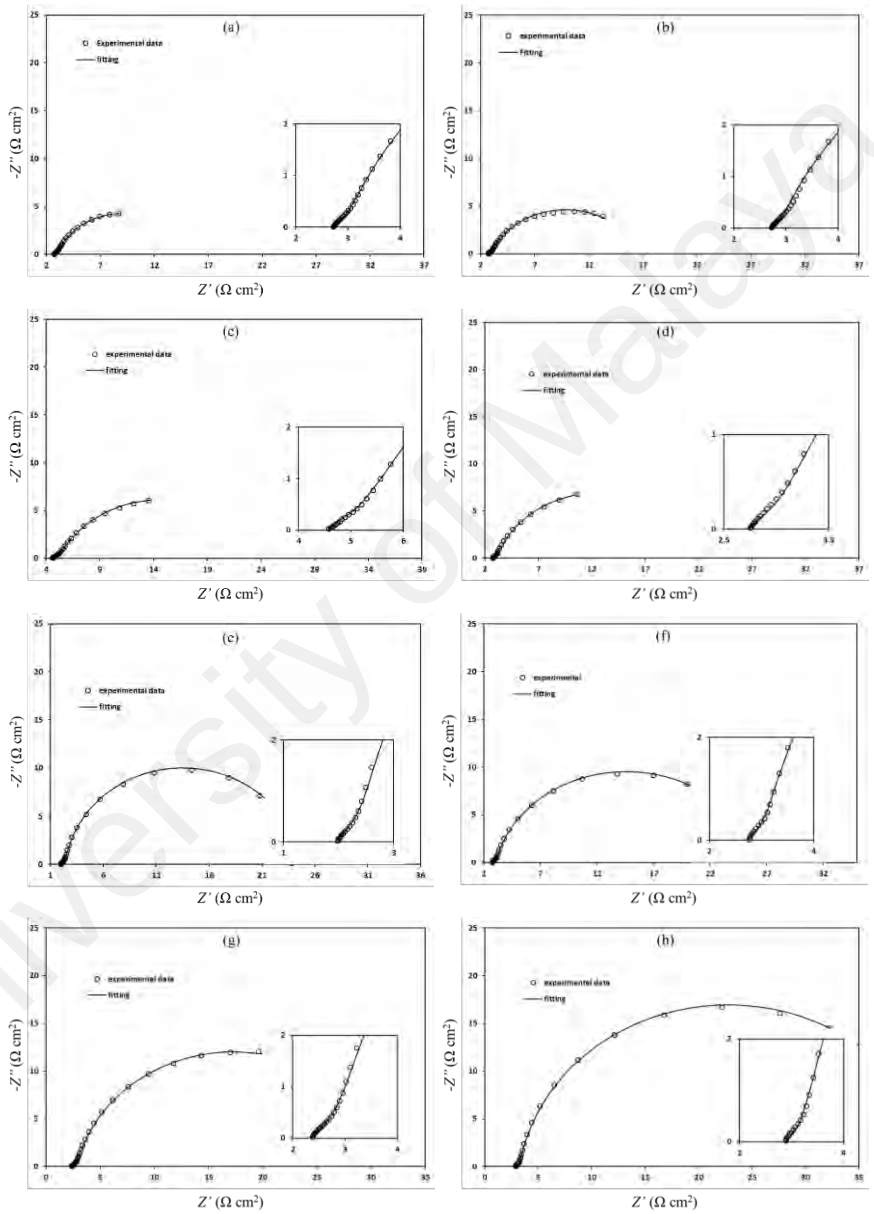

Figure 5.8: Nyquist plots obtained from EIS study of MC–PGPE QDSSCs fabricated with TiO_2/CdS(1–10) photoanodes. The inset of the figure is the semicircle correspond to the interface at the CE/electrolyte.

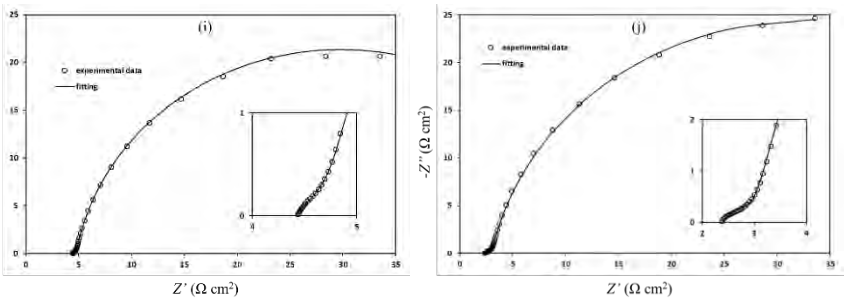

Figure 5.8, continued.

Table 5.3: The interfacial properties of the MC–PGPE based QDSSCs fabricated with TiO_2/CdS(1–10).

Photoanode	R_s (Ω cm^2)	R_{CE} (Ω cm^2)	R_{PA} (Ω cm^2)	C_{CE} (mF cm^2)	C_{PA} (mF cm^2)
TiO_2/CdS(1)	2.70 ± 0.03	0.26 ± 0.02	12.33 ± 0.58	0.60 ± 0.31	5.43 ± 0.19
TiO_2/CdS(2)	2.70 ± 0.03	0.22 ± 0.06	13.67 ± 0.58	0.59 ± 0.32	6.51 ± 1.87
TiO_2/CdS(3)	3.92 ± 0.57	0.65 ± 0.00	18.33 ± 0.58	0.85 ± 0.24	10.03 ± 1.01
TiO_2/CdS(4)	3.35 ± 1.05	0.42 ± 0.20	19.33 ± 0.28	0.74 ± 0.30	10.47 ± 1.25
TiO_2/CdS(5)	2.47 ± 0.44	0.32 ± 0.24	21.67 ± 0.57	0.63 ± 0.01	11.74 ± 2.31
TiO_2/CdS(6)	2.22 ± 0.45	0.40 ± 0.17	22.68 ± 0.56	0.73 ± 0.01	12.33 ± 2.82
TiO_2/CdS(7)	2.11 ± 0.20	0.47 ± 0.12	27.65 ± 1.15	0.76 ± 0.02	13.33 ± 1.87
TiO_2/CdS(8)	2.53 ± 0.31	0.53 ± 0.12	32.33 ± 5.77	0.81 ± 0.03	14.94 ± 0.47
TiO_2/CdS(9)	3.40 ± 0.88	0.39 ± 0.00	42.67 ± 6.35	0.71 ± 0.02	16.93 ± 1.49
TiO_2/CdS(10)	3.06 ± 1.18	0.48 ± 0.16	53.00 ± 5.20	0.80 ± 0.01	18.12 ± 0.29

5.2.5.2. Bode Plots

By utilizing Bode plot, another important parameter can be obtained i.e. electron lifetime (τ). Bode plot is a plot with phase and frequency as y and x axes respectively. Figure 5.9 shows the bode plots obtained from MC–PGPE QDSSCs fabricated with different photoanodes i.e. TiO_2/CdS(1–10). The value of τ has been calculated using the peak frequency of the Bode plot and Equation (3.18). From Table 5.4, can be seen that the τ value of the QDSSCs fabricated with TiO_2/CdS(1–5) photoanodes are higher compared to the QDSSCs fabricated with TiO_2/CdS(6–10) photoanodes.

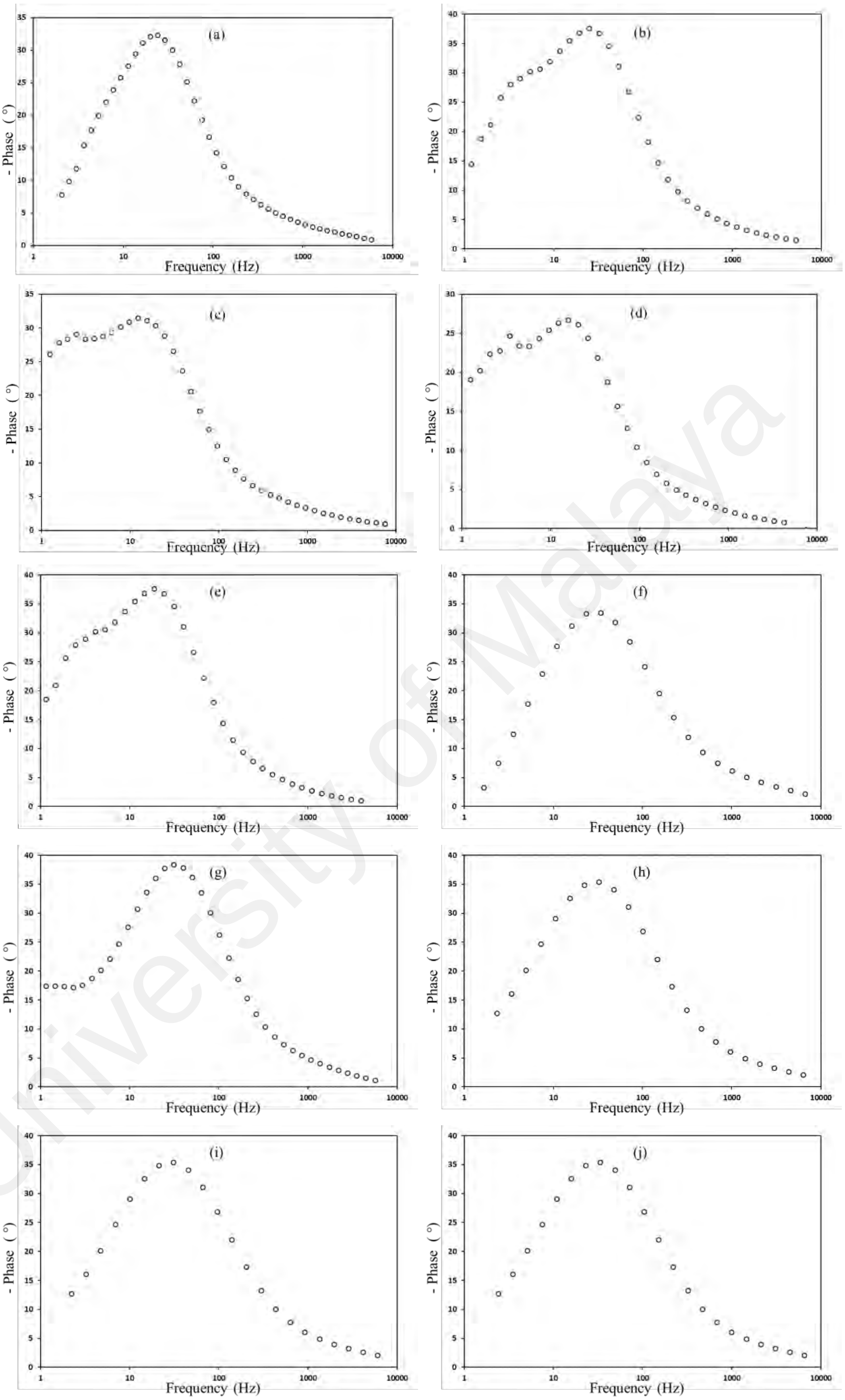

Figure 5.9: (a)–(j) show the bode plot of QDSSC fabricated with TiO_2/CdS(1) to TiO_2/CdS(10) photoanodes respectively.

Table 5.4: The electron lifetime for MC–PGPE based QDSSCs fabricated with different photoanode i.e. TiO_2/CdS(1–10) calculated from the Bode plots in Figure 5.9.

Photoanode used for QDSSCs fabrication	**Electron lifetime, τ (ms)**
TiO_2/CdS(1)	4.03 ± 0.00
TiO_2/CdS(2)	5.47 ± 2.37
TiO_2/CdS(3)	8.60 ± 0.69
TiO_2/CdS(4)	5.70 ± 0.00
TiO_2/CdS(5)	5.77 ± 0.12
TiO_2/CdS(6)	0.49 ± 0.18
TiO_2/CdS(7)	0.58 ± 0.30
TiO_2/CdS(8)	0.88 ± 0.04
TiO_2/CdS(9)	0.19 ± 0.02
TiO_2/CdS(10)	0.20 ± 0.02

5.2.6 IPCE Study of MC–PGPE Based QDSSCs Fabricated with Different Types of TiO_2/CdS Photoanode (1–10 SILAR Cycles)

Incident photon to current efficiency (IPCE) is an important characteristic of the photovoltaic devices. IPCE will enable us to determine the optimum wavelength for conversion of photon to electricity. Figure 5.10 shows the IPCE curves obtained from MC–PGPE based QDSSCs fabricated with TiO_2/CdS(1–10) photoanodes. The QDSSCs that exhibits the highest *PCE* (fabricated with TiO_2/CdS(5) photoanode) shows the highest IPCE value i.e. ~9.3% at wavelength range of 400–450 nm. In addition, the IPCE curve of this QDSSC covered a wide wavelength which is from 300 nm to 600 nm.

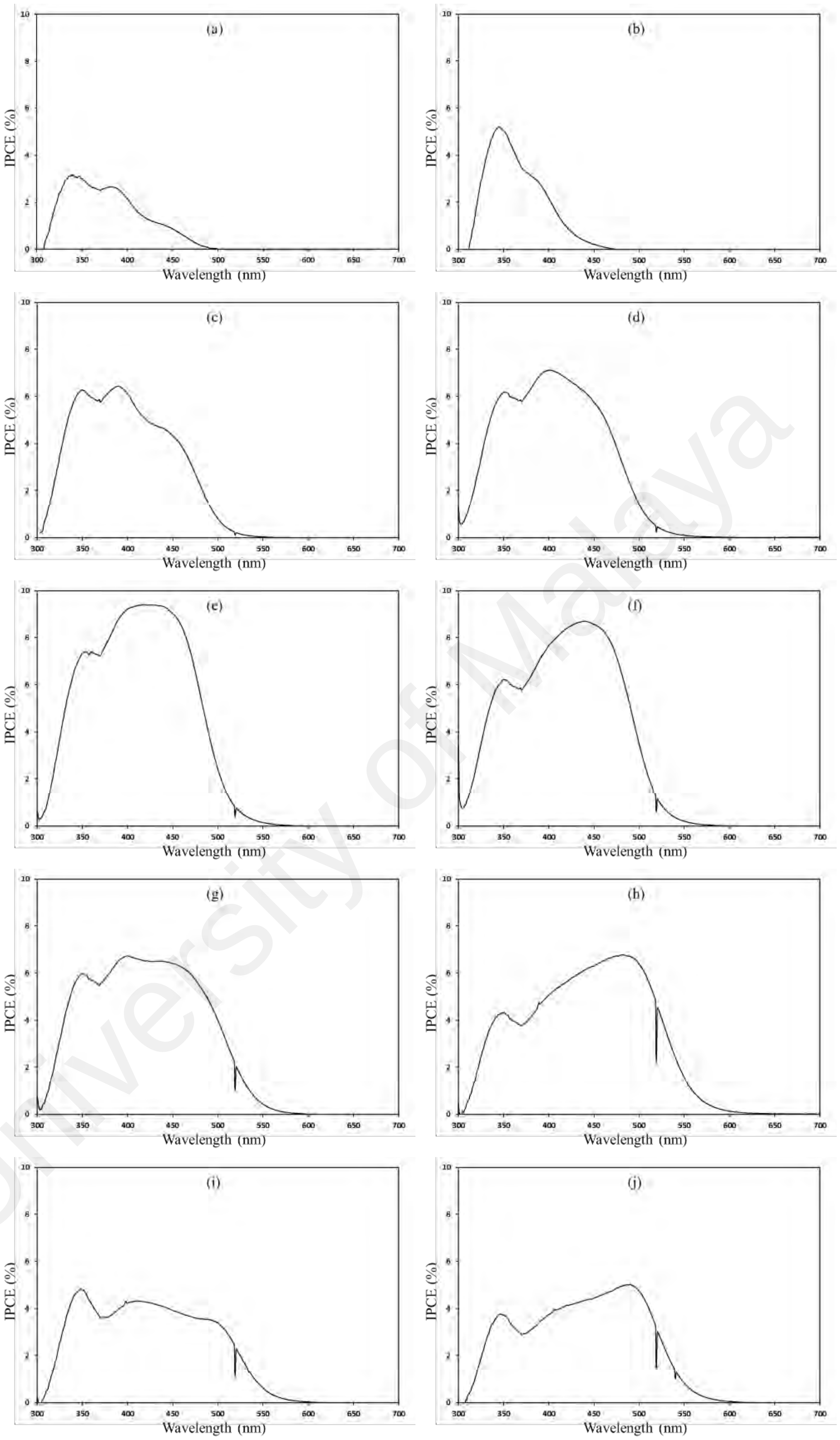

Figure 5.10: IPCE curves of the MC–PGPE based QDSSCs fabricated with TiO_2/CdS(1–10) photoanodes which represent in (a)–(j) respectively.

5.3 Improving the Performance of the MC–PGPE Based QDSSCs by Depositing Passivation Layers on the TiO_2/CdS(5) Photoanode

It has been concluded that the best number of SILAR cycles to be used for the CdS deposition is 5 SILAR cycles. QDSSCs fabricated with 5 SILAR cycles of CdS deposited photoanode i.e. TiO_2/CdS(5) exhibited the highest performance compared to the other QDSSCs fabricated. Hence, this section will present results on improving the performance of QDSSCs by depositing ZnS and SiO_2 passivation layers on TiO_2/CdS(5).

5.3.1 Morphology and Elemental Composition Study of Photoanode with Passivation Layers using FESEM and EDX Analysis

FESEM analysis has been done to study the surface morphology of the photoanode surface before and after deposition of QDs sensitizer and passivation layers. Figure 5.11(a) and (b) show FESEM images of photoanode surface with only TiO_2 layer and photoanode surface with CdS QDs sensitizer and passivation layers (ZnS and SiO_2) respectively. Referring to Figure 5.11, the surface morphology of (b) is rougher compared to (a) due to presence of CdS, ZnS and SiO_2 particles on the photoanode. However, CdS, ZnS and SiO_2 particles cannot be distinguished due to the fact that the size of these particle are extremely small compared to that of the TiO_2 (Lee & Lo, 2009).

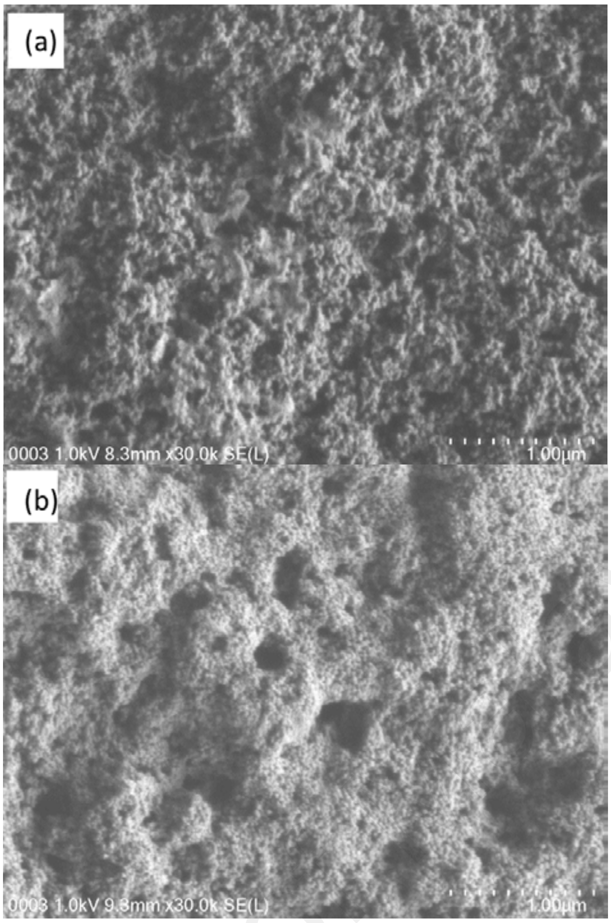

Figure 5.11: (a) photoanode surface with only TiO_2 layer (b) photoanode surface with TiO_2, CdS QDs sensitizer and passivation layers (ZnS and SiO_2) [TiO_2/CdS(5)/ZnS/SiO_2].

EDX analysis has been done to prove the presence of CdS, ZnS and SiO_2 on the TiO_2 surface in the TiO_2/CdS(5)/ZnS/SiO_2 photoanode. Figure 5.12 and Figure 5.13 show the EDX elemental map of the constituent elements and EDX spectrum obtained from the TiO_2/CdS(5)/ZnS/SiO_2 respectively. As can be seen in the EDX elemental map of the photoanode (Figure 5.12), all the elements which come from TiO_2 layers, CdS QDs sensitizer and passivation layer (ZnS and SiO_2) have been highlighted and well spread across the surface of the photoanode. The EDX spectrum (Figure 5.13) contains all elemental peaks with atomic percentage Ti (28.89%), Si (3.86%), O (65.14%), Cd (0.48%), Zn (0.80%) and S (0.82%).

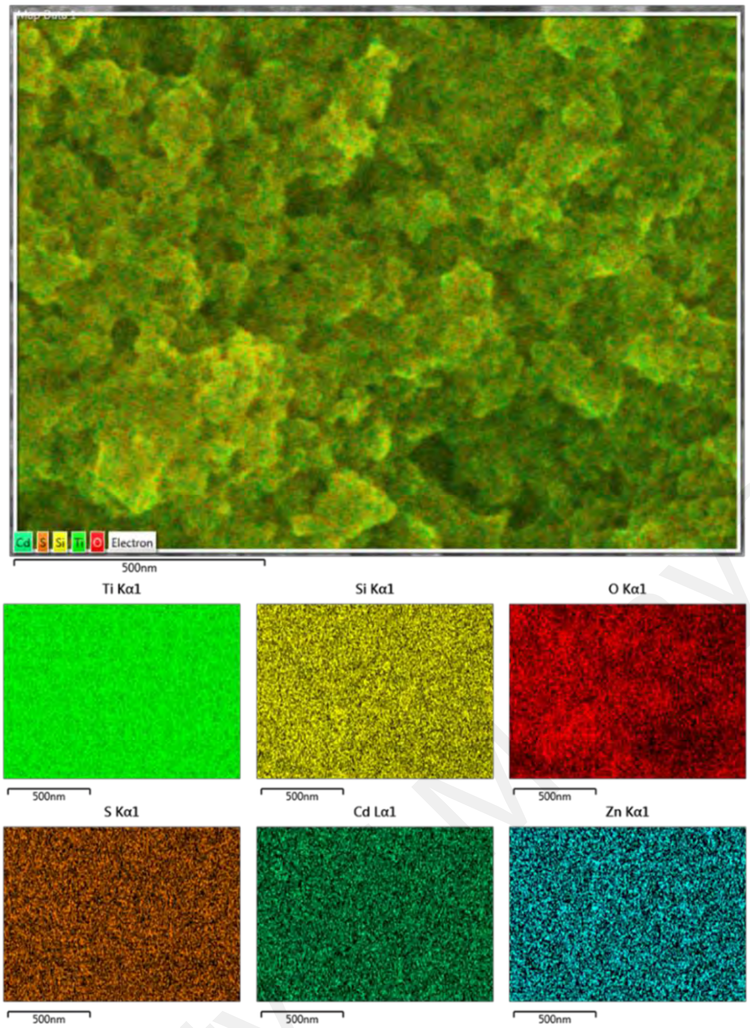

Figure 5.12: The EDX elemental map of the $TiO_2/CdS(5)/ZnS/SiO_2$ photoanode.

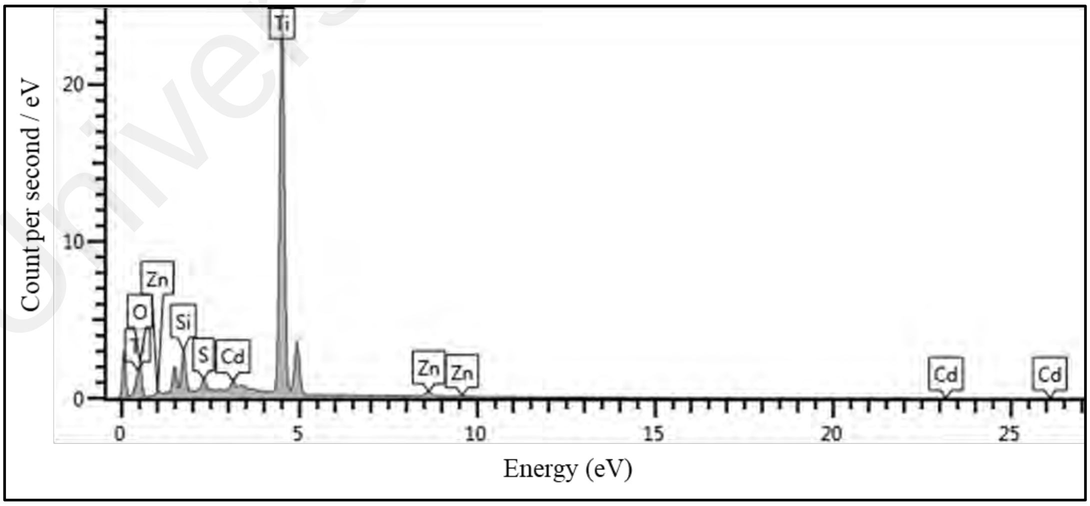

Figure 5.13: EDX spectrum of the photoanode with TiO_2 layer covered with CdS sensitizer and passivation layers (ZnS and SiO_2) i.e. $TiO_2/CdS(5)/ZnS/SiO_2$ photoanodes.

5.3.2 UV-Vis Characterization of TiO_2/CdS(5)/ZnS and TiO_2/CdS(5)/ZnS/SiO_2 Photoanodes

Figure 5.14 shows the absorption of the photoanodes with passivation layers. Figure 5.14(a) and (b) show the absorption spectrum of the TiO_2/CdS(5)/ZnS and TiO_2/CdS(5)/ZnS/SiO_2 photoanodes respectively. Figure 5.14(c) shows the combined absorption spectra of TiO_2/CdS(5), TiO_2/CdS(5)/ZnS and TiO_2/CdS(5)/ZnS/SiO_2 photoanodes for comparison. From absorption spectra in Figure 5.14(c), absorption was observed to increase with the deposition of the passivation layers: TiO_2/CdS(5) < TiO_2/CdS(5)/ZnS < TiO_2/CdS(5)/ZnS/SiO_2. In addition, blueshift of the absorption peak was observed from the absorption spectra of the photoanode with addition of the passivation layer: TiO_2/CdS(5) [511 nm] < TiO_2/CdS(5)/ZnS [503 nm] < TiO_2/CdS(5)/ZnS/SiO_2 [497 nm].

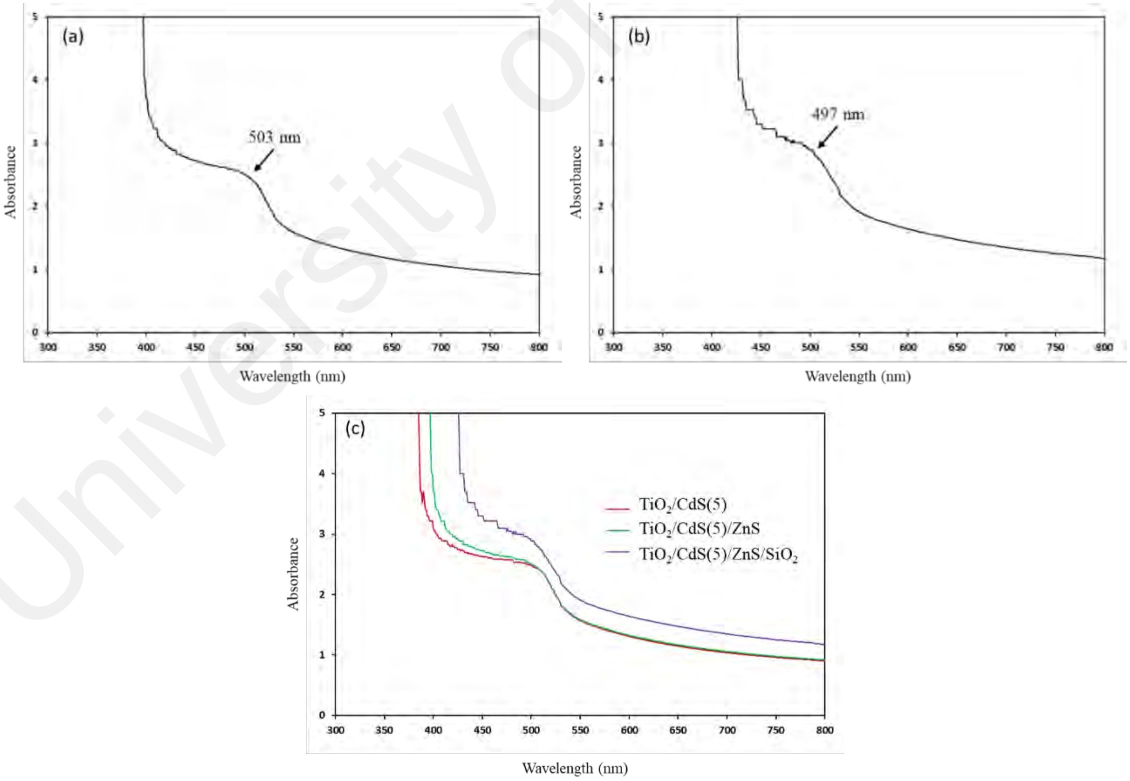

Figure 5.14: (a) and (b) show the absorption spectrum of the TiO_2/CdS(5)/ZnS and TiO_2/CdS(5)/ZnS/SiO_2 photoanodes respectively while (c) shows the combined absorption spectrum of TiO_2/CdS(5), TiO_2/CdS(5)/ZnS and TiO_2/CdS(5)/ZnS/SiO_2 photoanodes.

5.3.3 Determination of Optical Energy Transition of TiO_2/CdS(5)/ZnS and TiO_2/CdS(5)/ZnS/SiO_2 Photoanodes

By plotting graphs of $(\alpha h v)^2$ versus (hv) based on Equations (3.10) and (3.11), optical energy transition or band gap of the photoanodes deposited with passivation layers have been determined and shown in Figure 5.15 and Table 5.5 where α is absorbance (obtained from UV-vis measurement), h is Plank's constant and v is frequency. It can be seen that the absorption peak has undergone blueshift as passivation layers was deposited while E_g decreased with deposition of passivation layers.

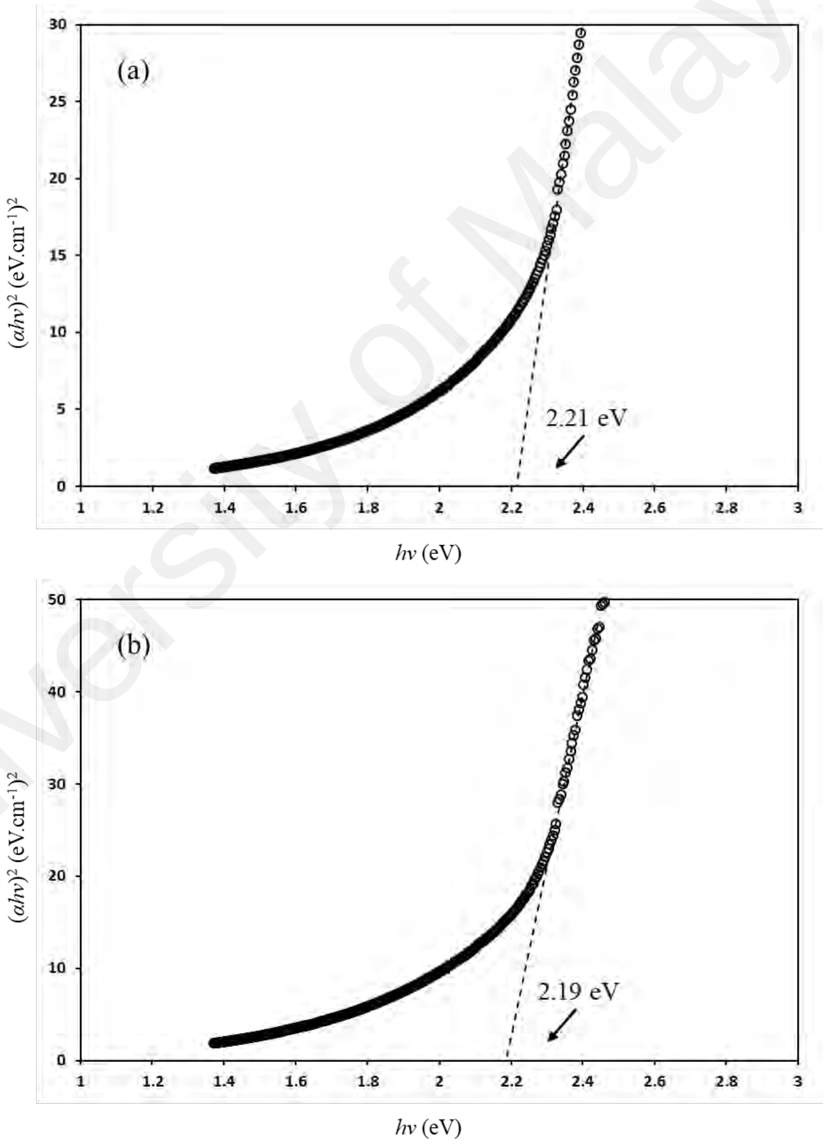

Figure 5.15: Tauc plot of TiO_2/CdS(5)/ZnS and TiO_2/CdS(5)/ZnS/SiO_2 photoanodes in (a) and (b) respectively.

Table 5.5: The absorption peak and optical energy band gap of the TiO_2/CdS(5), TiO_2/CdS(5)/ZnS and TiO_2/CdS(5)/ZnS/SiO_2 photoanodes.

Photoanodes	Absorption peak (nm)	Band gap (eV)
TiO_2/CdS(5)	511	2.22
TiO_2/CdS(5)/ZnS	503	2.21
TiO_2/CdS(5)/ZnS/SiO_2	497	2.19

5.3.4 *J–V* Characterization of MC–PGPE Based QDSSCs Fabricated with TiO_2/CdS(5)/ZnS and TiO_2/CdS(5)/ZnS/SiO_2 Photoanodes

J–V characterization has been done to study the effect of the passivation layers to the performance of the QDSSCs. The electrolyte used in this part is the optimized MC–PGPE and the CE material used is Pt. Figure 5.16(a) and (b) show the *J–V* curves obtained from the optimized MC–PGPE based QDSSCs fabricated with TiO_2/CdS(5)/ZnS and TiO_2/CdS(5)/ZnS/SiO_2 photoanodes respectively. Table 5.6 summarizes the *J–V* parameters obtained. QDSSC fabricated with TiO_2/CdS(5)/ZnS photoanode showed *PCE* improvement of ~35% compared to the QDSSC without passivation layer. The performance of the QDSSC are further improved by addition of SiO_2 layer which resulted in *PCE* improved by ~57 % compared to the QDSSC without passivation layer.

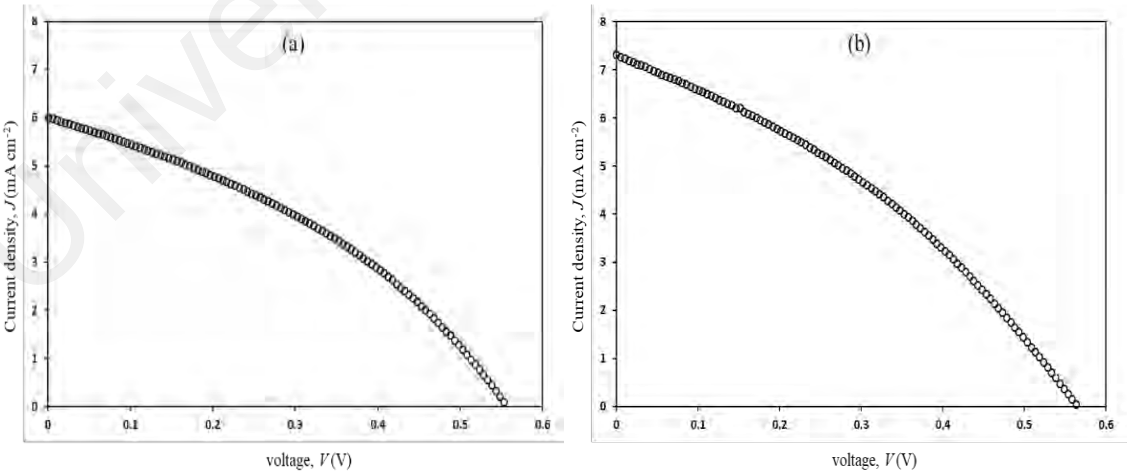

Figure 5.16: *J–V* curves of the QDSSCs fabricated with different passivation layers. (a) is for TiO_2/CdS(5)/ZnS photoanode while (b) is for TiO_2/CdS(5)/ZnS/SiO_2 photoanode.

Table 5.6: The *J–V* parameters obtained from Figure 5.16.

Photoanode used for QDSSC fabrication	J_{sc} **(mA cm^{-2})**	V_{oc} **(V)**	***FF***	***PCE*** **(%)**
TiO_2/CdS(5)	4.54 ± 0.10	0.51 ± 0.01	0.34 ± 0.03	0.77 ± 0.01
TiO_2/CdS(5)/ZnS	5.93 ± 0.12	0.55 ± 0.01	0.36 ± 0.01	1.19 ± 0.04
TiO_2/CdS(5)/ZnS/SiO_2	7.09 ± 0.27	0.56 ± 0.04	0.34 ± 0.01	1.34 ± 0.13

5.3.5 EIS Study of MC–PGPE Based QDSSCs Fabricated with TiO_2/CdS(5)/ZnS and TiO_2/CdS(5)/ZnS/SiO_2 Photoanodes

5.3.5.1 Nyquist Plots

Figure 5.17(a) and (b) show the Nyquist plots of the MC–PGPE based QDSSCs fabricated with TiO_2/CdS(5)/ZnS and TiO_2/CdS(5)/ZnS/SiO_2 photoanodes respectively. Values of R_s, R_{CE} and R_{PA} were obtained through fitting the Nyquist plot to the equivalent circuit in Figure 3.13 using Equation (3.17) while interfacial capacitance values (i.e. C_{CE} and C_{PA}) were calculated using Equation (3.18) and (3.19) respectively. Table 5.7 lists the interfacial properties of the QDSSCs obtained from the Nyquist plot. From EIS measurements, there is improvement of the R_{PA} parameter with addition of ZnS passivation layer from (21.67 ± 0.57) Ω cm^2 to (30.31 ± 2.27) Ω cm^2. The R_{PA} was further improved with addition of another passivation layer i.e. SiO_2 layer form (30.31 ± 2.27) Ω cm^2 to (40.33 ± 1.15) Ω cm^2. The same trend can be seen with C_{PA} parameter of the QDSSCs which increased with addition of passivation layer and implied that the amount of charges accumulated at interface of photoanode/electrolyte increased with increasing R_{PA}. R_s of all QDSSCs are in the same range 2.22–2.52 Ω cm^2.

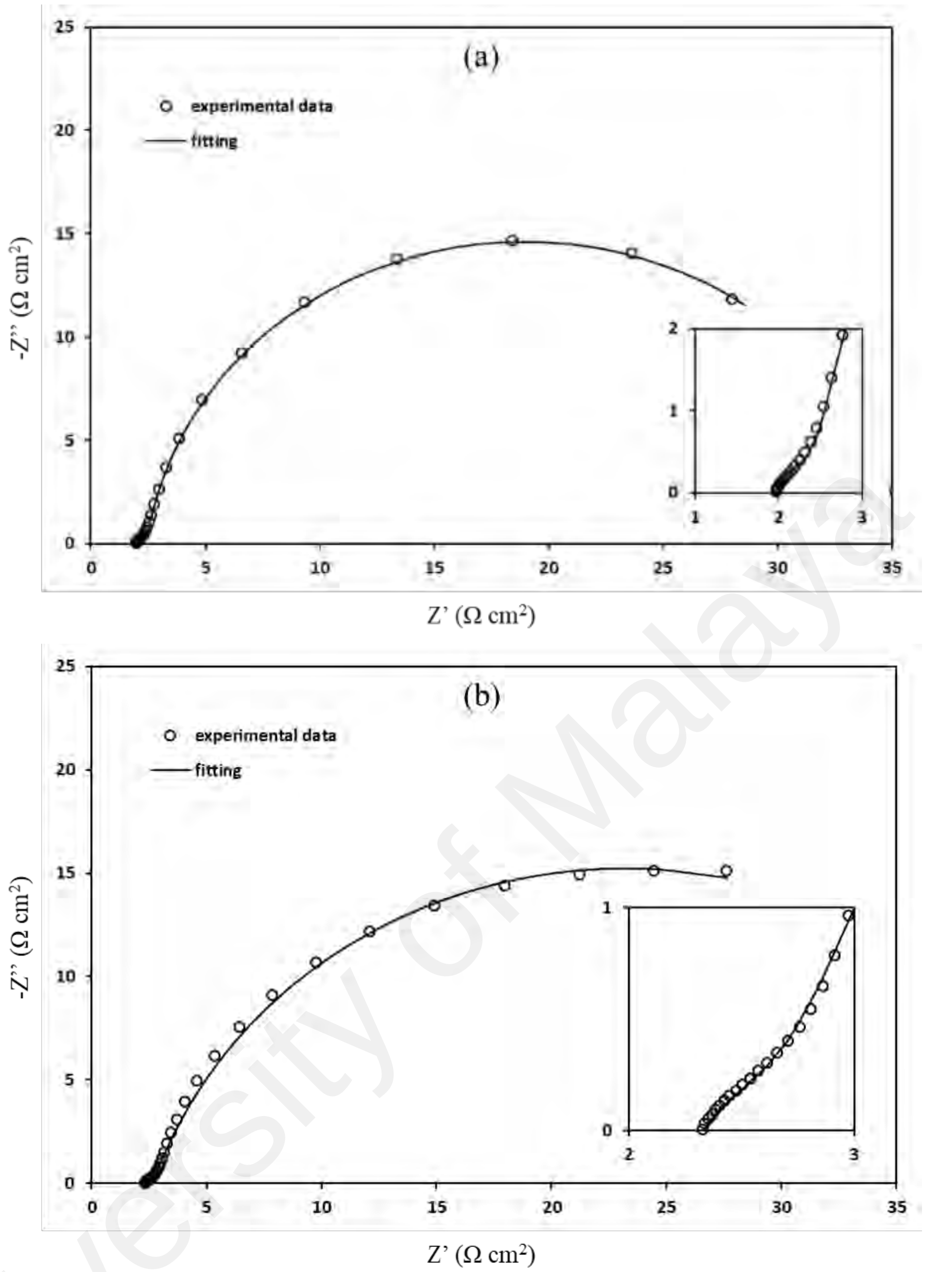

Figure 5.17: (a) and (b) show the Nyquist plots of QDSSCs fabricated with TiO_2/CdS(5)/ZnS and TiO_2/CdS(5)/ZnS/SiO_2 photoanodes respectively.

Table 5.7: The interfacial properties obtained from Figure 5.17.

Photoanode	R_s **(Ω cm²)**	R_{CE} **(Ω cm²)**	R_{PA} **(Ω cm²)**	C_{CE} **(mF cm²)**	C_{PA} **(mF cm²)**
TiO_2/CdS(5)	2.47 ± 0.44	0.32 ± 0.24	21.67 ± 0.57	0.63 ± 0.01	11.74 ± 2.31
TiO_2/CdS(5)/ZnS	2.22 ± 0.22	0.57 ± 0.05	30.31 ± 2.27	0.84 ± 0.02	12.65 ± 3.04
TiO_2/CdS(2)/ZnS/SiO_2	2.52 ± 0.32	0.42 ± 0.02	40.33 ± 1.15	0.65 ± 0.36	13.33 ± 0.13

5.3.5.2 Bode Plots

Electron lifetime (τ) of the QDSSCs have been estimated using Bode plot. The value of τ has been calculated using the peak frequency of the Bode plot and Equation (3.18). Figure 5.18 shows the Bode plots obtained from MC–PGPE QDSSCs fabricated with TiO_2/CdS(5)/ZnS and TiO_2/CdS(5)/ZnS/SiO_2 photoanodes. From Table 5.8, it can be seen that the QDSSC fabricated with TiO_2/CdS(5)/ZnS photoanode possessed τ of (6.90 ± 0.98) ms while QDSSC fabricated with TiO_2/CdS(5)/ZnS/SiO_2 photoanode is (12.43 ± 0.12) ms. Hence, QDSSCs fabricated with passivation layers exhibited longer τ compared to the QDSSC fabricated with no passivation layers i.e. (5.77 ± 0.12) ms.

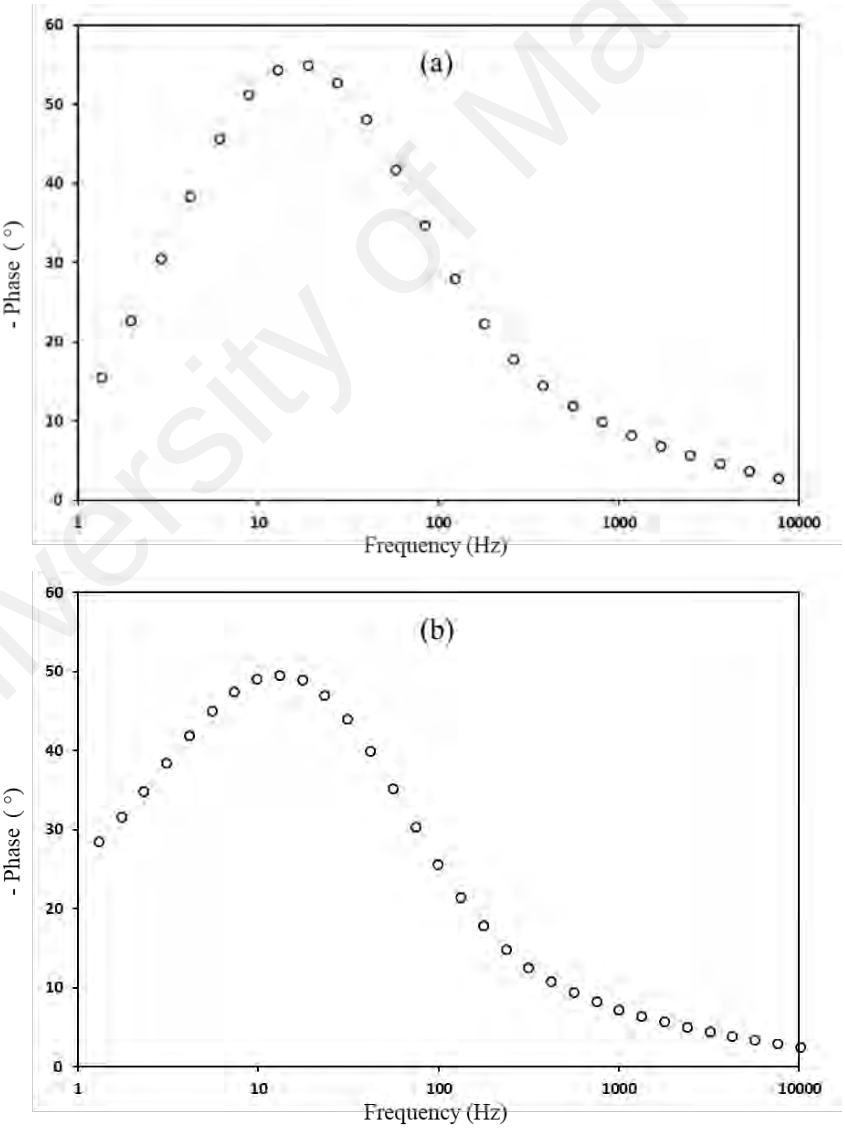

Figure 5.18: (a) and (b) show the Bode plots of the QDSSCs fabricated with TiO_2/CdS(5)/ZnS and TiO_2/CdS(5)/ZnS/SiO_2 photoanodes respectively.

Table 5.8: The τ for the QDSSCs fabricated with TiO_2/CdS(5)/ZnS and TiO_2/CdS(5)/ZnS/SiO_2 photoanodes calculated from the bode plots.

Photoanode used for QDSSCs fabrication	**Electron lifetime, τ (ms)**
TiO_2/CdS(5)	5.77 ± 0.12
TiO_2/CdS(5)/ZnS	6.90 ± 0.98
TiO_2/CdS(5)/ZnS/SiO_2	12.43 ± 0.12

5.3.6 IPCE Study of MC–PGPE Based QDSSCs Fabricated with TiO_2/CdS(5)/ZnS and TiO_2/CdS(5)/ZnS/SiO_2 Photoanodes

Figure 5.19 shows the IPCE curves obtained from MC–PGPE based QDSSCs fabricated with different photoanodes i.e. TiO_2/CdS(5)/ZnS and TiO_2/CdS(5)/ZnS/SiO_2 photoanodes. The highest IPCE obtained from QDSSC with TiO_2/CdS(5)/ZnS is 57.24 % at wavelength 407 nm. QDSSC fabricated with TiO_2/CdS(5)/ZnS/SiO_2 photoanode exhibited the highest IPCE of 67.20% at wavelength 403 nm. IPCE curve of both QDSSCs covered the wavelength from 300–600 nm. QDSSCs fabricated with passivation layers exhibited higher IPCE compared to the QDSSC with no passivation layers (TiO_2/CdS(5) photoanode) i.e. 9.3%.

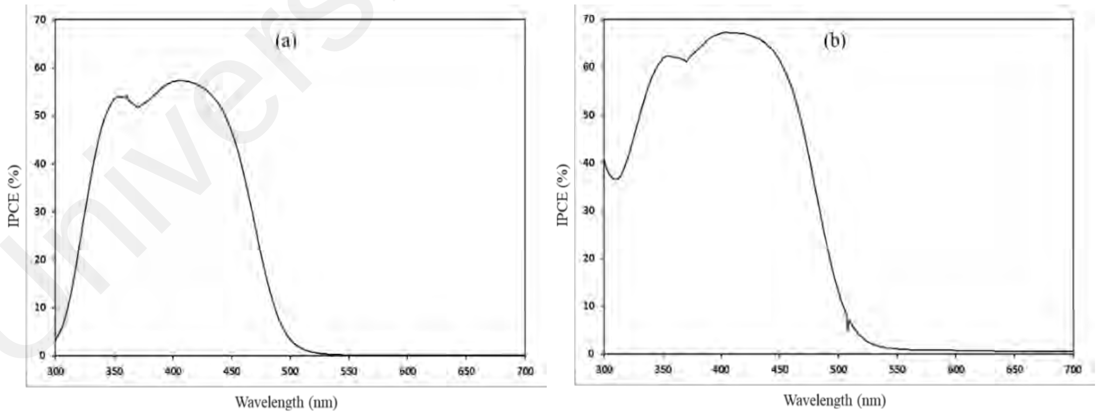

Figure 5.19: (a) and (b) are IPCE curves of MC–PGPE based QDSSCs fabricated with TiO_2/CdS(5)/ZnS and TiO_2/CdS(5)/ZnS/SiO_2 photoanodes respectively.

5.4 Summary

- From UV-Vis absorption, photoanodes with CdS QDs show higher absorption compared to the photoanode with only TiO_2 layers. However, there is no absorption observed at the range of 380 nm to 540 nm by photoanodes deposited with CdS QDs using 6 to 10 SILAR cycles i.e. TiO_2/CdS(6-10) photoanodes.
- From adsorption spectrum of TiO_2/CdS(1) to TiO_2/CdS(5) photoanodes, the energy band gap of the TiO_2/CdS photoanode decreased with increasing of number of SILAR cycles.
- From adsorption spectrum of TiO_2/CdS(6) to TiO_2/CdS(10) photoanode, the energy band gap of the TiO_2/CdS photoanode is almost constant with increasing of number of SILAR cycles.
- QDSSC is fabricated with TiO_2/CdS(5) photoanode exhibited the highest *PCE* of (0.77 ± 0.01)% with J_{sc} of (4.54 ± 0.10) mA cm^{-2}, V_{oc} of (0.51 ± 0.01) V and *FF* of (0.34 ± 0.03).
- From the Nyquist plots obtained for QDSSCs, the R_{PA} value increased as the number of SILAR cycles increased for the CdS deposition.
- The τ value of the QDSSCs fabricated with TiO_2/CdS(1–5) photoanodes are higher compared to the QDSSCs fabricated with TiO_2/CdS(6–10) photoanodes.
- The QDSSC that exhibited the highest *PCE* (fabricated with TiO_2/CdS(5) photoanode) shows the highest IPCE value i.e. ~9.3% at wavelength range of 400–450 nm.
- From UV-Vis absorption spectra, the absorption of the photoanode increased with the deposition of the passivation layers: TiO_2/CdS(5) < TiO_2/CdS(5)/ZnS < TiO_2/CdS(5)/ZnS/SiO_2.
- QDSSC fabricated with TiO_2/CdS(5)/ZnS photoanode showed *PCE* improvement of ~35% compared to the QDSSC without passivation layer.

- The performance of the QDSSC was further improved by addition of SiO_2 layer which resulted in *PCE* improvement of ~57 % compared to the QDSSC without passivation layer.
- From EIS measurements of the QDSSCs, there is improvement of the R_{PA} parameter with addition of ZnS passivation layer from $(21.67 \pm 0.57)\ \Omega\ cm^2$ to $(30.31 \pm 2.27)\ \Omega\ cm^2$.
- The R_{PA} was further improved with addition of another passivation layer i.e. SiO_2 layer form $(30.31 \pm 2.27)\ \Omega\ cm^2$ to $(40.33 \pm 1.15)\ \Omega\ cm^2$.
- QDSSCs fabricated with passivation layers exhibited longer τ compared to the QDSSC fabricated with no passivation layers.
- QDSSCs fabricated with passivation layers exhibited large IPCE compared to the QDSSC with no passivation layers.

CHAPTER 6: RESULTS ON COUNTER ELECTRODE MATERIALS

6.1 Introduction

The last part of this work is to investigate the most suitable material to be used as counter electrode (CE) for the QDSSCs fabrication i.e. the third objective of this work. This chapter will show the results obtained from experiments carried out to achieve the third objective. The materials that have been chosen for the CE investigation is Au and PbS. Au is chosen as it has quite the same properties with Pt being in the same noble metal group. PbS can generate auxiliary tandem effect that enhance the QDSSC performance. The fabrication of the QDSSC will utilize the optimized methylcellulose–polysulphide gel polymer electrolyte (MC–PGPE) (sample E) and TiO_2/CdS(5)/ZnS/SiO_2 photoanode. Through this chapter, the morphology and elemental composition of the CE have been investigated using FESEM and EDX while the electrochemical properties of the CE have been investigated using EIS and Tafel polarization measurements on the symmetric dummy cells. This will be followed by fabrication and characterizations of QDSSC with different CE materials through *J*–*V*, EIS and IPCE analysis.

6.2 Morphology and Elemental Composition Study of CEs using FESEM and EDX Analysis

6.2.1 FESEM Images of the Pt, Au and PbS CE Surface

FESEM analysis have been done to study the surface morphology of the CE with different selected materials which are Pt, Au and PbS. Figure 6.1 shows the FESEM images obtained from the experiment. All three surfaces of CE are uneven as observed from the FESEM images which show a good surface property for the catalytic electrode. The surface roughness with small pore diameter around 54 nm was observed for Pt CE. Island like structure with different shapes and sizes can be observed for the Au CE. The surface morphology of PbS in this work is similar to the work done by Tachan et. al 2011 and the size of the PbS crystals observed is less than 10^{-6} m. As can be seen from the figure, the surface of PbS CE is rougher compared to Au and Pt CE. This condition provides higher surface area for better catalytic activities. Hence the rate of charge transfer from PbS CE to the S_x^{2-} ions in electrolyte should be faster.

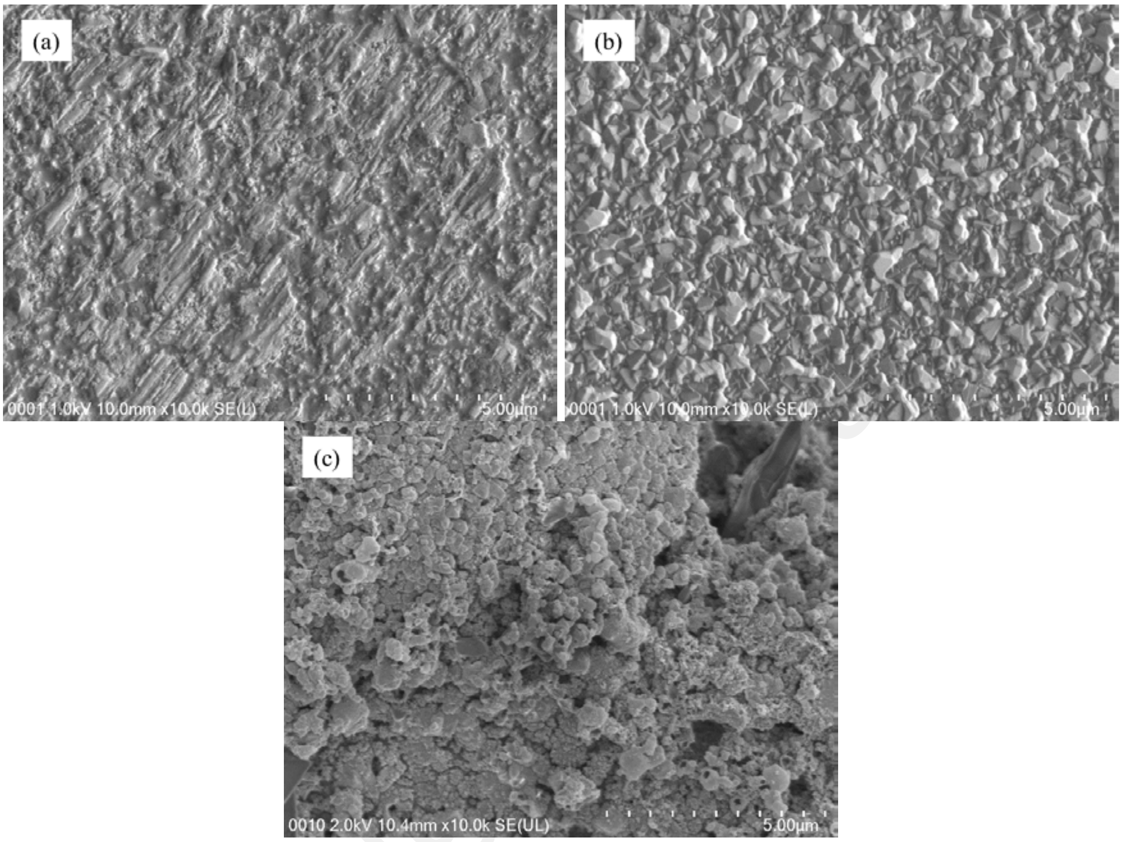

Figure 6.1: (a), (b) and (c) show the FESEM images of Pt, Au and PbS CE surfaces respectively.

6.2.2 Elemental Composition Analysis of the Pt, Au and PbS CEs

EDX analysis has been done to study the elemental composition of the CEs and to prove the presence of the constituent material on the CEs.

Figure 6.2 shows the EDX spectra obtained from the Pt, Au and Pb CE surfaces. From the EDX spectrum of the Pt CE, there is a peak of Pt, Sn and O with the atomic percentages of the constituent elements: Pt (16.85%), Sn (26.78%), and O (56.37%). The existence of Sn and O peaks in the EDX spectrum is derived from the FTO glass substrate used. There is a peak of Au, Sn and O in the Au CE EDX spectrum with atomic percentages of the constituent elements: Au (40.77%), Sn (22.51%) and O (36.71%).

Lastly, from the EDX spectrum of the PbS CE, there is a peak of Pb, S and O appeared with the atomic percentages of the constituent elements: Pb (34.64%), S (10.24%) and O (55.12%). It is implied that the O peak in the PbS CE EDX spectrum is due to the oxide layer formed at the surface of Pb foil. Pb metal can easily oxidise under atmospheric conditions.

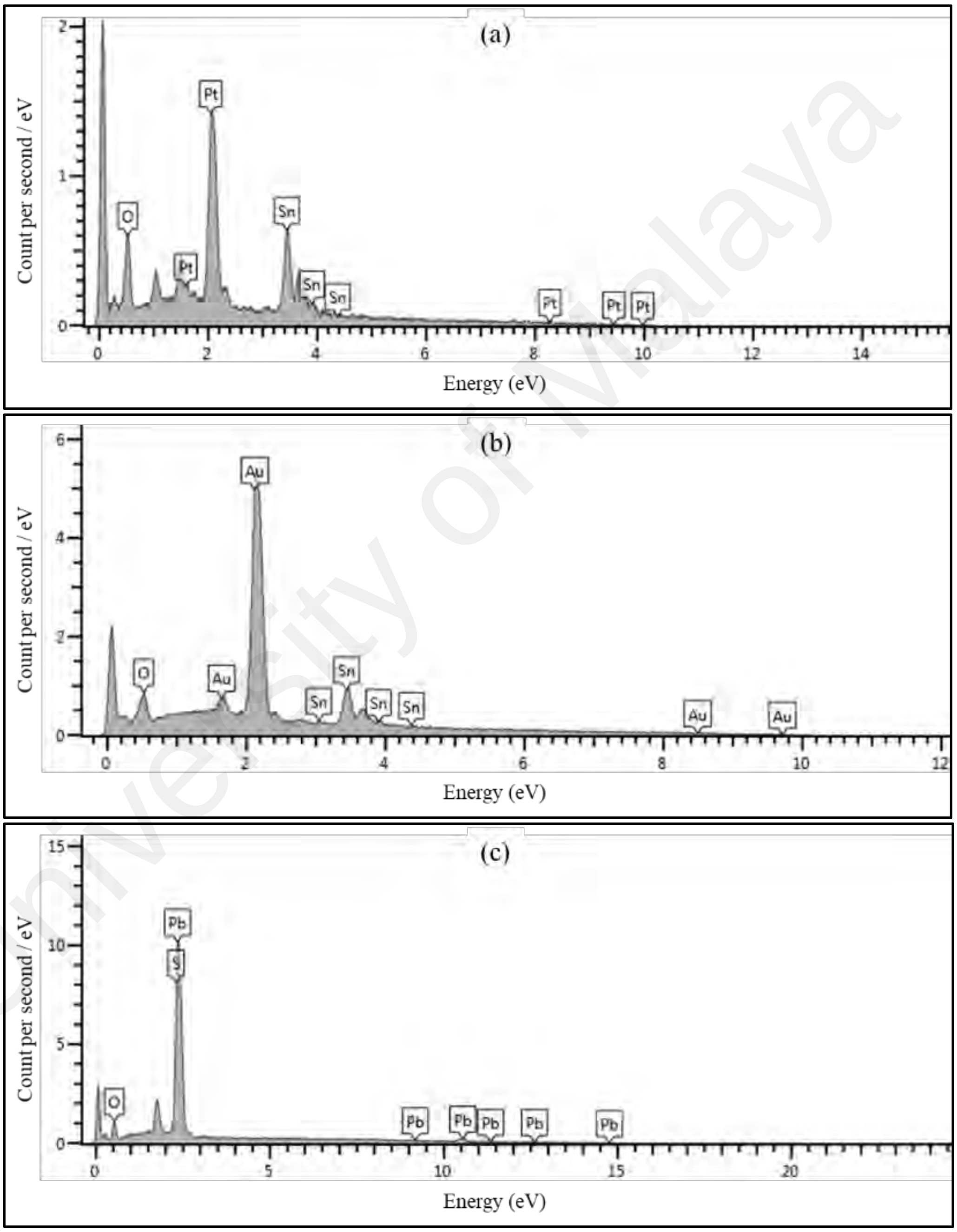

Figure 6.2: (a), (b) and (c) show the EDX spectrum obtained from Pt, Au and PbS CE surfaces respectively.

6.3 Charge Transfer Study of Pt, Au and PbS CEs Using EIS Analysis of the Symmetrical Cells

The properties of charge transfer between CE/electrolyte can be studied using EIS. The symmetrical cell is fabricated with Pt, Au or PbS electrodes separated by the thin film electrolyte. The electrolyte used is the optimized MC–PGPE (sample E). Figure 6.3 shows the Nyquist plots and Table 6.1 lists the interfacial properties from the respective symmetrical dummy cells fabricated with Pt, Au and PbS electrodes. Values of R_s and R_{dc} were obtained through fitting the Nyquist to the equivalent circuit in Figure 3.10 using Equation (3.14), while interfacial capacitance (C_{dc}) value was calculated using Equation (3.19). The R_s value is highest for the cell with Au CE followed by Pt and PbS. R_{dc} also exhibited the same trend. The C_{dc} of the Au symmetrical cell was the highest and followed by Pt and PbS symmetrical cells. This is due to the increased amount of charges accumulated at interface of the photoanode/electrolyte with increasing interfacial resistance.

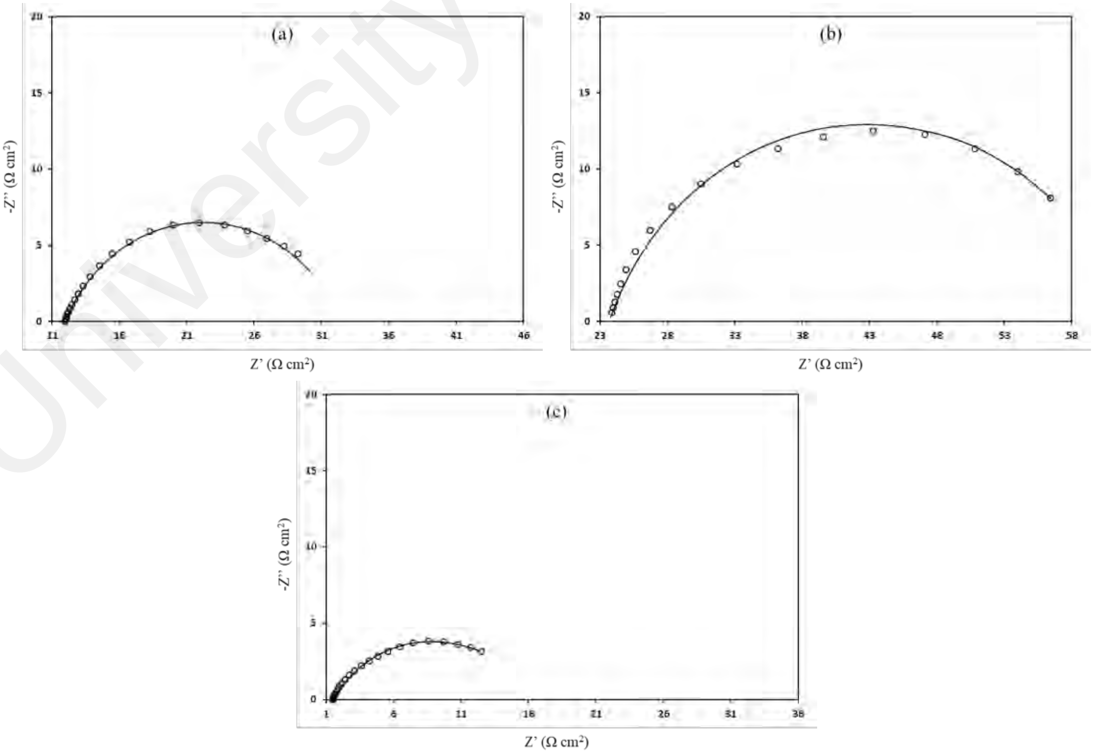

Figure 6.3: (a), (b) and (c) show the Nyquist plots obtained from the EIS analysis of Pt, Au and PbS symmetrical cells respectively to study the charge transfer process.

Table 6.1: The charge transfer properties obtained from the Pt, Au and PbS symmetrical cells obtained from EIS analysis.

Symmetrical electrode	R_S **(Ω cm^2)**	R_{dc} **(Ω cm^2)**	C_{dc} **(F cm^2)**
Pt	12.28 ± 0.90	5.07 ± 0.19	0.026 ± 0.008
Au	23.64 ± 1.22	8.59 ± 1.26	0.064 ± 0.030
PbS	1.88 ± 0.72	3.00 ± 0.25	0.016 ± 0.002

6.4 Tafel Polarization Measurement of Au and PbS CEs Using LSV Analysis of the Symmetrical cells

LSV test from potential of -0.6 V to 0.6 V has been done on the Au and PbS symmetric dummy cells to study the electrocatalytic activity of the target CE toward the MC–PGPE (sample E). It is noted that Tafel measurements on Pt CE has been done in the previous chapter (Section 4.3). From both LSV curves, the current density attained saturation at above 0.3 V for both polarities. In addition, the equilibrium steady state conditions can be seen as the anodic and cathodic part of the LSV curves are quite similar.

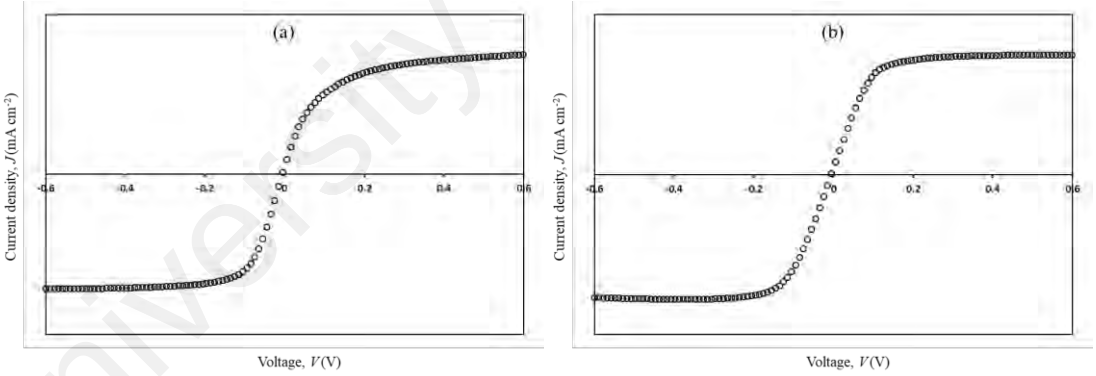

Figure 6.4: (a) and (b) show the LSV curves of Au and PbS symmetric dummy cells respectively.

From LSV curves, the Tafel polarization curves of the Au and PbS have been plotted by absolute and logarithmic current density values as shown in Figure 6.5. The diffusion of the polysulphide ions ($D_{S_x^{2-}}$) and charge transfer resistance in between CE/electrolyte (R_{dc}) can be calculated from J_{lim} and J_o obtained from the plotted Tafel polarization curve using Equation (3.10) and (3.11) respectively.

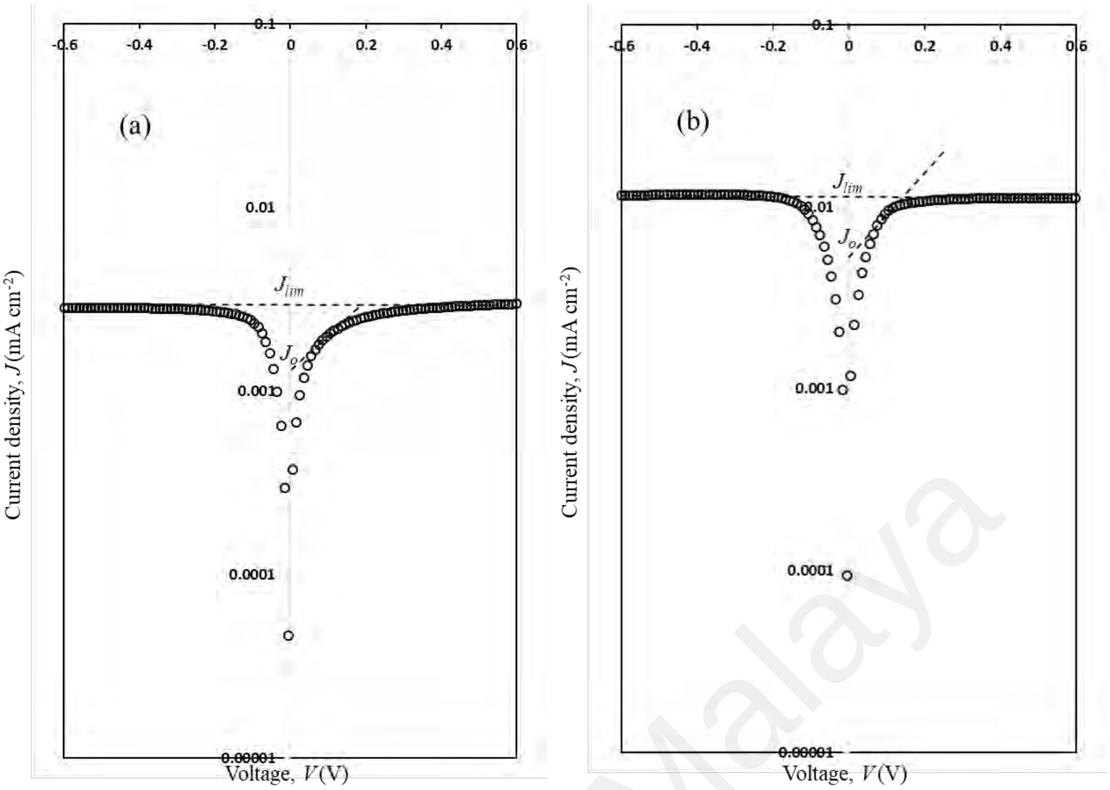

Figure 6.5: (a) and (b) show the Tafel polarization curves of Au and PbS symmetric dummy cells respectively.

Table 6.2: The parameters obtained from the Tafel polarization measurement of Pt, Au and PbS symmetric dummy cells respectively.

Symmetrical electrode	J_{lim} (mA cm^{-2})	J_o (mA cm^{-2})	$D_{S_x^{2-}}$ (x 10^{-6} cm^2 s^{-1})	R_{dc} (Ω cm^2)
Pt	3.54 ± 0.03	2.27 ± 0.06	1.08 ± 0.01	5.67 ± 0.15
Au	2.98 ± 0.19	1.57 ± 0.31	0.97 ± 0.06	8.39 ± 1.57
PbS	10.73 ± 0.81	4.33 ± 0.91	3.27 ± 0.25	3.05 ± 0.62

The parameters obtained from Tafel polarization measurement such as J_{lim}, J_o, $D_{S_x^{2-}}$ and R_{dc} are summarized in Table 6.2. The highest J_{lim} and J_o were possessed by PbS symmetric cell, which were followed by Pt and Au symmetric cells. The highest $D_{S_x^{2-}}$ shown by PbS symmetric cell was followed by Pt and Au symmetric cells. The lowest R_{dc} possessed by PbS symmetric cell was followed by Pt and Au symmetric cells. PbS is the most catalytic CE towards MC–PGPE since it exhibited highest $D_{S_x^{2-}}$ and lowest R_{dc}.

6.5 J–V Characterization of MC–PGPE Based QDSSCs Fabricated with Au and PbS CEs

J–V characterization has been done with QDSSCs fabricated with different CEs. It is noted that the electrolyte used in the fabrication of the QDSSCs is the MC–PGPE that has been optimized in the previous section (sample E) and the photoanode used is TiO_2/CdS(5)/ZnS/SiO_2. Figure 6.6 and Table 6.3 show the J–V curves and J–V characteristics obtained from this experiment respectively. Compared to the QDSSC fabricated with Pt, the *PCE* of Au QDSSC is slightly lower with percentage difference of 5.22%. The lower *PCE* value of QDSSC fabricated with Au is due to the lower value of J_{sc} and V_{oc} compared to the Pt QDSSC. QDSSC fabricated with PbS exhibited excellent performance with *PCE* improvement of 111.19% compared to the Pt QDSSC. The higher *PCE* value resulted from the higher J_{sc}, V_{oc} and *FF* parameters value.

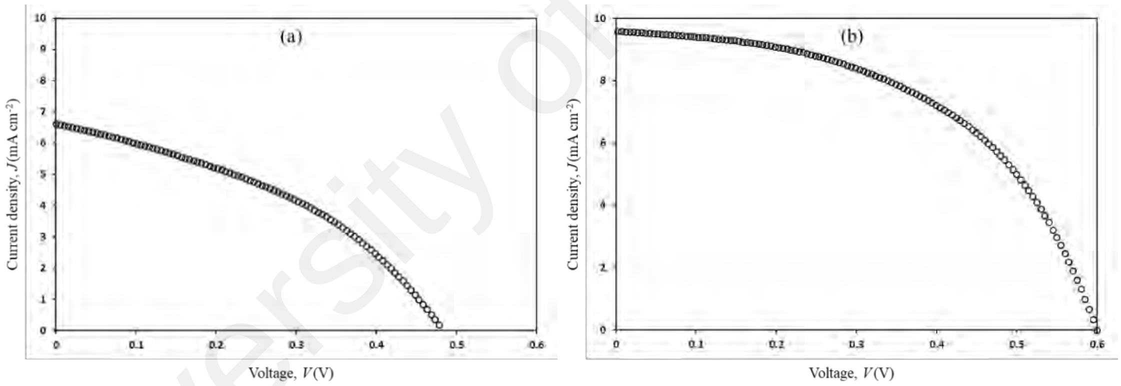

Figure 6.6: (a) and (b) show the J–V curves obtained from MC–PGPE based QDSSCs fabricated with Au and PbS CEs respectively.

Table 6.3: The J–V characteristic parameters obtained from Figure 6.6.

Counter electrode	J_{sc} (mA cm^{-2})	V_{oc} (V)	*FF*	*PCE* (%)
Pt	7.09 ± 0.27	0.56 ± 0.04	0.34 ± 0.01	1.34 ± 0.13
Au	6.59 ± 0.14	0.50 ± 0.03	0.37 ± 0.03	1.27 ± 0.06
PbS	9.54 ± 0.16	0.60 ± 0.02	0.49 ± 0.03	2.83 ± 0.07

6.6 Interfacial Study of MC–PGPE Based QDSSCs Fabricated with Different CE Materials using EIS

6.6.1 Nyquist Plots

EIS study has been done to gain the information on the interfacial properties of the MC–PGPE based QDSSCs fabricated with different CE i.e. Au and PbS. Figure 6.7 shows the Nyquist plots obtained from the EIS measurement of the MC–PGPE based QDSSCs fabricated with Au and PbS. Values of R_s, R_{CE} and R_{PA} were obtained through fitting the Nyquist plot to the equivalent circuit in Figure 3.13 using Equation (3.17), while interfacial capacitance values (i.e. C_{CE} and C_{PA}) were calculated using Equations (3.18) and (3.19) respectively. Table 6.4 lists the parameters obtained from the Nyquist plot. The Au QDSSC possessed the highest interfacial resistance in between CE/electrolyte interface or R_{CE} of (0.59 ± 0.08) Ω cm^2 followed by Pt QDSSC with R_{CE} of (0.42 ± 0.02) Ω cm^2 and PbS QDSSC with R_{CE} of (0.34 ± 0.09) Ω cm^2. The same trend can be observed in interfacial capacitance at CE/electrolyte or C_{CE} of the QDSSCs due to amount of charges accumulated at the interface of CE/electrolyte increased with increasing interfacial resistance: (0.84 ± 0.04) Ω cm^2, Au QDSSC > (0.65 ± 0.36) Ω cm^2, Pt QDSSC > (0.46 ± 0.28) Ω cm^2, PbS QDSSC. The interfacial resistance at interface of photoanode/electrolyte or R_{PA} of Au, Pt and PbS QDSSC are more or less the same in the range of 40.33–47.00 Ω cm^2. The trend of the interfacial capacitance at photoanode/electrolyte or C_{PA} is the same with that of R_{PA} i.e. in the same range (13.33–14.64 mF cm^2).

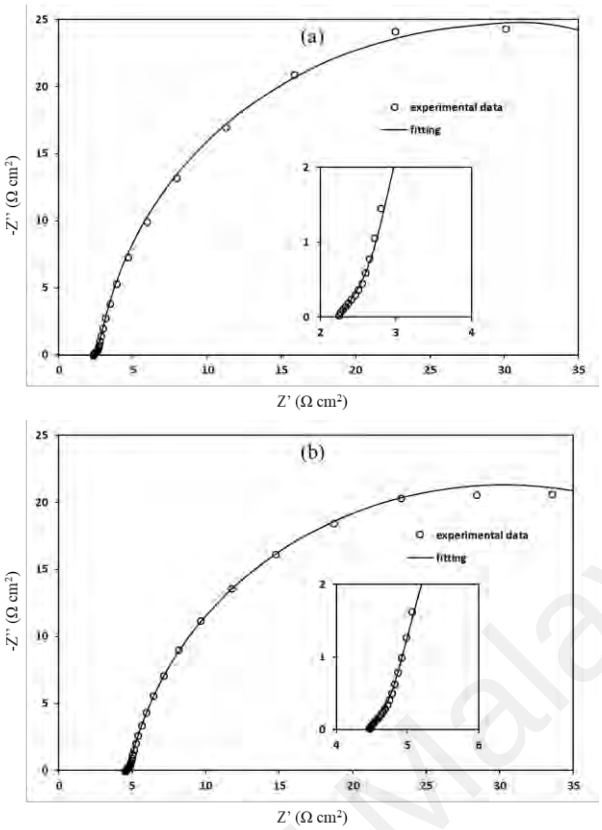

Figure 6.7: (a) and (b) show the Nyquist plots obtained from EIS analysis of MC–PGPE based QDSSCs fabricated with Au and PbS CEs respectively.

Table 6.4: The interfacial properties obtained from the Nyquist plots above.

Counter electrode	R_s **(Ω cm^2)**	R_{CE} **(Ω cm^2)**	R_{PA} **(Ω cm^2)**	C_{CE} **(mF cm^2)**	C_{PA} **(mF cm^2)**
Pt	2.52 ± 0.32	0.42 ± 0.02	40.33 ± 1.15	0.65 ± 0.36	13.33 ± 0.13
Au	2.33 ± 0.07	0.59 ± 0.08	47.00 ± 15.87	0.84 ± 0.04	14.64 ± 0.20
PbS	3.92 ± 0.89	0.34 ± 0.09	46.33 ± 6.35	0.46 ± 0.28	13.69 ± 0.24

6.6.2 Bode Plots

The electron lifetime (τ) of the MC–PGPE based QDSSCs fabricated with different CEs have been examined from the Bode plot. The value of τ has been calculated using the peak frequency of the Bode plot and Equation (3.18). Figure 6.8 shows the Bode plots obtained from EIS analysis while Table 6.5 lists the calculated τ values of the Pt, Au and PbS QDSSCs. PbS QDSSC exhibited the longest τ followed by Pt QDSSC and Au QDSSC.

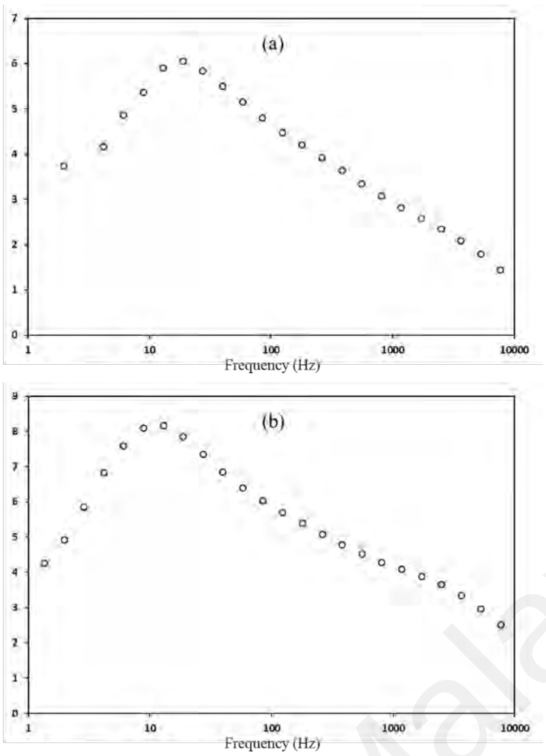

Figure 6.8: Bode plots obtained from the MC–PGPE based QDSSCs fabricated with (a) Au and (b) PbS CEs respectively.

Table 6.5: The electron lifetime value obtained from the bode plot above.

Counter electrode	Electron lifetime, *τ* (ms)
Pt	12.43 ± 0.12
Au	9.07 ± 0.36
PbS	13.33 ± 0.14

6.7 IPCE Study of MC–PGPE Based QDSSCs Fabricated with Different CE Materials

Figure 6.9 shows the IPCE curves obtained from MC–PGPE based QDSSCs fabricated with Au and PbS CEs. IPCE study is essential for the photovoltaic device since it will give information on how many incident photons converted to the electricity at a certain wavelength. The wavelength range of the IPCE curves of the Pt, Au and PbS are in the same range i.e. 300 to 600 nm. The highest IPCE exhibited by Au QDSSC is 51.50% at wavelength of 431.98 nm while the highest IPCE for the PbS QDSSC is 70.77% at wavelength of 427.99 nm.

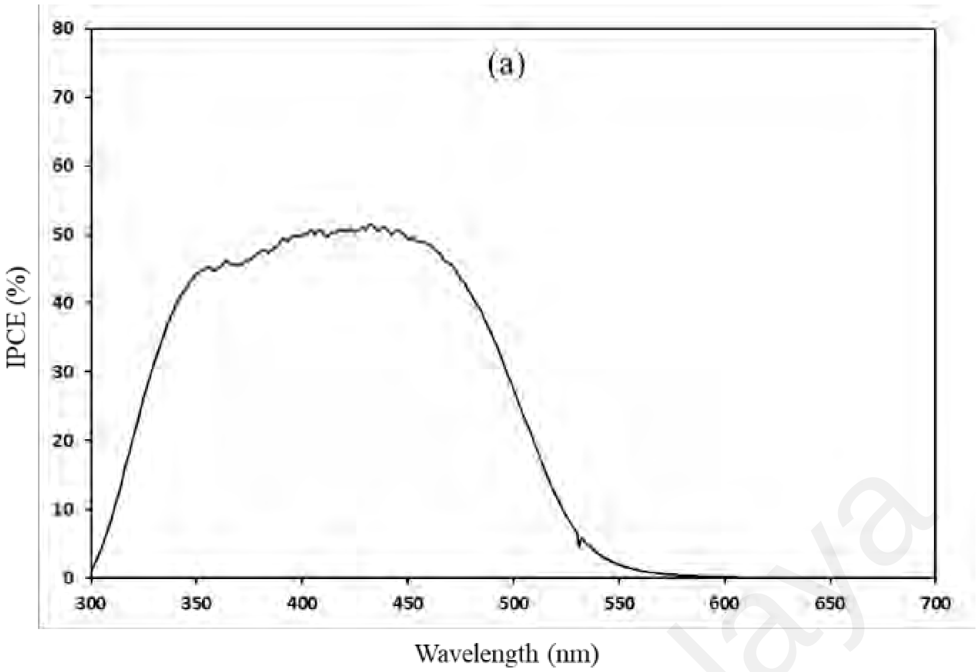

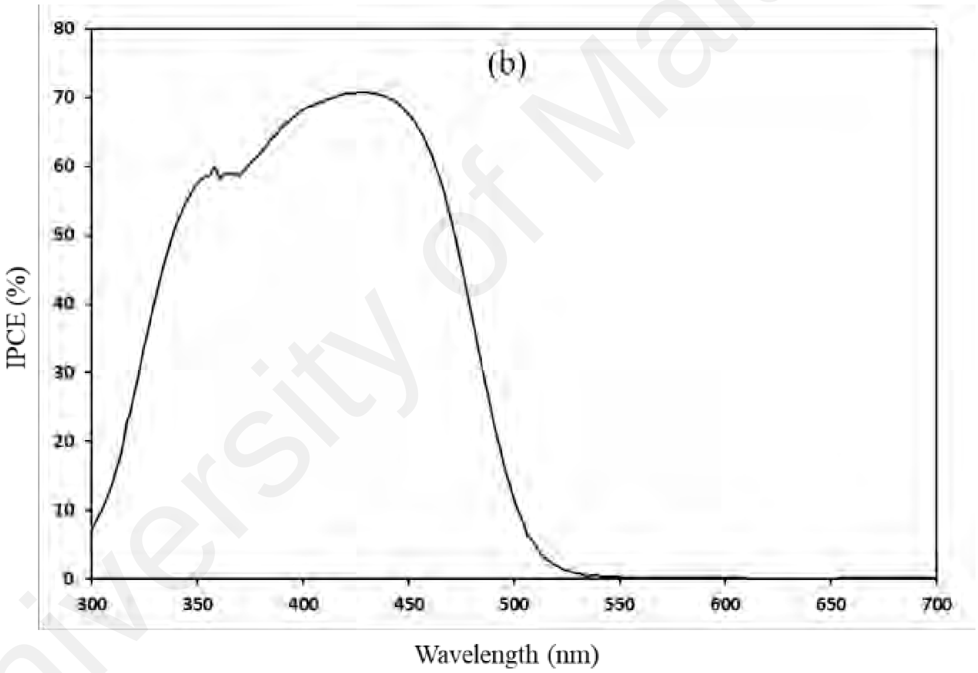

Figure 6.9: IPCE curves obtained from MC–PGPE based QDSSCs fabricated with (a) Au and (b) PbS CEs respectively.

6.8 Summary

- EIS measurements on the symmetric dummy cells revealed that the R_s value is highest for cell with Au CE followed by Pt and PbS. R_{dc} also exhibited the same trend. The C_{dc} of the Au symmetrical cell was the highest and followed by Pt and PbS symmetrical cells.

- Tafel polarization measurement revealed that highest J_{lim} and J_o were possessed by PbS symmetric cell followed by Pt and Au symmetric cells. The highest $D_{S_x^{2-}}$ was exhibited by PbS symmetric cell followed by Pt and Au symmetric cells. The lowest R_{dc} possessed by PbS symmetric cell followed by Pt and Au symmetric cells.
- Compared to the QDSSC fabricated with Pt, the *PCE* of Au QDSSC is slightly lower with percentage difference of 5.22%. While QDSSC fabricated with PbS exhibited excellent performance with *PCE* improvement of 111.19% compared to the Pt QDSSC.
- From the EIS measurements on QDSSCs, the Au QDSSC possessed the highest R_{CE} followed by Pt QDSSC and PbS QDSSC. The same trend can be observed for C_{CE} of the QDSSCs.
- From τ calculation, PbS QDSSC exhibited the longest τ followed by Pt QDSSC and Au QDSSC.
- The highest IPCE exhibited by Au QDSSC was 51.50% at 431.98 nm while the highest IPCE for the PbS QDSSC was 70.77% at 427.99 nm. (QDSSC fabricated with Pt CE exhibited the highest IPCE of 67.20% at wavelength 403 nm).

CHAPTER 7: DISCUSSION

7.1 Introduction

This chapter will discuss the results obtained to achieve the objectives of this work. Section 7.2 will discuss the results in Chapter 4 which is characterization and optimization of methylcellulose–polysulphide gel polymer electrolytes (MC–PGPEs), Section 7.3 will discuss the results in Chapter 5 which is optimization of the photoanode and Section 7.4 will discuss the results in Chapter 6 which is investigation of the best materials for the counter electrode (CE). Chapter 4, 5 and 6 contained the results to achieve objectives one, two and three of the current work respectively.

7.2 Discussion on the Characterization and Optimization of MC–PGPEs

The first objective of this work is to produce a novel polysulphide GPE with methylcellulose (MC) as the host polymer. The innovation is to use MC as the polymer host. Generally, MC is abundantly available, cheap, non-toxic and biocompatible. As a host polymer to the polymer electrolyte, MC is a good choice due to its high glass transition temperature (T_g) i.e. in the range of 176–200 °C (Rimdusit et al., 2008; Shuhaimi et al., 2010). According to Gu et al., (2008), a high T_g is better for the mechanical strength of a material since it will result in good film forming property and the polymer electrolyte will not be affected by high temperature (Park et al., 2001). However, there are many reports saying that ion transport through polymer electrolyte only occurs when the temperature is above T_g (Golodnitsky et al., 2015). Hence, using MC as a host for gel polymer electrolytes (GPEs) enables harnessing the advantages of MC since GPEs do have not have ionic transport restriction, that is, the ions are free to move through the solvent. Five samples of GPE with different composition of Na_2S have been prepared i.e. sample A (3.70 *wt.%* Na_2S, 3.70 *wt.%* MC, 92.50 *wt.%* distilled water, 0.10 *wt.%* S) sample B (5.45 *wt.%* Na_2S, 3.63 *wt.%* MC, 90.77 *wt.%* distilled water, 0.15 *wt.%* S), sample C (7.13 *wt.%* Na_2S, 3.56 *wt.%* MC, 89.11 *wt.%* distilled water, 0.20 *wt.%*

S), sample D (7.46 *wt.%* Na_2S, 3.55 *wt.%* MC, 88.78 *wt.%* distilled water, 0.21 *wt.%* S) and sample E (7.78 *wt.%* Na_2S, 3.54 *wt.%* MC, 88.46 *wt.%* distilled water, 0.22 *wt.%* S). Na_2S salt did not fully dissolve when the salt content was increased beyond 7.78 *wt.%*. Up to 7.78 *wt.%* conductivity continued to increase. This can be attributed to the increase in Na^+ and S^{2-} ion content with increasing amount of Na_2S (Golodnitsky et al., 2015). Increased ionic conductivity with increasing salt concentration is attributed to the increasing number of charge carrier ions (Na^+ and S^{2-}) in the electrolyte.

From the Arrhenius relation stated in Equations (3.8) and (3.9), the activation energy (E_a) of the MC–PGPEs were calculated. E_a can be thought of as the magnitude of the potential barrier or energy barrier separating the minimum of the potential energy surface pertaining to the initial and final thermodynamic state (Aziz et al., 2018). In this case, the E_a value was manifested as the energy required for the ions to become mobile. Hence, the high conducting MC–PGPE should possesses lower E_a compared to the low conducting MC–PGPE. The E_a obtained from the MC–PGPE samples in this work: sample A (72.49 meV) > sample B (67.56 meV) > sample C (62.49 meV) > sample D (58.19 meV) > sample E (55.25 meV). As expected, the E_a of the sample decreases as the ionic conductivity of the GPE sample increasing from sample A to sample E.

Ionic transport properties such as ionic diffusion coefficient (D), ionic number of density (n) and ionic mobility (μ) have been calculated by using Equations (3.4), (3.5) and (3.6) respectively. From the calculations, the ionic number of density, n of the GPE increased with the amount of Na_2S added. This supports the arguments mentioned by Mogurampelly et al. 2015 who stated that large concentration of salt results in increased ionic density of the electrolyte system and eventually led to increase in the ionic conductivity of the electrolyte. However, the μ of the MC–PGPE decreased with increasing of salt. This is an inkling for the increase in viscosity of the electrolytes. The increase in viscosity may be implied by the decrease in ionic mobility, μ. According to

Samir et al. (2005), enhancing the viscosity of polymer electrolyte will result in decrease in ionic mobility. This is because an increasing amount of ions inside the GPE will create high electrostatic hindrance between them which lead to the restriction of ion movement (Oh et al., 2002). The diffusion coefficient, D of the GPE has the same trend with μ decreasing with increasing of the Na_2S concentration. This agrees with Equation (3.5) which stated that D is directly proportional to μ. Hence, the ionic conductivity of the MC–PGPEs in this work is directly influenced by n i.e. high n produces high ionic conductivity and vice versa. From Equation (3.6), it can be rearranged into the Equation (7.1), which indicated that the ionic conductivity is product of the n and μ and electron charge, e.

$$\sigma = n\mu e \tag{7.1}$$

Based on the Equation (7.1), the ionic conductivity of the MC–PGPEs sample have been calculated and compared in Table 7.1. In Table 7.1, the ionic conductivity acquired from EIS measurement designated as σ_{exp} and ionic conductivity calculated from Equation (7.1) designated as σ_{cal}. The percentage difference between σ_{exp} and σ_{cal} are ranging from 3.31–31.08% as shown in the brackets inside the table. The value of σ_{exp} and σ_{cal} obtained are more or less the same with percentage difference lower than 31.08%. In addition, the ionic conductivities trend acquired from calculation exhibited the same trend as the ionic conductivity obtained from the EIS experiment. From Table 7.1, the percentage difference of σ between calculated and experimental values is higher (~30%) at low salt concentration samples (sample A and B) while the percentage difference is lower (~4%) for the high salt concertation samples (sample C, D and E). This can be attributed to the non–uniformity of the salt in MC–PGPE with low salt concentration. However, high concentration of salt will cause the composition be more uniform and hence the conductivity of the different portions of the samples will not differ significantly, hence the percentage difference is smaller. According to Boström et al. (2003), samples with high concentration of salt, the ions will be more dispersed and the conductivity will not differ significantly.

Table 7.1: Ionic conductivity of the MC–PGPE from the experiment and calculation [Equation (7.1)]. Take note that in the bracket is the percentage different with the σ calculated from the bulk resistance of the GPE.

Sample	σ_{exp} (S cm^{-1})	σ_{cal} at 0.2 kHz (S cm^{-1})	σ_{cal} at 2 kHz (S cm^{-1})
A	0.096	0.122 (27.08%)	0.126 (31.25%)
B	0.127	0.150 (18.11%)	0.146 (14.96%)
C	0.163	0.157 (3.68%)	0.157 (3.68%)
D	0.181	0.175 (3.31%)	0.187 (3.31%)
E	0.191	0.183 (4.19%)	0.184 (3.66%)

From the study of the ionic transport properties of MC–PGPE in this work: D and μ increases with the increasing of temperature while n exhibits the opposite trend i.e. decreases with increasing temperature. This behaviour can be related to the free-volume model (Turnbull et al., 1961). According to the free-volume model, elevating temperature will increase the free volume and thus increases the mobility as well as the diffusion of the ions. However, increased free volume will cause the density of the ions to reduce. This behaviour implies to the MC–GPE at both frequencies i.e. 0.2 kHz and 2 kHz.

Another important characteristic that has been studied is the dielectric constant that represents the capacity of the charged contained in the MC–PGPEs. The dielectric constant trend of the MC–GPE is: sample A < sample B < sample C < sample D < sample E which is same with the trend of the ionic conductivity. This implied that the salt concentration in the MC–GPE directly affects the stored charged. The trend of dielectric constant of the MC–GPE agrees with the increment of charge carrier concentration with increase in salt concentration. The dielectric constant also increased with temperature. In this case, the dielectric constant is affected by the mobility and the diffusion of the ions which also increases with increase in temperature.

The electrocatalytic properties such as limiting current density (J_{lim}), exchange current density (J_o) have been obtained from Tafel polarization measurements on the MC–PGPE samples using Pt electrodes. While polysulphide ion diffusion ($D_{S_x^{2-}}$) and charge transfer resistance between Pt CE/electrolyte (R_{dc}) have been calculated from J_{lim}, Equation (3.10) and J_o, Equation (3.11) respectively. Here, the J_{lim} was considered for S_x^{2-} ions as sulphide concentration was greater than the concentration of sulphur in the MC–GPE samples (Papageorgiou et al., 1996). The J_{lim} shown by MC–PGPE increased with increasing concentration of the Na_2S: $J_{lim,\mathrm{A}} < J_{lim,\mathrm{B}} < J_{lim,\mathrm{C}} < J_{lim,\mathrm{D}} < J_{lim,\mathrm{E}}$. However, the $D_{S_x^{2-}}$ of the MC–GPE decreased with increasing Na_2S concentration. The decrease of $D_{S_x^{2-}}$ with increasing of Na_2S concentration is due to the bottleneck situation that restricted the movement of the S_x^{2-} ions inside the MC–GPE. In addition, increasing amount of ions inside the MC–GPE will create high electrostatic hindrance between them that can lead to restriction of ionic movement (Oh et al., 2002). The trend of $D_{S_x^{2-}}$ agrees with the trend of ionic diffusion (D) calculated from decrease with increasing Na_2S concentration.

The exchange current density (J_o) between Pt CE/electrolyte in the symmetric dummy cell showed that the it increases with increasing Na_2S concentration: $J_{o,\mathrm{A}} < J_{o,\mathrm{B}} < J_{o,\mathrm{C}} < J_{o,\mathrm{D}} < J_{o,\mathrm{E}}$. While the calculated charge transfer resistance between Pt CE/electrolyte (R_{dc}) calculated from J_o decreased with increasing Na_2S concentration: $R_{dc,\mathrm{A}} > R_{dc,\mathrm{B}} > R_{dc,\mathrm{C}} > R_{dc,\mathrm{D}} > R_{dc,\mathrm{E}}$. This is a good signal since lower R_{dc} will favour the charge transfer process at the interface of CE/electrolyte. Lower R_{dc} indicates that the charge transfer between CE/electrolyte possesses lower resistance and produces more effective electrons which resulted in higher current density. Hence, utilization of MC–PGPE sample E with composition of 7.78 *wt.%* Na_2S will result in excellent electrocatalytic at the interface of Pt CE and electrolyte since Pt CE symmetric dummy cell fabricated with sample E possessed with lower R_{dc} which provide easy path for the charge transfer from CE to the electrolyte.

Due to the composition of at least 88 *wt.%* distilled water in the MC–PGPEs samples. the FTIR spectra generated is very similar to that of distilled water FTIR spectrum. However, there are some differences in the spectra in the wavenumber region between 850 and 1200 cm^{-1} and between 2350 and 3250 cm^{-1}. These differences are due to the presence of the MC in the composition of the GPEs. As can be seen in the MC–PGPE samples FTIR spectra, there are high intensity bands recorded in the range between 850 and 1200 cm^{-1}. This is due to C–O–C and C–H stretching located in the molecular structure of the MC. C–O–C stretching occurring inside an anhydroglucose ring can be determined in the range from 850 to 1200 cm^{-1} at 1050 cm^{-1} (Sekiguchi et al., 2003). The peak at 950 cm^{-1} is attributed to the C–H stretching that originated from CH_2 and CH_3 groups (Oliveira et al., 2015). At wavenumber 2350 to 3250 cm^{-1}, there is one peak corresponding to the C–H stretching in the structure of MC which is 2900 cm^{-1}. This peak has influenced the MC–GPE FTIR spectra to exhibited slightly higher absorbance compared to that of distilled water as shown in the figure below.

The optimized MC–PGPE obtained from this work is sample E with composition of 3.54 *wt.%* MC, 88.46 *wt.%* distilled water, 7.78 *wt.%* Na_2S and 0.22 *wt.%* sulphur. This MC–GPE exhibited the highest ionic conductivity at room temperature and the lowest activation energy i.e. (0.191 ± 0.001) S cm^{-1} and (55.25 ± 1.15) meV respectively. Hence, this sample will be utilized for the QDSSCs fabrication.

7.3 Discussion on the Characterization and Optimization of Photoanodes

7.3.1 Optimization of the CdS QDs Deposition

10 different TiO_2/CdS photoanodes i.e. TiO_2/CdS(1–10) photoanodes have been prepared in order to find out the suitable number of SILAR cycles for CdS QDs deposition on the TiO_2. CdS has been chosen since it is one of the cadmium chalcogenide quantum dots that have been frequently used as sensitizer in QDSSCs studies (Jun et al., 2013; Peter, 2011; Rhee et al., 2013). This is because preparation and deposition of cadmium chalcogenides on the surface of TiO_2 is easy. Moreover, the cadmium chalcogenides have conduction bands suitable for electron injection into the TiO_2. The absorption spectra of TiO_2/CdS(1) to TiO_2/CdS(5) photoanodes are in the wavelength range of 380–800 nm. However, the absorption spectra of TiO_2/CdS(6) to TiO_2/CdS(10) photoanode slightly narrow which in the range of 530–800 nm. This is because of the number of SILAR cycles used affects the size of the CdS QDs deposited on the TiO_2 layer (Jun et al., 2013). As the number of SILAR cycles used increased, the size of the CdS QDs also increased and may form agglomerates. Increased size and agglomeration of CdS QDs resulted in some of the light being blocked from passing the photoanode and eventually reduced the adsorption range of the TiO_2/CdS(6–10) photoanodes compared to the absorption range of TiO_2/CdS(1–5) photoanodes (Veerathangam et al., 2018).

Absorption intensity of TiO_2/CdS(1) to TiO_2/CdS(5) photoanodes increased with the number of SILAR cycles. The opposite trend in absorption intensity was observed for TiO_2/CdS(6) to TiO_2/CdS(10) photoanodes. The increase in absorption intensity for TiO_2/CdS(1) to TiO_2/CdS(5) photoanode is due to the increasing number of CdS QDs deposited on the surface of the TiO_2. However, depositing CdS QDs with more than five SILAR cycles is no longer beneficial due to the agglomeration and increasing size of CdS QDs that can block light from penetrating the photoanode and eventually reduce light absorption.

The absorption peak or absorption band edge can be seen in the absorption spectra of the TiO_2/CdS(1) to TiO_2/CdS(5) photoanode. However, there is no absorption peak observed from TiO_2/CdS(6) to TiO_2/CdS(10) photoanode. The absorption peak of the photoanodes appeared to be red shifted or shifted towards longer wavelength with increasing number of SILAR cycles: TiO_2/CdS(1) [480 nm] < TiO_2/CdS(2) [482 nm] < TiO_2/CdS(3) [483 nm] < TiO_2/CdS(4) [504 nm] < TiO_2/CdS(5) [511 nm]. The redshift of the absorption peak implied that the size of the CdS QDs increased with increasing number of SILAR cycles used (Chang et al., 2007). The optical energy transition or band gap of the TiO_2/CdS(1–10) photoanodes have been calculated based on Beer–Lambert's equation. The band gap of the photoanode is considered as the required amount of energy to remove the most loosely bound electron in the valence band of the QD and also determined the energy separation in between valence and conduction bands. From TiO_2/CdS(1) to TiO_2/CdS(5) photoanode, the band gap decreased with increasing number of SILAR cycles: TiO_2/CdS(1) [2.34 eV] > TiO_2/CdS(2) [2.34 eV] > TiO_2/CdS(3) [2.33 eV] > TiO_2/CdS(4) [2.27 eV] > TiO_2/CdS(5) [2.22 eV]. The changing of band gap with number of SILAR cycles used is due to the confinement effect i.e. the band gap of the QDs is different with its bulk material and depends on its size (Chang et al., 2007). Confinement effect happens when the size of a QD particle decreased till it reached a nano scale. The decrease in confining dimension makes the energy levels discrete and this increases or widens up the band gap (Chang et al., 2007).

Figure 7.1 shows the trend of the *J–V* parameters (J_{sc}, V_{oc}, *FF* and *PCE*) of the QDSSCs fabricated with 10 different type of photoanode i.e. TiO_2/CdS(1–10) photoanodes. From Figure 7.1, the *PCE* of the QDSSC increased with increasing number of SILAR cycles used until the maximum 0.77% for the QDSSC prepared with TiO_2/CdS(5) photoanode. The *PCE* of the QDSSCs fabricated are mainly affected by the J_{sc} as can be seen in Figure 7.1. The *PCE* trend is similar to J_{sc}. The increase in J_{sc} of the

QDSSC with increasing number of SILAR can be attributed to the amount of the CdS QDs deposited to the TiO_2 surface with increasing number of SILAR cycles. As the amount of the CdS QD deposited on the TiO_2 surface increases, it will result in increasing number density of electrons injected into the TiO_2 conduction band and eventually improve the J_{sc} and *PCE* of the QDSSCs. Another reason for the enhancement of *PCE* with the increasing number of SILAR cycles is due to the CdS QDs covering the surface of the TiO_2 layer. A good distribution of CdS QDs sensitizer on TiO_2 and coverage of the surface will result in good QDSSC performance as the electron recombination from TiO_2 to the electrolyte is reduced due to TiO_2 surface making less contact with the electrolyte. From EDX elemental map in Figure 5.12, it can be seen that the CdS QDs is well dispersed covering the photoanode surface. Overcoming recombination problem in QDSSC will result in enhancement of J_{sc}, V_{oc}, and *FF* and eventually will give a good result for *PCE* (Tachan et al., 2011).

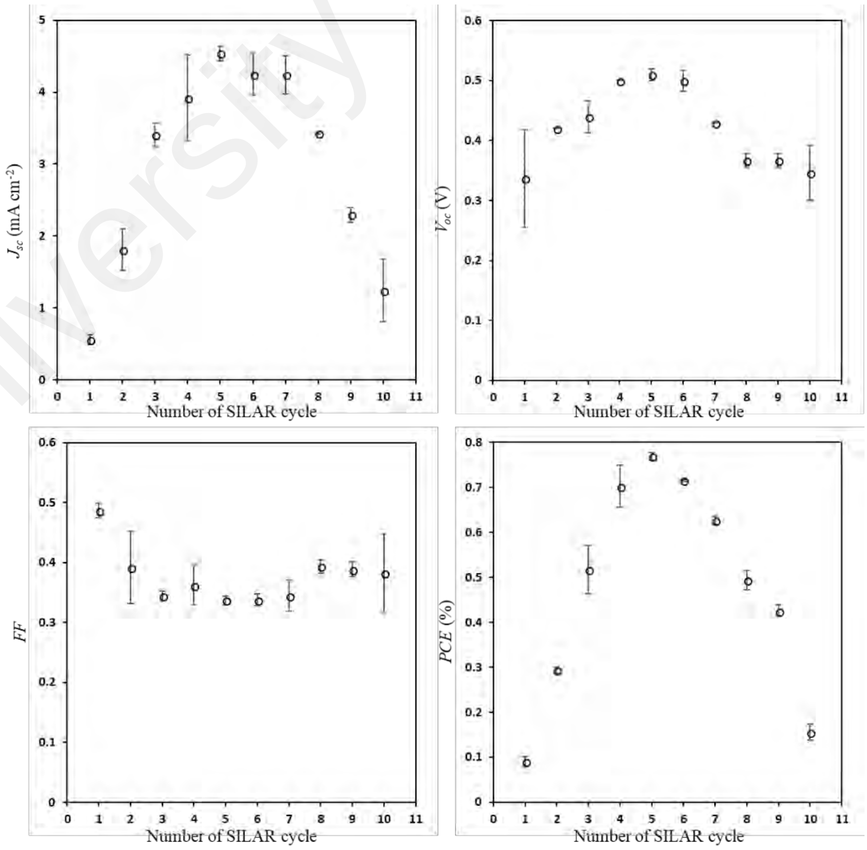

Figure 7.1: Trend of the *J–V* parameters of QDSSCs fabricated with TiO_2/CdS(1–10) photoanodes with optimized MC–PGPE and Pt CE.

However, as can be seen in Figure 7.1, there is a decrease in QDSSC performance as the number of SILAR cycles used was beyond five. The J_{sc} decreased with increasing number of SILAR cycles and led to the reduction of PCE. This reduction of the QDSSCs performance is related to the dispersed morphology of the deposited CdS QDs on the surface of the TiO_2. This reduction is due to the increasing size of deposited CdS QDs and agglomeration of QDs with increased number of SILAR cycles. The agglomeration of Cd QDs on the TiO_2 surface led to the reduced electron injection and increased resistance to electron travel reducing J_{sc} as well as the PCE of the QDSSCs.

EIS measurements were done in order to investigate the process at the interface of the electrode/electrolyte of the QDSSCs fabricated with TiO_2/CdS(1–10) photoanodes. From the measurement, the interfacial resistance at the boundary between electrolyte and photoanode (R_{PA}) increased with increasing of the number of SILAR cycles. For QDSSC fabricated with TiO_2/CdS(1) to TiO_2/CdS(5) photoanodes, the increased R_{PA} is beneficial since it will suppress the electron recombination process from photoanode to the electrolyte. However, increment of the R_{PA} for the QDSSCs fabricated with TiO_2/CdS(6) to TiO_2/CdS(10) photoanodes will cause the high resistance for the electron to transfer from S^{-2} ions to the photoanode and eventually reducing the J_{sc} and PCE of the QDSSCs. From the Bode plots for the QDSSCs fabricated with TiO_2/CdS(1–5) photoanodes exhibited longer τ compared to the QDSSCs fabricated with TiO_2/CdS(6–10) photoanodes. This showed that the electrons produced by the CdS QDs in the QDSSCs fabricated by TiO_2/CdS(1–5) photoanodes is effectively injected into the conduction band of the TiO_2 while the electrons produced in the QDSSCs fabricated with TiO_2/CdS(6–10) photoanodes easily recombined with the electrolyte. The τ value in the QDSSC imply the electron recombination resistance, higher τ value indicates the higher value of the recombination resistance in the sensitized solar cell device (Bisquert et al., 2009).

The IPCE curves of the QDSSC fabricated with TiO_2/CdS(1–10) are in the wavelength range of 300 to 600 nm. The highest IPCE achieved by the QDSSC increased with increasing of number of SILAR cycles until the maximum value was achieved for the QDSSC fabricated with TiO_2/CdS(5) photoanode, 9.41% at 417.99 nm. However, the maximum IPCE achieve by the QDSSC decreased for QDSSCs fabricated with TiO_2/CdS(6–10) photoanodes. IPCE results agree with the trend of the J_{sc} and *PCE* of the QDSSCs which increased with increasing number of SILAR cycles and decreased beyond that.

Hence, five SILAR cycles is the best to deposit the CdS QDs to the QDSSC photoanode since QDSSC fabricated with TiO_2/CdS(5) photoanode exhibits the highest *PCE* which is (0.77 ± 0.01)% with J_{sc} of (4.54 ± 0.10) mA cm^{-2}, V_{oc} of (0.51 ± 0.01) V and *FF* of (0.34 ± 0.03). In the next part of this work, five SILAR cycles will be utilized for the CdS QDs deposition to the photoanode.

7.3.2 Incorporation of the Passivation Layer for Performance Improvement

As the number of SILAR cycles for the CdS QDs deposition has been optimized. The next part of this work is to further improve the performance of the QDSSC. ZnS and SiO_2 passivation layers have been deposited on CdS QDs. Two types of photoanodes have been prepared i.e. TiO_2/CdS(5)/ZnS and TiO_2/CdS(5)/ZnS/SiO_2 photoanodes. ZnS and SiO_2 have been chosen due to these two materials is widely used and effectively suppressed the recombination process and improve the performance of the QDSSCs as reported in the literature. So far, there are many reports on QDSSC improvement by incorporating single ZnS passivation layer (Guijarro et al., 2011; Shen et al., 2008; Tubtimtae et al., 2012). There are less reports on incorporation of more than one passivation layer, however, it has been proven that this strategy can be used for the improvement of the QDSSC performance (Ren et al., 2015; Yang et al., 2015).

From the *J–V* characterizations, the performance of the QDSSCs is better with passivation layers as shown in Figure 7.2. With single ZnS passivation layer, the performance of the QDSSC improved by 54.54% with *PCE* of (1.19 ± 0.04)% compared to the QDSSC fabricated without any passivation layer i.e. *PCE* of (0.77 ± 0.01)%. With double passivation layers (ZnS and SiO_2), the performance of the QDSSC is further increases by 57.00% with *PCE* of (1.34 ± 0.13)% compared to the QDSSC fabricated without any passivation layer. Based on Figure 7.2, the trend of *PCE* are mainly affected by the J_{sc} of the QDSSC. Other *J–V* parameters such as V_{oc} and *FF* of the QDDSCs fabricated with and without passivation layer are more or less the in the same range.

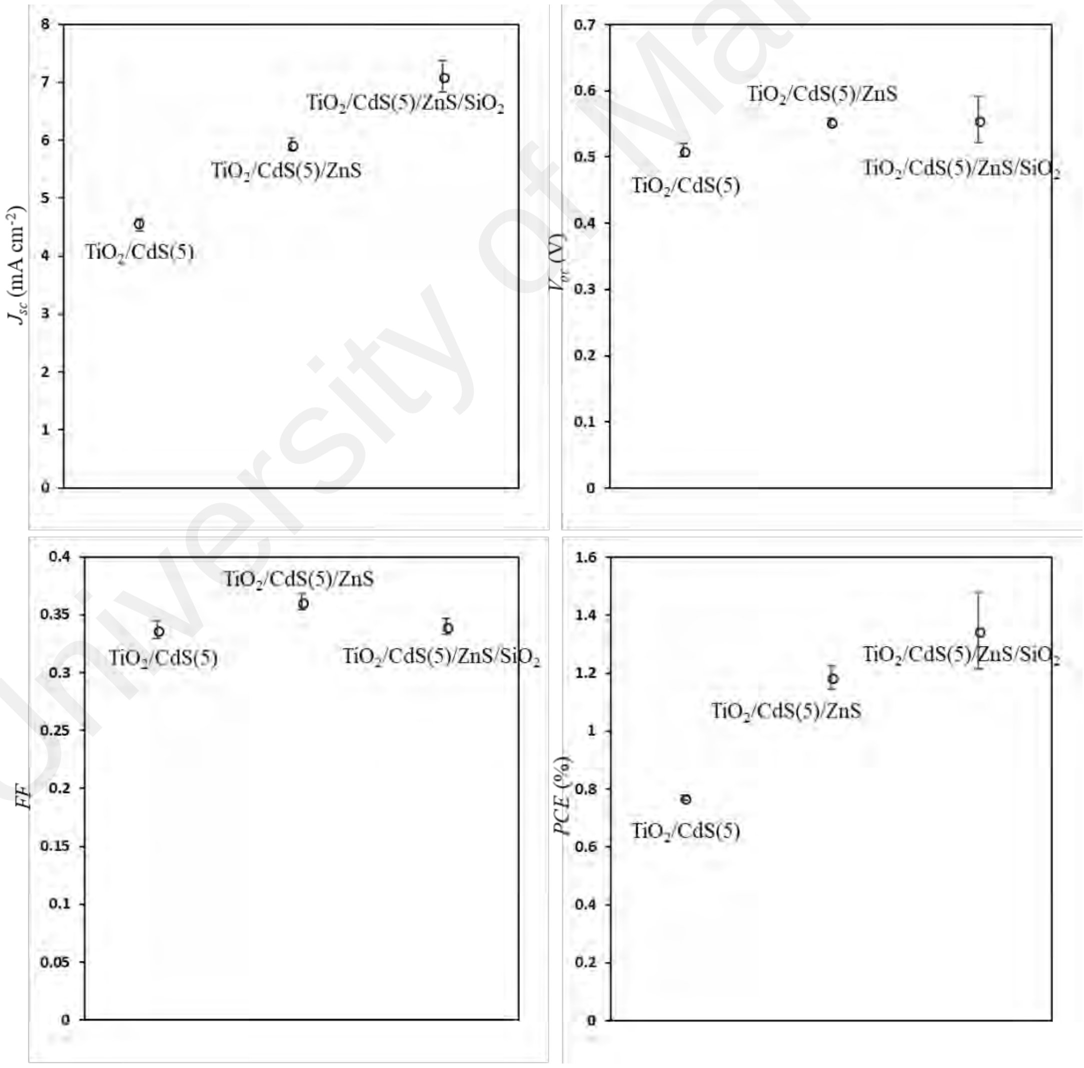

Figure 7.2: *J–V* characteristics trend of the QDSSCs fabricated with and without passivation layers.

The IPCE result agrees with the J_{sc} parameters of the QDSSCs. Without any passivation layer, the highest IPCE obtained is 9.41% at wavelength of 417.99 nm. With single ZnS passivation layer, the highest IPCE obtained was 57.24% at 407.00 nm. While with double passivation layers (ZnS and SiO_2), the IPCE further increased to 67.20% at 403 nm. This result implied that the percentage of the light converted into electricity improved with the passivation layer, hence, improving the J_{sc} and PCE of the QDSSC.

By knowing the interfacial process (in this work through EIS), the roles of the passivation layers in the QDSSCs fabricated can be determined. The interfacial resistance at the photoanode/electrolyte interface or R_{PA} is the resistance for electrons to recombine with the S_x^{-2} ions in the electrolyte. In other words, R_{PA} is a recombination resistance. From EIS results, R_{PA} of the QDSSCs increased with implementation of the passivation layers: (21.67 ± 0.57) Ω cm^2, TiO_2/CdS(5) < (30.31 ± 2.27) Ω cm^2, TiO_2/CdS(5)/ZnS < (40.33 ± 1.15) Ω cm^2, TiO_2/CdS(5)/ZnS/SiO_2. The QDSSC without any passivation layers showed a lower recombination resistance at the interface of photoanode and electrolyte compared to the QDSSCs fabricated with passivation layers. The lower value of recombination resistance will easily promote the process of recombination which explained the low J_{sc} of the QDSSC fabricated (Ng et al., 2015). With ZnS passivation layer, the value of recombination resistance increased preventing recombination of electrons with S_x^{2-} ions which can be implied from the increased J_{sc} exhibited by the QDSSC. With double passivation layer (ZnS and SiO_2) recombination resistance further increased and reduced the rate of electron recombination and J_{sc} was observed to increase. The calculated electron lifetimes (τ) of the QDSSCs fabricated with and without passivation layer showed that τ of the devices increased with the passivation layer: (5.77 ± 0.12) ms, TiO_2/CdS(5) < (6.90 ± 0.98) ms, TiO_2/CdS(5)/ZnS < (12.43 ± 0.12) ms, TiO_2/CdS(5)/ZnS/SiO_2. This further supported the results from recombination resistance of the QDSSC. According to Bisquert et al. (2009), the recombination resistance is directly reflected by the τ of the QDSSC i.e. the longer τ is a manifestation of the large recombination resistance. Hence, the passivation layer obviously improved the performance of the QDSSCs by suppressing the electron recombination process and resulted in the increment of J_{sc} and *PCE* of the QDSSC.

From the UV–Vis absorption spectra, another role of passivation layer has been revealed i.e. improving the light absorption of the photoanode. Improving the absorption of the QDSSCs photoanode will lead to the improvement of the amount of the electrons produce at the photoanode and eventually improve the electricity generated in the QDSSC. This agrees with the IPCE results which showed that the IPCE of the QDSSC increased with implementation of the passivation layers. The absorption of the QDSSC was improved with addition of single ZnS passivation layer compared to without any passivation layer. The absorption is further increased with double passivation layers (ZnS and SiO_2): TiO_2/CdS(5) < TiO_2/CdS(5)/ZnS < TiO_2/CdS(5)/ZnS/SiO_2. This implies that passivation layers will improve the light absorption capability of the photoanode which will result in J_{sc} increase and *PCE* improvement. The absorption peak of nanoparticles will undergo blueshift with surface modification (Kislov, Srinivasan, Emirov, & Stefanakos, 2008). The blueshift of the absorption peak indicate decrease in size of the nanoparticle (QDs sensitizer and passivation layers) deposited on the photoanode. This implies that the CdS QDs deposited become more dispersed and less agglomerate with deposition of passivation layer which results in absorption intensity of the light as shown by the UV–Vis absorption spectra.

From the photoanode study, it can be concluded that the photoanode with deposition arrangement of TiO_2/CdS(5)/ZnS/SiO_2 is the most suitable for use since it favours the performance of the QDSSC. Hence, the second objective of this work has been achieved and this photoanode will be utilized in the next part of this work which is the study of the CE.

7.4 Discussion on the Investigation for the Best Counter Electrode Material

Au and PbS have been chosen due to their properties that could be beneficial for replacing Pt as the counter electrode (CE). Au categorized in the same group with Pt i.e. noble metal. PbS CE is known to provide enhancement of the J_{sc} and V_{oc} of the QDSSC due to its absorption capability and auxiliary tandem effect respectively. It is to be noted that the electrolyte and photoanode used in this part are sample E and $TiO_2/CdS(5)/ZnS/SiO_2$ that have been optimized and investigated from the previous experiments.

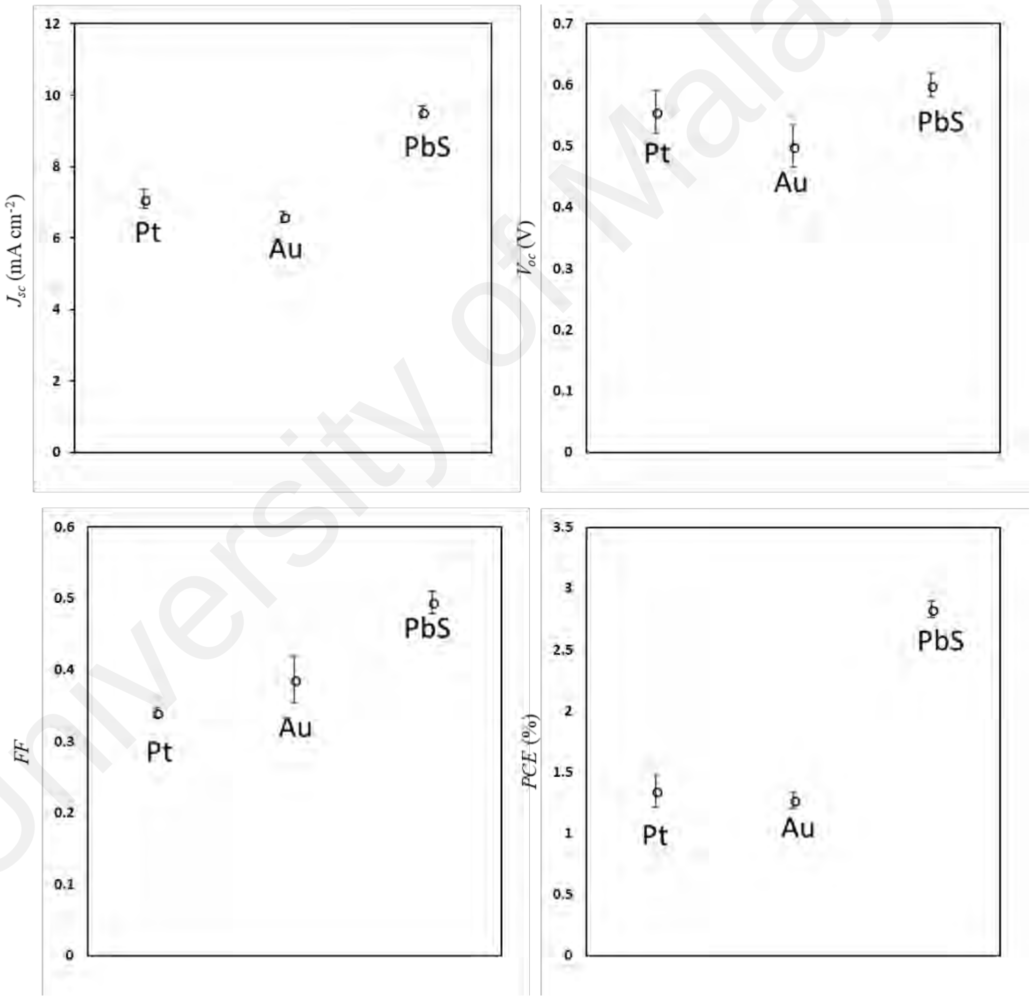

Figure 7.3: *J–V* parameters of the QDSSCs fabricated with different CE materials.

From the *J–V* characterizations as shown in Figure 7.3, the highest performance is shown by QDSSC fabricated with PbS CE with *PCE* of (2.83 ± 0.07)%. QDSSC with PbS CE exhibited *PCE* improvement by 111.19% compared to the QDSSCs fabricated with Pt CE that exhibited *PCE* of (1.34 ± 0.13)%. However, the performance of the QDSSC fabricated with Au CE showed a slightly lower performance compared to the QDSSC fabricated with Pt CE with percentage difference of 5.22%. Its *PCE* was (1.27 ± 0.06)%. The highest *PCE* of the PbS QDSSC resulted from the enhancement of the J_{sc}, V_{oc} and *FF*. QDSSC fabricated with Au CE exhibited the lowest J_{sc} and V_{oc}. Hence, Au is not a good material to replace the Pt CE in our QDSSC system. According to Pensa et al. (2012), there is reaction between polysulphide electrolyte system and gold CE. Sulphur can adsorb to the surface of the Au CE to form covalent bond (polysulphide ions adsorbed to the surface of the Au CE) and structures (AuS is produced due to Au corrosion). This process is called "Au poisoning effect" and explains the low performance showed by QDSSC fabricated with Au CE.

Improvement of the J_{sc} and V_{oc} of the QDSSC is due to the auxiliary tandem effect formed with the presence of the PbS CE. The enhancement of the J_{sc} is due to the ability of PbS to absorb light in the visible to near infrared (~1000 nm) (Gibson, 1950). The remnant infrared light that pass through the photoanode will be absorbed by the PbS CE to generate additional electrons and eventually increased the current generated as well as the J_{sc} of the QDSSC. The V_{oc} enhancement in the PbS QDSSC is due to the the additional photovoltage in the QDSSC system, generated due to the p-type PbS semiconductors with lower Fermi level will create additional potential in the QDSSC system as shown in Figure 7.4 (Lin et al., 2013). The highest *FF* value for QDSSC fabricated with PbS CE indicates that PbS is the most catalytic material for MC–PGPE containing polysulphide as redox couples (Tachan et al., 2011). Here, the most "catalytic material" means that the rate of the electron transfer from the material to the S_x^{2-} ions is faster compared to other materials.

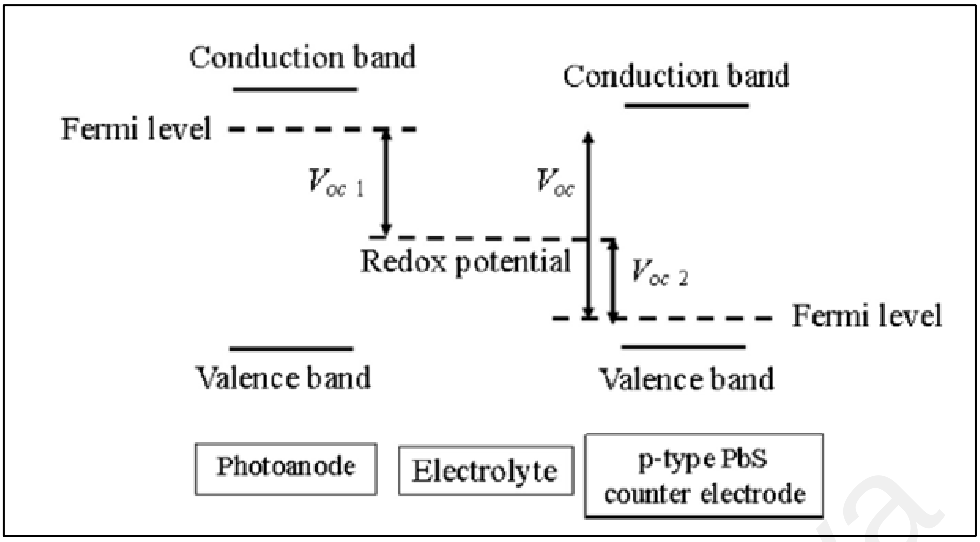

Figure 7.4: Energy band in QDSSC with PbS CE. (Mingsukang et al., 2017)

From the IPCE results, QDSSC fabricated with PbS CE showed the highest maximum IPCE achieved, which is 70.77% at 427.99 nm. And the lowest maximum IPCE, 51.20% achieved from QDSSC fabricated with Au CE at 431.98 nm. The highest IPCE was exhibited from QDSSC fabricated with PbS CE. This device converted light into electricity at wide range of wavelength which resulted in high J_{sc} of the QDSSC. This is because the PbS CE also acted as photocathode that harvest the remnant light that pass through the photoanode and facilitate electron injection to the electrolyte. The lowest IPCE showed by QDSSC fabricated with Au CE resulted from the "Au poisoning effect" which reduce the electricity generate in the device.

EIS measurement has been done to gain information on interfacial processes in the QDSSCs fabricated with Au and PbS CEs. The interfacial resistance at interface of CE/electrolyte or R_{CE} of the QDSSC fabricated with PbS CE is the lowest while the QDSSC fabricated with Au CE exhibited the highest R_{CE}: (0.59 ± 0.08) Ω cm^2, Au QDSSC > (0.42 ± 0.02) Ω cm^2, Pt QDSSC > (0.34 ± 0.09) Ω cm^2, PbS QDSSC. Lower R_{CE} value is beneficial to the performance of the QDSSC since it will increase electron transfer rate from CE to the electrolyte and will increase the stability and performance of the cell. This proved that the PbS QDSSC possessed high catalytic property for electron transfer at the interface of CE/electrolyte that resulted in the high *FF* (0.49 ± 0.03) compared to Pt QDSSC [*FF,* (0.34 ± 0.01)] and Au QDSSC [*FF*, (0.37 ± 0.03)]. High R_{CE} exhibited by QDSSC fabricated with Au CE is due to the Au poisoning effect. Au poisoning effect will supress the electron transfer from CE to the S_x^{2-} ions in the electrolyte consequently reducing J_{sc} and *FF* of the QDSSC. This implied that Au is not catalytic for the electron transfer from CE to electrolyte.

From the electron lifetime (τ) calculation, the highest lifetime of (13.33 ± 0.14) ms observed for the PbS CE. This confirmed the fast transfer of electron at the interface of CE/electrolyte helps to reduce S_x^{2-} ions accumulation at the photoanode and thereby reduce the electron recombination to improve the photocurrent and voltage (Lin et al., 2013). While the QDSSC fabricated with Au CE exhibited the lowest τ i.e. (9.07 ± 0.36) ms. Lowest τ indicated high recombination rate at the interface of photoanode/electrolyte due to the accumulation of S_x^{2-} ions at the photoanode. Slow electrons transfer from Au CE to the S_x^{2-} ions in the electrolyte cause the amount of S_x^{2-} ions accumulate in the electrolyte higher which increases the electron recombination rate. This can be confirmed by the C_{CE} of Au QDSSC [(0.84 ± 0.04 Ω) cm^2] is higher compared to Pt QDSSC [(0.65 ± 0.36 Ω) cm^2] and PbS QDSSC [(0.46 ± 0.28 Ω) cm^2]. Hence, QDSSC with Au CE produces the lowest performance.

To further confirm the electron transfer process at interface of CE/electrolyte, the EIS analysis has been done with Pt, Au and PbS symmetrical dummy cells. Symmetrical dummy cells were fabricated with both electrodes being Pt or Au or PbS separated with MC–PGPE in the form of film. The charge transfer resistance observed from the PbS symmetrical dummy cells is smaller (3.00 ± 0.25) Ω cm^2 compared to Pt (5.07 ± 0.19) Ω cm^2 and Au (8.59 ± 1.26) Ω cm^2. This trend is similar to the interfacial resistance at interface of CE/electrolyte or R_{PA} obtained from the EIS measurement of the full QDSSC devices. The small charge transfer resistance shown by PbS symmetrical dummy cells indicates that the reduction rate of the S_x^{2-} ions to S^{2-}ions in the electrolyte are faster. The large charge transfer resistance shown by Au symmetrical dummy cells stipulate that the reduction process of the S_x^{2-} ions is slow. EIS of the symmetrical dummy cells results agree with the previous results that implies the outstanding performance of the QDSSC fabricated with PbS CE and poor performance of the QDSSC fabricated with Au CE.

The electrocatalytic properties such as limiting current density (J_{lim}), exchange current density (J_o) have been obtained from Tafel polarization measurement of the Pt, Au and PbS symmetrical dummy cell separated with MC–PGPE. While polysulphide ion diffusion ($D_{S_x^{2-}}$) and charge transfer resistance between Pt CE/electrolyte (R_{dc}) have been calculated from J_{lim}, Equation (3.10) and J_o, Equation (3.11) respectively. Here, the J_{lim} was considered for S_x^{2-} ions as sulphide concentration was greater than the concentration of S in the MC–PGPE samples (Papageorgiou et al., 1996).

PbS symmetrical cell showed the highest J_{lim} followed by Pt and Au symmetrical cells: PbS > Pt > Au. The calculated $D_{S_x^{2-}}$ also showed the same trend which PbS symmetrical cell possessed the highest followed by Pt and Au symmetrical cells. This showed that the S_x^{2-} ions in the PbS symmetric dummy cell possessed higher degree of diffusivity compared to Pt and Au symmetric dummy cell. High diffusivity of the S_x^{2-} ions in the PbS symmetric dummy cell indicates that the PbS exhibited high catalytic degree toward MC–PGPE which resulted in high value of the transferred current density (Hwang et al., 2015). Au symmetric cell possessed the lowest $D_{S_x^{2-}}$ which indicate that the diffusivity of the S_x^{2-} ions is low. This is due to the reaction that occurred between polysulphide electrolyte and gold CE. Sulphur entities (S^{2-}, S_x^{2-}, etc.) in the electrolyte will adsorb to the surface of the Au CE and hinders the electron transfer process. This process is called "Au poisoning effect" and explains the low performance exhibited by QDSSC fabricated with Au CE (Pensa et al., 2012).

The exchange current density (J_o) between Au, Pt and PbS symmetric dummy cell obtained from Tafel polarization showed that the PbS symmetric dummy cell possessed the highest J_o followed by Pt and Au symmetric dummy cells: PbS > Pt > Au. While the calculated charge transfer resistance between CE/electrolyte (R_{dc}) calculated by using Equation (3.11) showed that the PbS symmetric dummy cell possessed the lowest R_{dc} followed by Pt and Au symmetric dummy cells: PbS < Pt < Au. Lower R_{dc} will favour the charge transfer process at interface of CE/electrolyte. Lower R_{dc} showed by PbS symmetric dummy cell indicates that the charge transfer between PbS CE and electrolyte possesses lower resistance and produces more effective electrons which resulted in higher current density. Hence, MC–PGPE based QDSSC fabricated with PbS will give excellent performance as shown in *J-V* characteristics. Due to the Au poisoning effect, The R_{dc} showed by Au symmetric cell is high which indicates that the charge transfer between Au CE and electrolyte possesses high resistance and produces less effective electrons which resulted in lower current density. As a result, the QDSSC fabricated with Au CE possessed lower performance.

Table 7.2: Comparison of the R_{dc} values of the Pt, Au and PbS symmetric dummy cells from EIS and Tafel polarization measurements.

Symmetric dummy cell	EIS R_{dc} (Ω cm^2)	Tafel R_{dc} (Ω cm^2)	Percentage difference (%)
Pt	5.07 ± 0.19	5.67 ± 0.15	11.83
Au	8.59 ± 1.26	8.39 ± 1.57	2.32
PbS	3.00 ± 0.25	3.05 ± 0.62	1.67

Table 7.2 show the R_{dc} of obtained from EIS and Tafel polarization measurement of the Pt, Au and PbS symmetric dummy cells. From EIS measurement, R_{dc} values were obtained from the semicircle of the Nyquist plot while while R_{dc} from Tafel measurement is calculated by using Equation (3.11). Can be seen that the R_{dc} values of the symmetric dummy cells from both measurements are same with small percentage different. Hence,

both measurements are related to each other and reliable for determining catalytic properties of the CE material of the sensitized solar cells.

The combination of excellent J_{sc}, V_{oc} and FF led to the best overall performance for the QDSSC with PbS CE. The better performance of the QDSSC with PbS CE is due to excellent properties of PbS such as highly catalytic toward polysulphide electrolyte and could form auxiliary tandem effect in the QDSSC system. On the other hand, Au CE exhibited the lowest performance among the CEs tried in this investigation. The lowest performance is related to the Au poisoning effect that reducing the charge transfer at interface of CE/electrolyte which lead to reduce of J_{sc}, V_{oc}, FF and PCE of the QDSSC.

CHAPTER 8: CONCLUSION AND SUGGESTION FOR FURTHER WORK

8.1 Conclusion

The novel methylcellulose–polysulphide gel polymer electrolyte (MC–PGPE) has been produced in this work. The MC–PGPE with the composition of 3.54 *wt.%* methylcellulose (MC), 88.46 *wt.%* distilled water, 7.78 *wt.%* Na_2S and 0.22 *wt.%* sulphur exhibited the best ionic conductivity of (0.191 ± 0.001) S cm^{-1} at room temperature with low activation energy of (55.25 ± 1.15) meV. High ionic conductivity was attributed to the high charge carrier density. The interfacial resistance between Pt CE and sample E MC–PGPE is the lowest i.e. (5.67 ± 0.15) Ω cm^2 calculated from Tafel polarization measurement. Lower interfacial resistance between CE and electrolyte will give easy path for the electron transfer and will improve the current density of the QDSSC. In FTIR analysis, presence of the MC in the MC–PGPE samples can be traced at wavenumber of 850 to1200 cm^{-1} and 2350 to 3250 cm^{-1} which due to the C–O– C (1050 cm^{-1}) and C–H (950 cm^{-1} and 2900 cm^{-1}) structures inside MC. Hence, the first objective of this work which is to develop and optimized conductivity of the polysulphide GPE system by using MC as a host polymer have been achieved.

Good distribution of CdS QDs sensitizer on the photoanode having CdS QDs deposited with five SILAR cycles [TiO_2/CdS(5) photoanode] give the best performance with J_{sc} of (4.54 ± 0.10) mA/cm^2, V_{oc} of (0.51 ± 0.01) V, *FF* of (0.34 ± 0.03) and *PCE* of (0.77 ± 0.01)%. Based on UV–Vis analysis, the good performance of the QDSSC fabricated with TiO_2/CdS(5) photoanode can be attributed to the TiO_2/CdS(5) photoanode that exhibited high absorption intensity.

The performance of the QDSSC was improved by suppressing the recombination process at interface of photoanode and electrolyte by depositing ZnS passivation layer on the TiO_2/CdS(5) photoanode. QDSSC fabricated with TiO_2/CdS(5)/ZnS photoanode exhibited *PCE* improvement by 54.54% [*PCE* of (1.19 ± 0.04)%, J_{sc} of (5.93 ± 0.12) mA/cm^2, V_{oc} of (0.55 ± 0.01) V and *FF* of (0.36 ± 0.01)] compared to the QDSSC fabricated without passivation layer. The performance of the QDSSC was further enhanced with addition of another passivation layer i.e. SiO_2 layer on the TiO_2/CdS(5)/ZnS photoanode. Compared to the QDSSC fabricated without passivation layer, QDSSC fabricated with TiO_2/CdS(5)/ZnS/SiO_2 photoanode exhibited *PCE* improvement by 57.00% with *PCE* of (1.34 ± 0.13)%, J_{sc} of (7.09 ± 0.27) mA/cm^2, V_{oc} of (0.56 ± 0.04) V and *FF* of (0.34 ± 0.01). Based on EIS analysis, recombination process at interface of photoanode and electrolyte in the QDSSC was successfully suppressed with the help of passivation layers. In addition, the absorption intensity of the photoanode with passivation layers was observed to be higher compared to the photoanode without passivation layer, Thus, revealing another role of the passivation layers. The passivation layers help to improve light absorption of the photoanode. When more light is absorbed, more electrons can be generated and the current density produced increased. This is further confirmed from IPCE studies.

In the last part of this work, Au and PbS have been studied to find out the better material for the counter electrode (CE) of the QDSSC with MC–PGPE and TiO_2/CdS(5)/ZnS/SiO_2 photoanode. PbS was found to be the better material as CE. The performance of the QDSSC with PbS CE showed *PCE* enhancement by 111.19% with *PCE* of (2.83 ± 0.07)%, J_{sc} of (9.54 ± 0.16) mA/cm^2, V_{oc} of (0.60 ± 0.02) V and *FF* of (0.49 ± 0.03) compared to the QDSSC fabricated with Pt CE. The enhancement of the *PCE* is due to the improvement of J_{sc}, V_{oc} and *FF*. Good performance of PbS QDSSC is also attributed to the auxiliary tandem effect that provided additional current density and voltage in the QDSSC system. In addition, PbS CE exhibited higher catalytic properties toward MC–PGPE. High catalytic properties of Pb CE can be seen in the study of symmetrical dummy cell using EIS and Tafel polarization measurements. From EIS and Tafel polarization measurements, it has been revealed that the interfacial resistance between CE and MC–PGPE is low, thus provides easy path for the charge transfer. Also, the diffusion of polysulphide ions calculated from Tafel polarization is high. Hence, PbS is the better to be used for the MC–PGPE based QDSSC.

FTO/TiO_2/CdS(5)/ZnS/SiO_2/MC–PGPE (sample E)/PbS (CE) QDSSC assembly exhibited the highest *PCE* i.e. (2.83 ± 0.07)% with J_{sc} of (9.54 ± 0.16) mA/cm^2, V_{oc} of (0.60 ± 0.02) V and *FF* of (0.49 ± 0.03). IPCE of this QDSSC is 70.77% at 427.99 nm. The novel MC–PGPE that has been used for this QDSSC assembly exhibited ionic conductivity of (0.191 ± 0.001) S cm^{-1} at room temperature with activation energy of (55.25 ± 1.15) meV. The photoanode used i.e. TiO_2/CdS(5)/ZnS/SiO_2 has good light absorption properties and successfully suppressed electron recombination and PbS is the better material as CE for MC–PGPE based QDSSC.

8.2 Suggestions for Further Works

The present study has developed some thoughts for future dimension of research. For the continuation of this research in future, some suggestions can be made based on the findings/insights of the present work. These suggestions that have been made such as:

- Study of different salt (ions contributors for example lithium sulphide (Li_2S), potassium sulphide (K_2S), acetyl sulphide ($C_4H_6O_2S$), diphenyl sulphide ($C_{12}H_{10}S$), etc.
- Study on double cation effect in the application of QDSSCs. This can be studied by mixing two types of salt in electrolyte.
- Utilization of chemical additives in electrolyte. In DSSCs, additive chemical is a very popular strategy to improve the performance of the cells. Example of additive chemicals are ionic liquid, TBP, GuNCS, KCl, NaOH, etc

REFERENCES

Aziz, S. B., Woo, T. J., Kadir, M. F. Z., & Ahmed, H. M. (2018). A conceptual review on polymer electrolytes and ion transport models. *Journal of Science: Advanced Materials and Devices, 3*(1), 1-17.

Badawi, A. (2015). Decrease of back recombination rate in CdS quantum dots sensitized solar cells using reduced graphene oxide. *Chinese Physics B, 24*(4), 047205.

Badawi, A., Easawi, K., Al-Hosiny, N., & Abdallah, S. (2014). Alloyed CdTe quantum dots sensitized TiO_2 electrodes for photovoltaic applications. *Materials Sciences and Applications, 5,* 27-32.

Bailey, R. E., & Nie, S. (2003). Alloyed semiconductor quantum dots: tuning the optical properties without changing the particle size. *Journal of the American Chemical Society, 125*(23), 7100-7106.

Bandara, T. M. W. J., & Mellander, B.-E. (2011). Evaluation of Mobility, Diffusion Coefficient and Density of Charge Carriers in Ionic Liquids and Novel Electrolytes Based on a New Model for Dielectric Response. in A. Kokorin (Ed.), *Ionic Liquids* (pp. 383-406). Rijeka, Crotia: IntechOpen.

Barreca, A. I. (2012). Climate change, humidity, and mortality in the United States. *Journal of Environmental Economics and Management, 63*(1), 19-34.

Bisquert, J., Fabregat-Santiago, F., Mora-Seró, I., Garcia-Belmonte, G., & Giménez, S. (2009). Electron lifetime in dye-sensitized solar cells: theory and interpretation of measurements. *The Journal of Physical Chemistry C, 113*(40), 17278-17290.

Bisquert, J., Garcia-Belmonte, G., Fabregat-Santiago, F., Ferriols, N. S., Bogdanoff, P., & Pereira, E. C. (2000). Doubling exponent models for the analysis of porous film electrodes by impedance. relaxation of TiO_2 nanoporous in aqueous solution. *The Journal of Physical Chemistry B, 104*(10), 2287-2298.

Blakers, A., Zin, N., McIntosh, K. R., & Fong, K. (2013). High efficiency silicon solar cells. *Energy Procedia, 33*, 1-10.

Boström, M., Williams, D. R. M., & Ninham, B. W. (2003). Specific ion effects: why the properties of lysozyme in salt solutions follow a hofmeister series. *Biophysical Journal, 85*(2), 686-694.

Caputo, J. A., Frenette, L. C., Zhao, N., Sowers, K. L., Krauss, T. D., & Weix, D. J. (2017). General and efficient C–C bond forming photoredox catalysis with semiconductor quantum dots. *Journal of the American Chemical Society, 139*(12), 4250-4253.

Cerdán-Pasarán, A., Esparza, D., Zarazúa, I., Reséndiz, M., López-Luke, T., De la Rosa, E., Fuentes-Ramirez, R., Alotorre-Orddaz, A., & Martínez-Benítez, A. (2016). Photovoltaic study of quantum dot-sensitized $TiO_2/CdS/ZnS$ solar cell with P3HT or P3OT added. *Journal of Applied Electrochemistry, 46*(9), 975-985.

Chang, C.-H., & Lee, Y.-L. (2007). Chemical bath deposition of CdS quantum dots onto mesoscopic TiO_2 films for application in quantum-dot-sensitized solar cells. *Applied Physics Letters, 91*(5), 053503.

Charles, R. G., Davies, M. L., & Douglas, P. (2016). Third generation photovoltaics-Early intervention for circular economy and a sustainable future, presented at berlin, 7-9 Sept. 2016: Electronics Goes Green 2016+ (EGG).

Chen, H.-Y., Lin, L., Yu, X.-Y., Qiu, K.-Q., Lü, X.-Y., Kuang, D.-B., & Su, C.-Y. (2013). Dextran based highly conductive hydrogel polysulfide electrolyte for efficient quasi-solid-state quantum dot-sensitized solar cells. *Electrochimica Acta, 92*, 117-123.

Chen, H., Fu, W., Yang, H., Sun, P., Zhang, Y., Wang, L., Zhoa, W., Zhou, X., Zhao, H., Jing, Q., Qi, X., & Li, Y. (2010). Photosensitization of TiO_2 nanorods with CdS quantum dots for photovoltaic devices. *Electrochimica Acta, 56*(2), 919-924.

Chen, H., Zhu, L., Liu, H., & Li, W. (2014). Efficient iron sulfide counter electrode for quantum dots-sensitized solar cells. *Journal of Power Sources, 245*, 406-410.

Choi, Y., Seol, M., Kim, W., & Yong, K. (2014). Chemical bath deposition of stoichiometric CdSe quantum dots for efficient quantum-dot-sensitized solar cell application. *The Journal of Physical Chemistry C, 118*(11), 5664-5670.

Daud, M. N. M., Zakaria, A., Jafari, A., Ghazali, M. S. M., Abdullah, W. R. W., & Zainal, Z. (2012). Characterization of CdTe films deposited at various bath temperatures and concentrations using electrophoretic deposition. *International Journal of Molecular Sciences, 13*(5), 5706-5714.

De Iacovo, A., Venettacci, C., Colace, L., Scopa, L., & Foglia, S. (2016). PbS colloidal quantum dot photodetectors operating in the near infrared. *Scientific Reports, 6*, 37913, 1-9.

Duan, J., Tang, Q., He, B., & Chen, H. (2015). All-solid-state quantum dot-sensitized solar cell from plastic crystal electrolyte. *RSC Advances, 5*(42), 33463-33467.

Duan, J., Tang, Q., Sun, Y., He, B., & Chen, H. (2014). Solid-state electrolytes from polysulfide integrated polyvinylpyrrolidone for quantum dot-sensitized solar cells. *RSC Advances, 4*(105), 60478-60483.

Faber, M. S., Park, K., Cabán-Acevedo, M., Santra, P. K., & Jin, S. (2013). Earth-abundant cobalt pyrite (CoS_2) thin film on glass as a robust, high-performance counter electrode for quantum dot-sensitized solar cells. *The Journal of Physical Chemistry Letters, 4*(11), 1843-1849.

Fabregat-Santiago, F., Bisquert, J., Palomares, E., Otero, L., Kuang, D., Zakeeruddin, S. M., & Grätzel, M. (2007). Correlation between photovoltaic performance and impedance spectroscopy of dye-sensitized solar cells based on ionic liquids. *The Journal of Physical Chemistry C, 111*(17), 6550-6560.

Farris, S., Schaich, K. M., Liu, L., Piergiovanni, L., & Yam, K. L. (2009). Development of polyion-complex hydrogels as an alternative approach for the production of bio-based polymers for food packaging applications: a review. *Trends in Food Science & Technology, 20*(8), 316-332.

Feng, W., Li, Y., Du, J., Wang, W., & Zhong, X. (2016). Highly efficient and stable quasi-solid-state quantum dot-sensitized solar cells based on a superabsorbent polyelectrolyte. *Journal of Materials Chemistry A, 4*(4), 1461-1468.

Golodnitsky, D., Strauss, E., Peled, E., & Greenbaum, S. (2015). Review—on order and disorder in polymer electrolytes. *Journal of The Electrochemical Society, 162*(14), A2551-A2566.

Gao, B., Shen, C., Yang, Y., Yuan, S., & Chen, G. (2014). Green synthesized CdSe quantum dots capped by 3-mercaptopropionic acid sensitized solar cells. In A. Y. Oral, Z. B. Bahsi & M. Ozer (Eds.), *International Congress on Energy Efficiency and Energy Related Materials (ENEFM2013): Proceedings, Antalya, Turkey, 9-12 October 2013* (pp. 9-17). Cham: Springer International Publishing.

Ghobadi, N. (2013). Band gap determination using absorption spectrum fitting procedure. *International Nano Letters, 3*(2), 1-4.

Gibson, A. F. (1950). The absorption spectra of solid lead sulphide, selenide and telluride. *Proceedings of the Physical Society. Section B, 63*(10), 756-767.

Gong, X., Yang, Z., Walters, G., Comin, R., Ning, Z., Beauregard, E., Adinolfi, V,. Voznyy, O,. & Sargent, E. H. (2016). Highly efficient quantum dot near-infrared light-emitting diodes. *Nature Photonics, 10*, 253-257.

Gopi, C. V. V. M., Singh, S., Eswar Reddy, A., & Kim, H.-J. (2018). CNT@rGO@MoCuSe composite as an efficient counter electrode for quantum dot-sensitized solar cells. *ACS Applied Materials & Interfaces, 10*(12), 10036-10042.

Gratzel, M. (2005). Solar energy conversion by dye-sensitized photovoltaic cells. *Inorganic Chemistry, 44*, 6841-6851.

Green, M. A. (2009, 7-12 June). *Third generation photovoltaics: assessment of progress over the last decade.* Paper presented at the 34th IEEE Photovoltaic Specialists Conference (PVSC).

Guijarro, N., Campina, J. M., Shen, Q., Toyoda, T., Lana-Villarreal, T., & Gomez, R. (2011). Uncovering the role of the ZnS treatment in the performance of quantum dot sensitized solar cells. *Physical Chemistry Chemical Physics, 13*(25), 12024-12032.

Hanna, M. C., & Nozik, A. J. (2006). Solar conversion efficiency of photovoltaic and photoelectrolysis cells with carrier multiplication absorbers. *Journal of Applied Physics, 100*(7), 074510.

Hariskos, D., Powalla, M., Chevaldonnet, N., Lincot, D., Schindler, A., & Dimmler, B. (2001). Chemical bath deposition of CdS buffer layer: prospects of increasing materials yield and reducing waste. *Thin Solid Films, 387*(1), 179-181.

Hodes, G., Manassen, J., & Cahen, D. (1977). Photo-electrochemical energy conversion: electrocatalytic sulphur electrodes. *Journal of Applied Electrochemistry, 7*(2), 181-182.

Hodes, G., Manassen, J., & Cahen, D. (1980). Electrocatalytic electrodes for the polysulfide redox system. *Journal of The Electrochemical Society, 127*(3), 544-549.

Huang, S., Sun, H., Huang, X., Zhang, Q., Li, D., Luo, Y., & Meng, Q. (2012). Carbon nanotube counter electrode for high-efficient fibrous dye-sensitized solar cells. *Nanoscale Research Letters, 7*(1), 222.

Hwang, I., & Yong, K. (2015). Counter electrodes for quantum-dot-sensitized solar cells. *ChemElectroChem, 2*(5), 634-653.

Jasim, K. E. (2015). Quantum dots solar cells. In L. A. Kosyachenko (Ed.), *Solar Cells - New Approaches and Reviews* (pp. Ch. 11). Rijeka: InTech.

Jun, H. K., Buraidah, M. H., Noor, M. M., Kufian, M. Z., Majid, S. R., Sahraoui, B., & Arof, A. K. (2013). Application of LiBOB-based liquid electrolyte in co-sensitized solar cell. *Optical Materials, 36*(1), 151-158.

Jun, H. K., Careem, M. A., & Arof, A. K. (2013). Quantum dot-sensitized solar cells—perspective and recent developments: A review of Cd chalcogenide quantum dots as sensitizers. *Renewable and Sustainable Energy Reviews, 22*(Supplement C), 148-167.

Jun, H. K., Careem, M. A., & Arof, A. K. (2013). A suitable polysulfide electrolyte for CdSe quantum dot-sensitized solar cells. *International Journal of Photoenergy, 2013*, 1-10.

Jung, S. W., Kim, J.-H., Kim, H., Choi, C.-J., & Ahn, K.-S. (2012). ZnS overlayer on in situ chemical bath deposited CdS quantum dot-assembled TiO_2 films for quantum dot-sensitized solar cells. *Current Applied Physics, 12*(6), 1459-1464.

Kamitakahara, H., Yoshinaga, A., Aono, H., Nakatsubo, F., Klemm, D., & Burchard, W. (2008). New approach to unravel the structure–property relationship of methylcellulose. *Cellulose, 15*(6), 797-801.

Kashyout, A. B., Soliman, H. M. A., Fathy, M., Gomaa, E. A., & Zidan, A. A. (2012). CdSe quantum dots for solar cell cevices. *International Journal of Photoenergy, 2012*, 1-7.

Kavan, L., Yum, J.-H., & Graetzel, M. (2014). Graphene-based cathodes for liquid-junction dye sensitized solar cells: Electrocatalytic and mass transport effects. *Electrochimica Acta, 128*, 349-359.

Kern, R., Sastrawan, R., Ferber, J., Stangl, R., & Luther, J. (2002). Modeling and interpretation of electrical impedance spectra of dye solar cells operated under open-circuit conditions. *Electrochimica Acta, 47*(26), 4213-4225.

Kim, H., Hwang, I., & Yong, K. (2014). Highly durable and efficient quantum dot-sensitized solar cells based on oligomer gel electrolytes. *ACS Applied Materials & Interfaces, 6*(14), 11245-11253.

Kislov, N., Srinivasan, S. S., Emirov, Y., & Stefanakos, E. K. (2008). Optical absorption red and blue shifts in $ZnFe_2O_4$ nanoparticles. *Materials Science and Engineering: B, 153*(1), 70-77.

Kobayashi, K., Huang, C.-i., & Lodge, T. P. (1999). Thermoreversible gelation of aqueous methylcellulose solutions. *Macromolecules, 32*(21), 7070-7077.

Kurzin, A. V., Evdokimov, A. N., Golikova, V. S., & Pavlova, O. S. (2010). Solubility of sodium sulfide in alcohols. *Journal of Chemical & Engineering Data, 55*(9), 4080-4081.

Lamb, W. F. (2016). Which countries avoid carbon-intensive development? *Journal of Cleaner Production, 131*, 523-533.

Lamb, W. F., & Rao, N. D. (2015). Human development in a climate-constrained world: What the past says about the future. *Global Environmental Change, 33*, 14-22.

Lan, Z., Wu, W., Zhang, S., Que, L., & Wu, J. (2016). Preparation of high-efficiency CdS quantum-dot-sensitized solar cells based on ordered TiO_2 nanotube arrays. *Ceramics International, 42*(7), 8058-8065.

Lana-Villarreal, T., Font-Sanchis, E., Sastre-Santos, Á., Fernández-Lázaro, F., & Gómez, R. (2011). Characterization and polymerization of thienylphenyl and selenylphenyl amines and their interaction with CdSe quantum dots. *ChemPhysChem, 12*(6), 1155-1164.

Lee, H., Leventis, H. C., Moon, S.-J., Chen, P., Ito, S., Haque, S. A., Torres, T., Nuesch, F., Geiger, T., Zakeeruddin, S. M., Gratzel M., & Nazeeruddin, M. K. (2009). PbS and CdS quantum dot-sensitized solid-state solar cells: “Old concepts, new results”. *Advanced Functional Materials, 19*(17), 2735-2742.

Lee, L. T. L., He, J., Wang, B., Ma, Y., Wong, K. Y., Li, Q., Xiao, X., & Chen, T. (2014). Few-layer $MoSe_2$ possessing high catalytic activity towards iIodide/tri-iodide redox shuttles. *Scientific Reports, 4*, 4063.

Lee, W., Min, S. K., Dhas, V., Ogale, S. B., & Han, S.-H. (2009). Chemical bath deposition of CdS quantum dots on vertically aligned ZnO nanorods for quantum dots-sensitized solar cells. *Electrochemistry Communications, 11*(1), 103-106.

Lee, Y.-L., & Chang, C.-H. (2008). Efficient polysulfide electrolyte for CdS quantum dot-sensitized solar cells. *Journal of Power Sources, 185*(1), 584-588.

Lee, Y.-L., & Lo, Y.-S. (2009). Highly efficient quantum-dot-sensitized solar cell based on co-sensitization of CdS/CdSe. *Advanced Functional Materials, 19*(4), 604-609.

Lewis, N. S., & Nocera, D. G. (2006). Powering the planet: Chemical challenges in solar energy utilization. *Proceedings of the National Academy of Sciences, 103*(43), 15729-15735.

Lin, C.-Y., Teng, C.-Y., Li, T.-L., Lee, Y.-L., & Teng, H. (2013). Photoactive p-type PbS as a counter electrode for quantum dot-sensitized solar cells. *Journal of Materials Chemistry A, 1*(4), 1155-1162.

Lindroos, S., Arnold, A., & Leskelä, M. (2000). Growth of CuS thin films by the successive ionic layer adsorption and reaction method. *Applied Surface Science, 158*(1), 75-80.

Liu, D., & Kamat, P. V. (1993). Photoelectrochemical behavior of thin cadmium selenide and coupled titania/cadmium selenide semiconductor films. *The Journal of Physical Chemistry, 97*(41), 10769-10773.

Liu, Z., Miyauchi, M., Uemura, Y., Cui, Y., Hara, K., Zhao, Z., Sunahara, k., & Furube, A. (2010). Enhancing the performance of quantum dots sensitized solar cell by SiO_2 surface coating. *Applied Physics Letters, 96*(23), 233107.

Long, L., Wang, S., Xiao, M., & Meng, Y. (2016). Polymer electrolytes for lithium polymer batteries. *Journal of Materials Chemistry A, 4*(26), 10038-10069.

Marie-Isabelle, B. (2012). Nano-TiO_2 for dye-sensitized solar cells. *Recent Patents on Nanotechnology, 6*(1), 10-15.

McElroy, N., Page, R. C., Espinbarro-Valazquez, D., Lewis, E., Haigh, S., O'Brien, P., & Binks, D. J. (2014). Comparison of solar cells sensitised by CdTe/CdSe and CdSe/CdTe core/shell colloidal quantum dots with and without a CdS outer layer. *Thin Solid Films, 560*(Supplement C), 65-70.

Meng, K., Chen, G., & Thampi, K. R. (2015). Metal chalcogenides as counter electrode materials in quantum dot sensitized solar cells: a perspective. *Journal of Materials Chemistry A, 3*(46), 23074-23089.

Mingsukang, M. A., Buraidah, M. H., & Arof, A. K. (2017). Third-generation-sensitized solar cells. In N. Das (Ed.), *Nanostructured Solar Cells* (pp. Ch. 02). Rijeka: InTech.

Mingsukang, M. A., Buraidah, M. H., & Careem, M. A. (2017). Development of gel polymer electrolytes for application in quantum dot-sensitized solar cells. *Ionics, 23*(2), 347-355.

Mingsukang, M. A., Buraidah, M. H., Careem, M. A., Albinsson, I., Mellander, B. E., & Arof, A. K. (2017). Investigation of counter electrode materials for gel polymer electrolyte based quantum dot sensitized solar cells. *Electrochimica Acta, 241*, 487-496.

Morales-Ortega, A., Carvajal-Millan, E., López-Franco, Y., Rascón-Chu, A., Lizardi-Mendoza, J., Torres-Chavez, P., & Campa-Mada, A. (2013). Characterization of water extractable arabinoxylans from a spring wheat flour: Rheological properties and microstructure. *Molecules, 18*(7), 8417.

Mukherjee, A., Satpati, B., Bhattacharyya, S. R., Ghosh, R., & Mitra, P. (2015). Synthesis of nanocrystalline CdS thin film by SILAR and their characterization. *Physica E: Low-dimensional Systems and Nanostructures, 65*, 51-55.

Murray, C. B., Norris, D. J., & Bawendi, M. G. (1993). Synthesis and characterization of nearly monodisperse CdE (E = sulfur, selenium, tellurium) semiconductor nanocrystallites. *Journal of the American Chemical Society, 115*(19), 8706-8715.

Nashed, R., Ismail, Y., & Allam, N. K. (2013). Recent advances in the use of density functional theory to design efficient solar energy-based renewable systems. *Journal of Renewable and Sustainable Energy, 5*(2), 022701.

Nei de Freitas, J., Nogueira, A. F., & De Paoli, M.-A. (2009). New insights into dye-sensitized solar cells with polymer electrolytes. *Journal of Materials Chemistry, 19*(30), 5279-5294.

Ng, H. M., Ramesh, S., & Ramesh, K. (2015). Efficiency improvement by incorporating 1-methyl-3-propylimidazolium iodide ionic liquid in gel polymer electrolytes for dye-sensitized solar cells. *Electrochimica Acta, 175*(Supplement C), 169-175.

Nozik, A. J. (2005). Exciton multiplication and relaxation dynamics in quantum dots: Applications to ultrahigh-efficiency solar photon conversion. *Inorganic Chemistry, 44*(20), 6893-6899.

O'Regan, B., & Gratzel, M. (1991). A low-cost, high-efficiency solar cell based on dye-sensitized colloidal TiO_2 films. *Nature, 353*(6346), 737-740.

Oh, B. K., Jung, W. I., Kim, D. W., & Rhee, H. W. (2002). Preparation of UV curable gel polymer electrolytes and their electrochemical properties. *Bulletin of the Korean Chemical Society, 23*(5), 683-687.

Oliveira, R. L., Vieira, J. G., Barud, H. S., Assunção, R. M. N., R. Filho, G., Ribeiro, S. J. L., & Messadeqq, Y. (2015). Synthesis and characterization of methylcellulose produced from bacterial cellulose under heterogeneous condition. *Journal of the Brazilian Chemical Society, 26*, 1861-1870.

Ortega, P. F. R., Trigueiro, J. P. C., Silva, G. G., & Lavall, R. L. (2016). Improving supercapacitor capacitance by using a novel gel nanocomposite polymer electrolyte based on nanostructured SiO_2, PVDF and imidazolium ionic liquid. *Electrochimica Acta, 188*(Supplement C), 809-817.

Ozeki, T., Yuasa, H., & Okada, H. (2005). Controlled release of drug via methylcellulose-carboxyvinylpolymer interpolymer complex solid dispersion. *AAPS PharmSciTech, 6*(2), E231-E236.

Pan, Z., Zhang, H., Cheng, K., Hou, Y., Hua, J., & Zhong, X. (2012). Highly efficient inverted type-I CdS/CdSe core/shell structure QD-sensitized solar cells. *ACS Nano, 6*(5), 3982-3991.

Papageorgiou, N., Athanassov, Y., Armand, M., Bonhoʎte, P., Pettersson, H., Azam, A., & Grätzel, M. (1996). The performance and stability of ambient temperature molten salts for solar cell applications. *Journal of The Electrochemical Society, 143*(10), 3099-3108.

Park, N.-G. (2015). Perovskite solar cells: an emerging photovoltaic technology. *Materials Today, 18*(2), 65-72.

Park, J. S., Park, J. W., & Ruckenstein, E. (2001). Thermal and dynamic mechanical analysis of PVA/MC blend hydrogels. *Polymer, 42*(9), 4271-4280.

Patel, P. (2012). Quantum dots are behind new displays. *IEEE Spectrum, 49*(8), 14-17.

Pathan, H. M., & Lokhande, C. D. (2004). Deposition of metal chalcogenide thin films by successive ionic layer adsorption and reaction (SILAR) method. *Bulletin of Materials Science, 27*(2), 85-111.

Pawar, S. A., Patil, D. S., Lokhande, A. C., Gang, M. G., Shin, J. C., Patil, P. S., & Kim, J. H. (2016). Chemical synthesis of CdS onto TiO$_2$ nanorods for quantum dot sensitized solar cells. *Optical Materials, 58*, 46-50.

Pensa, E., Cortés, E., Corthey, G., Carro, P., Vericat, C., Fonticelli, M. H., Benitez, G., Rubert, A. A., & Salvarezza, R. C. (2012). The chemistry of the Sulfur–Gold Interface: In Search of a Unified Model. *Accounts of Chemical Research, 45*(8), 1183-1192.

Peter, L. M. (2011). The Grätzel cell: Where next? *The Journal of Physical Chemistry Letters, 2*(15), 1861-1867.

Radich, J. G., Dwyer, R., & Kamat, P. V. (2011). Cu$_2$S reduced graphene oxide composite for high-efficiency quantum dot solar cells. Overcoming the redox limitations of S^{2-}/S_n^{2-} at the counter electrode. *The Journal of Physical Chemistry Letters, 2*(19), 2453-2460.

Rakhshani, A. E., & Al-Azab, A. S. (2000). Characterization of CdS films prepared by chemical-bath deposition. *Journal of Physics: Condensed Matter, 12*(40), 8745-8755.

Ren, Y., Ma, Z., & Bruce, P. G. (2012). Ordered mesoporous metal oxides: synthesis and applications. *Chemical Society Reviews, 41*(14), 4909-4927.

Ren, Z., Wang, J., Pan, Z., Zhao, K., Zhang, H., Li, Y., Zhoa, Y., Mora-Sero, I., Bisquert, J., & Zhong, X. (2015). Amorphous TiO$_2$ buffer layer boosts efficiency of quantum dot sensitized solar cells to over 9%. *Chemistry of Materials, 27*(24), 8398-8405.

Reverchon, E., Adami, R., Cardea, S., & Porta, G. D. (2009). Supercritical fluids processing of polymers for pharmaceutical and medical applications. *The Journal of Supercritical Fluids, 47*(3), 484-492.

Rhee, J. H., Chung, C.-C., & Diau, E. W.-G. (2013). A perspective of mesoscopic solar cells based on metal chalcogenide quantum dots and organometal-halide perovskites. *Npg Asia Materials, 5*, e68.

Rimdusit, S., Jingjid, S., Damrongsakkul, S., Tiptipakorn, S., & Takeichi, T. (2008). Biodegradability and property characterizations of Methyl Cellulose: Effect of nanocompositing and chemical crosslinking. *Carbohydrate Polymers, 72*(3), 444-455.

Samadpour, M., Irajizad, A., Taghavinia, N., & Molaei, M. (2011). A new structure to increase the photostability of CdTe quantum dot sensitized solar cells. *Journal of Physics D: Applied Physics, 44*(4), 045103.

Sanehira, E. M., Marshall, A. R., Christians, J. A., Harvey, S. P., Ciesielski, P. N., Wheeler, L. M., Luther, J. M. (2017). Enhanced mobility CsPbI quantum dot arrays for record-efficiency, high-voltage photovoltaic cells. *Science Advances, 3*(10), eaao4204.

Sayama, K., Sugihara, H., & Arakawa, H. (1998). Photoelectrochemical properties of a porous Nb_2O_5 electrode sensitized by a ruthenium Dye. *Chemistry of Materials, 10*(12), 3825-3832.

Sekiguchi, Y., Sawatari, C., & Kondo, T. (2003). A gelation mechanism depending on hydrogen bond formation in regioselectively substituted O-methylcelluloses. *Carbohydrate Polymers, 53*(2), 145-153.

Seo, M. H., Hwang, W. P., Kim, Y. K., Lee, J. K., & Kim, M. R. (2011, 19-24 June). *Improvement of Quantum Dot-Sensitized Solar Cells based on Cds and CdSe Quantum Dots.* Paper presented at the 2011 37th IEEE Photovoltaic Specialists Conference.

Shalom, M., Dor, S., Rühle, S., Grinis, L., & Zaban, A. (2009). Core/CdS quantum dot/shell mesoporous solar cells with improved stability and efficiency using an amorphous TiO_2 coating. *The Journal of Physical Chemistry C, 113*(9), 3895-3898.

Shalom, M., Hod, I., Tachan, Z., Buhbut, S., Tirosh, S., & Zaban, A. (2011). Quantum dot based anode and cathode for high voltage tandem photo-electrochemical solar cell. *Energy & Environmental Science, 4*(5), 1874-1878.

Shen, Q., Kobayashi, J., Diguna, L. J., & Toyoda, T. (2008). Effect of ZnS coating on the photovoltaic properties of CdSe quantum dot-sensitized solar cells. *Journal of Applied Physics, 103*(8), 084304.

Shuhaimi, N. E. A., Teo, L. P., Majid, S. R., & Arof, A. K. (2010). Transport studies of NH_4NO_3 doped methyl cellulose electrolyte. *Synthetic Metals, 160*(9), 1040-1044.

Sixto, G., Iván, M.-S., Lorena, M., Nestor, G., Teresa, L.-V., Roberto, G., Diguna, L. J., Shen, Q., Toyoda, T., & Juan, B. (2009). Improving the performance of colloidal quantum-dot-sensitized solar cells. *Nanotechnology, 20*(29), 295204.

Solovyev, A. A., Zakharov, A. N., Rabotkin, S. V., & Kovsharov, N. F. (2016). Electrochromic device with polymer electrolyte. *Journal of Electronic Materials, 45*(8), 3866-3871.

Späth, M., Sommeling, P. M., van Roosmalen, J. A. M., Smit, H. J. P., van der Burg, N. P. G., Mahieu, D. R., Bakeer, N.J., & Kroon, J. M. (2003). Reproducible manufacturing of dye-sensitized solar cells on a semi-automated baseline. *Progress in Photovoltaics: Research and Applications, 11*(3), 207-220.

Sudhagar, P., Jung, J. H., Park, S., Sathyamoorthy, R., Ahn, H., & Kang, Y. S. (2009). Self-assembled CdS quantum dots-sensitized TiO_2 nanospheroidal solar cells: Structural and charge transport analysis. *Electrochimica Acta, 55*(1), 113-117.

Sun, W.-T., Yu, Y., Pan, H.-Y., Gao, X.-F., Chen, Q., & Peng, L.-M. (2008). CdS quantum dots sensitized TiO_2 nanotube-array photoelectrodes. *Journal of the American Chemical Society, 130*(4), 1124-1125.

Tachan, Z., Shalom, M., Hod, I., Rühle, S., Tirosh, S., & Zaban, A. (2011). PbS as a highly catalytic counter electrode for polysulfide-based quantum dot solar cells. *The Journal of Physical Chemistry C, 115*(13), 6162-6166.

Teo, L. P., Buraidah, M. H., Nor, A. F. M., & Majid, S. R. (2012). Conductivity and dielectric studies of Li_2SnO_3. *Ionics, 18*(7), 655-665.

Tiong, T. S., Buraidah, M. H., Teo, L. P., & Arof, A. K. (2016). Conductivity studies of poly(ethylene oxide)(PEO)/poly(vinyl alcohol) (PVA) blend gel polymer electrolytes for dye-sensitized solar cells. *Ionics, 22*(11), 2133-2142.

Tubtimtae, A., & Lee, M.-W. (2012). Effects of passivation treatment on performance of CdS/CdSe quantum-dot co-sensitized solar cells. *Thin Solid Films, 526*(Supplement C), 225-230.

Turnbull, D., & Cohen, M. H. (1961). Free-volume model of the amorphous phase: Glass transition. *The Journal of Chemical Physics, 34*(1), 120-125.

Vijayakumar, E., Kang, S.-H., & Ahn, K.-S. (2018). Facile electrochemical synthesis of manganese cobalt sulfide counter electrode for quantum dot-sensitized solar cells. *Journal of The Electrochemical Society, 165*(5), F375-F380.

Vogel, R., Hoyer, P., & Weller, H. (1994). Quantum-Sized PbS, CdS, Ag_2S, Sb_2S_3, and Bi_2S_3 particles as sensitizers for various nanoporous wide-bandgap semiconductors. *The Journal of Physical Chemistry, 98*(12), 3183-3188.

Vogel, R., Pohl, K., & Weller, H. (1990). Sensitization of highly porous, polycrystalline TiO_2 electrodes by quantum sized CdS. *Chemical Physics Letters, 174*(3), 241-246.

Veerathangam, K., Senthil Pandian, M., & Ramasamy, P. (2018). Influence of SILAR deposition cycles in CdS quantum dot-sensitized solar cells. *Journal of Materials Science: Materials in Electronics, 29*(9), 7318-7324.

Wang, Y., Hou, Y., Tang, A., Feng, B., Li, Y., Liu, J., & Teng, F. (2007). Synthesis and optical properties of composition-tunable and water-soluble $Zn_xCd_{1-x}Te$ alloyed nanocrystals. *Journal of Crystal Growth, 308*(1), 19-25.

Xu, B., & Lin, B. (2016). Reducing carbon dioxide emissions in China's manufacturing industry: a dynamic vector autoregression approach. *Journal of Cleaner Production, 131*, 594-606.

Yang, J., Wang, J., Zhao, K., Izuishi, T., Li, Y., Shen, Q., & Zhong, X. (2015). CdSeTe/CdS Type-I Core/Shell quantum dot sensitized solar cells with efficiency over 9%. *The Journal of Physical Chemistry C, 119*(52), 28800-28808.

Yang, Z., Chen, C.-Y., Roy, P., & Chang, H.-T. (2011). Quantum dot-sensitized solar cells incorporating nanomaterials. *Chemical Communications, 47*(34), 9561-9571.

Yasuo, C., Ashraful, I., Yuki, W., Ryoichi, K., Naoki, K., & Liyuan, H. (2006). Dye-sensitized solar cells with conversion efficiency of 11.1%. *Japanese Journal of Applied Physics, 45*(2), 24-28.

Yeh, M.-H., Lee, C.-P., Chou, C.-Y., Lin, L.-Y., Wei, H.-Y., Chu, C.-W., & Ho, K.-C. (2011). Conducting polymer-based counter electrode for a quantum-dot-sensitized solar cell (QDSSC) with a polysulfide electrolyte. *Electrochimica Acta, 57*, 277-284.

Yu-Jen, S., & Yuh-Lang, L. (2008). Assembly of CdS quantum dots onto mesoscopic TiO_2 films for quantum dot-sensitized solar cell applications. *Nanotechnology, 19*(4), 045602.

Yu, X.-Y., Lei, B.-X., Kuang, D.-B., & Su, C.-Y. (2011). Highly efficient CdTe/CdS quantum dot sensitized solar cells fabricated by a one-step linker assisted chemical bath deposition. *Chemical Science, 2*(7), 1396-1400.

Yu, Z., Zhang, Q., Qin, D., Luo, Y., Li, D., Shen, Q., & Meng, Q. (2010). Highly efficient quasi-solid-state quantum-dot-sensitized solar cell based on hydrogel electrolytes. *Electrochemistry Communications, 12*(12), 1776-1779.

Zhang, Q., Zhang, Y., Huang, S., Huang, X., Luo, Y., Meng, Q., & Li, D. (2010). Application of carbon counterelectrode on CdS quantum dot-sensitized solar cells (QDSSCs). *Electrochemistry Communications, 12*(2), 327-330.

Zhao, K., Pan, Z., Mora-Seró, I., Cánovas, E., Wang, H., Song, Y., Gong, X., Wang, J., Bonn, M., Bisquert, J., & Zhong, X. (2015). Boosting power conversion efficiencies of quantum-dot-sensitized solar cells beyond 8% by recombination control. *Journal of the American Chemical Society, 137*(16), 5602-5609.

LIST OF PUBLICATIONS AND PAPERS PRESENTED

Publications:

Mingsukang, M. A., Buraidah, M. H., & Arof, A. K. (2017). Third-generation-sensitized solar cells. In N. Das (Ed.), *Nanostructured Solar Cells* (pp. Ch. 02). Rijeka: InTech.

Mingsukang, M. A., Buraidah, M. H., Careem, M. A., Albinsson, I., Mellander, B. E., & Arof, A. K. (2017). Investigation of counter electrode materials for gel polymer electrolyte based quantum dot sensitized solar cells. *Electrochimica Acta, 241*, 487-496.

Mingsukang, M. A., Buraidah, M. H., & Careem, M. A. (2017). Development of gel polymer electrolytes for application in quantum dot-sensitized solar cells. *Ionics, 23*, 347-355.

Papers presented:

Mingsukang, M. A., Buraidah, M. H., Careem, M. A., & Arof A. K., Fabrication and characterization of QDSSCs with methylcellulose–polysulphide GPE, International research conference on solar energy materials, solar cells and solar energy applications (SOLAR ASIA 2018), 4–6 January 2018, Kandy, Sri Lanka. (International).

Mingsukang, M. A., Hisamuddin, S. N., Baharun, N. N. S., Lee, Y. C., Abidin, Z. H. Z., Buraidah, M. H., Karakas, A., & Arof, A. K., Study of some sensitizers for gel polymer electrolyte based sensitized solar cells (SSCs), International Conference on Functional Materials & Devices 2017 (ICFMD - 2017), 15 – 18 August 2017, Malacca, Malaysia. (International).

Mingsukang, M. A., Buraidah, M. H., Careem, M. A., & Arof A. K., Cadmium sulphide quantum dots as sensitizer in sensitized solar, National Workshop on Functional Materials 2017 (NWFM 2017), 17-18 January, 2017, University of Malaya, Malaysia. (National).

Mingsukang, M. A., Buraidah, M. H., Careem, M. A., Albinsson, I., Mellander, B. E., & Arof, A. K., Investagation of counter electrode materials for gel polymer electrolyte based QDSSCs, International Symposium on Polymer Electrolytes (ISPE 2016) 15–19 August 2016, Uppsala, Sweden (International).

Mingsukang, M. A., Buraidah, M. H., Careem, M. A., & Arof A. K., Development of methylcellulose–polysulphide gel polymer electrolyte for QDSSCs application, International Symposium on Materials and Asset Integrity (ISMAI 2016), 16–18 May 2016, Putra World Trade Centre, Kuala Lumpur. (International).